SANDIA REPORT
SAND2015-8388
Unlimited Release
Printed Month and Year

Understanding H isotope adsorption and absorption of Al-alloys using modeling and experiments (LDRD: #165724)

Donald K. Ward, Xiaowang Zhou, Richard A. Karnesky, Robert Kolasinski, Michael E. Foster, Ryan B. Sills, Konrad Thürmer, Paul Chao, Ethan N. Epperly, Bryan M. Wong, Jonathan A. Zimmerman

Prepared by
Sandia National Laboratories
Albuquerque, New Mexico 87185 and Livermore, California 94550

Sandia National Laboratories

Issued by Sandia National Laboratories, operated for the United States Department of Energy by Sandia Corporation.

Available to DOE and DOE contractors from
U.S. Department of Energy
Office of Scientific and Technical Information
P.O. Box 62
Oak Ridge, TN 37831

Telephone: (865) 576-8401
Facsimile: (865) 576-5728
E-Mail: reports@osti.gov
Online ordering: http://www.osti.gov/scitech

Available to the public from
U.S. Department of Commerce
National Technical Information Service
5301 Shawnee Rd
Alexandria, VA 22312

Telephone: (800) 553-6847
Facsimile: (703) 605-6900
E-Mail: orders@ntis.gov
Online order: http://www.ntis.gov/search

SAND2015-8388
Unlimited Release
Printed Month 2015

Understanding H isotope adsorption and absorption of Al-alloys using modeling and experiments (LDRD: 165724)

Donald K. Ward
Radiation and Nuclear Detection Materials and Analysis: 8126

Xiaowang Zhou
Mechanics of Materials: 8256

Richard A. Karnesky
Hydrogen and Combustion Technology: 8367

Robert Kolasinski
Energy Innovation: 8366

Michael E. Foster
Materials Chemistry: 8223

Ryan B. Sills
Gas Transfer Systems: 8254

Konrad Thürmer
Materials Physics: 8342

Paul Chao
Hydrogen and Combustion Technology: 8367
Carnegie Mellon University, Pittsburgh, PA

Ethan Epperly
Radiation and Nuclear Detection Materials and Analysis: 8126
Livermore Valley Charter Preparatory High School, Livermore, CA

Bryan M. Wong
Materials Chemistry: 8223
Chemical and Environmental Engineering Materials Science and Engineering
University of California, Riverside
Riverside, California 92521

Jonathan A. Zimmerman
Hydrogen and Combustion Technology: 8367

Sandia National Laboratories
P.O. Box 969
Livermore, California 94551-0969-MS957

Abstract

Current austenitic stainless steel storage reservoirs for hydrogen isotopes (e.g. deuterium and tritium) have performance and operational life-limiting interactions (e.g. embrittlement) with H-isotopes. Aluminum alloys (e.g.AA2219), alternatively, have very low H-isotope solubilities, suggesting high resistance towards aging vulnerabilities. This report summarizes the work performed during the life of the Lab Directed Research and Development in the Nuclear Weapons investment area (165724), and provides invaluable modeling and experimental insights into the interactions of H isotopes with surfaces and bulk AlCu-alloys. The modeling work establishes and builds a multi-scale framework which includes: a density functional theory informed bond-order potential for classical molecular dynamics (MD), and subsequent use of MD simulations to inform defect level dislocation dynamics models. Furthermore, low energy ion scattering and thermal desorption spectroscopy experiments are performed to validate these models and add greater physical understanding to them.

ACKNOWLEDGMENTS

Sandia National Laboratories is a multiprogram laboratory managed and operated by Sandia Corporation, a wholly owned subsidiary of Lockheed Martin Corporation, for the US Department of Energy's National Nuclear Security Administration under contract DE-AC04-94AL85000 (SAND2014-3909 J). This work was performed under a Laboratory Directed Research and Development (LDRD) project. The authors appreciate the valuable discussions with the reviewers.

We thank Professor Wei Cai of Stanford University for his contributions to the dislocation dynamics algorithm development.

We thank Tom Arsenlis and Sylvie Aubry (Lawrence Livermore National Laboratory) for assistance and access to ParaDiS.

We thank Jake Ostien, Tim Shepodd, Alf Morales, Adam Rowen, and Marie Kane for their support during this project.

Additionally, we would like to thank Dorian Balch (8254), Chris San Marchi (8367), Brian Somerday (8367), and James Foulk (8256) for thoughtful conversation in framing the outline for this project.

Contents

FIGURES

TABLES

NOMENCLATURE

MD	molecular dynamics
MS	molecular statics
BOP	bond-order potential (Pettifor style)
DD	dislocation dynamics
DFT	density functional theory
LEIS	low energy ion scattering
TDS	thermal desorption spectroscopy
Al	Aluminum
Cu	Copper
di	dimer
tri	trimer
ch	chain
tetra	tetragon
rhom	rhombus
rec	rectangle
dc	diamond-cubic
sc	simple-cubic
bcc	body-centered-cubic
fcc	face-centered-cubic
hcp	hexagonal-closely-packed
gra	graphite
grap	graphene
fcs	face-centered-square
zb	zinc-blende
wz	wurtzite
PAW	projector-augmented-wave
VASP	Vienna Ab initio Simulation Package
vdW	van der Waals
GGA	generalized-gradient approximation
PBE	Perdew, Burke and Ernzerhof density functional
LAMMPS	Large-scale Atomic/Molecular Massively Parallel Simulator.
CCSD(T)	coupled cluster theory with singles, doubles and perturbative triple excitations
TZVP	triple-zeta basis set with polarization
DOE	Department of Energy
SNL	Sandia National Laboratories

1. INTRODUCTION

Stainless steel is ubiquitous as a structural material for a large number of applications including transportation, aviation, energy, and hydrogen isotope (H=protium (P), deuterium (D), or tritium (T)) containment. Many of the environments for these applications include exposure to hydrogen, either in the form of gas or water. Ultimately, the operational effectiveness of austenitic stainless steel components will degrade due to life-limiting interactions (e.g. embrittlement) with H isotopes [1]. This is particularly of concern for storage reservoirs of rarer or more hazardous hydrogen isotopes. Hydrogen containment materials are critical for many applications in Sandia's portfolio. Decades of engineering experience with austenitic stainless steel have defined a safe operating envelope for managing hydrogen embrittlement in this material class. Aluminum alloys have shown potential for improved compatibility for containment of H isotopes. Aluminum alloys (e.g. AA2219), alternatively, have very low H-isotope solubilities, suggesting high resistance towards aging vulnerabilities. Yet, in certain environments, even Al-Alloys show the effects of exposure to H [2,3]. Accurate component lifetime predictions require a fundamental understanding of H-isotope interactions with Al-metal/oxide surfaces and crystalline defects (dislocations, precipitates). Unfortunately, the long-time scales associated with H-isotopes transport and engineering design lifetimes make sole experimental investigations impractical. The ideal tool for analyzing reservoirs would be a continuum level constitutive model for use in a finite element framework. However, such a model capable of capturing the correct aging of the material does not and cannot exist without a fundamental understanding of the crystalline defects and their interaction mechanisms. A truly predictive defect model requires information from the atomic-level, which in-turn requires a high-fidelity interatomic potential.

This work focuses on the interactions of H isotopes with binary Al-Cu alloys. Copper is a common alloying element in Al-alloys and is the primary source of precipitation strengthening in candidate alloys such as AA2219. Age hardening forms Al-Cu intermetallic precipitates that strengthen the material. Al-Cu precipitates evolve through a series phases during aging: α → GP-I → GP-II/θ'' → θ' → θ, where α is supersaturated solid solution, GP-I zones are coherent (100) Cu monolayer disks, GP-II zones are larger coherent Cu discs separated by three Al planes, θ' is a semicoherent Al_2Cu phase (tetragonal distortion of the CaF_2 structure), and θ is an incoherent c16 structure. This work explores the fundamental H isotope interactions with a multiscale modeling framework in conjunction with a rigorous experimental program. The multiscale modeling framework incorporates models at three different length and time scales, high quality density functional theory (DFT), classical molecular dynamics (MD) employing a high fidelity interatomic bond-order-potential (BOP), and defect level dislocation dynamics (DD). Using a bottom up approach, DFT→ DD, as data and information are gathered at lower length scales it is passed to the higher length and time scales resulting in high fidelity models which represent the appropriate physics from the lower length scales. First, we have developed the first-ever chemical-reaction-simulation-enabling high fidelity ternary bond-order-potential (BOP). Transferability to a variety of configurations is the key to accurate simulations of material interaction with H. Many potentials exist to model materials (e.g. embedded atom method [4], modified embedded atom method [5], angular-dependent [6]), but, none of them effectively capture complicated systems with the fidelity of the bond-order potential (BOP) [7–11]. The fidelity of the BOP is achieved by extensively benchmarking with high quality density function theory (DFT) calculations, and validating with experiments. The BOP is then used in molecular dynamics (MD) and Monte Carlo (MC) simulations to study adatom trapping energies and absorption mechanisms. Second, we developed a defect dynamics (DD) model, informed from atomistics and experiments, to study effects of precipitates on the motion of dislocations within the binary system. This model is a critical tool for understanding the mechanisms responsible for continuum level material response to applied stress. We started with Lawrence Livermore National Lab and Stanford University's open source DD software (ParaDiS) [12], which has been developed strictly for dislocation/dislocation interactions. Dislocation dynamics simulations describe the material as an elastic body containing line defects that interact with each other through superimposed elastic fields. The motion of the dislocations is governed by the forces imposed by the elastic field and a dislocation mobility law. We advanced this software with the inclusion of elastic defects (inclusions, precipitates). Using input from MD simulations utilizing BOP was critical in the development of this model. As an example, misfit strains for the Cu precipitates were calculated using MD. DD then takes the misfit strains and incorporates that into the strain field of the defect level simulation. The software developed is not fully mature, but establishes a framework for adding complicated interactions to create a more sophisticated model in the future.

Novel experiments using low energy ion scattering (LEIS) were performed to explore H on surfaces and trapping in Al-Cu in order to refine underlying assumptions of the models and to validate model predictions. LEIS provides information on the structure and composition of surfaces by analyzing the energies and intensities of low energy ions scattered from surfaces. In contrast to other surface techniques, it is directly sensitive to adsorbed H. From the perspective of addressing the problem of H embrittlement, it is one of only a few methods capable of elucidating the atomic-scale processes by which hydrogen adsorbs on the surface and then migrates into the bulk material. Our angle-resolved ion energy spectrometer (ARIES) at Sandia is a unique LEIS instrument that has been specifically optimized for studies of light adsorbates on surfaces. The instrument is equipped with a high-sensitivity ion time of flight spectroscopy system capable of detecting small concentrations of hydrogen on surfaces. ARIES also includes an Auger electron spectrometer for detailed compositional analysis. Our recent work has included several enhancements to LEIS specifically suited for observing adsorbed hydrogen. Recently, we developed an approach for rigorously comparing LEIS measurements with binary collision models to obtain surface structure information [13]. We have demonstrated the capabilities of determining the H-binding site as well as its height above the first layer of W surfaces [14]. We are able to dose materials with calibrated amounts of atomic H. Detecting the configuration of these adsorbates on single crystal aluminum provided insight into binding energies and bond lengths to complement the aforementioned models.

In conjunction with the surface adsorption experiments, trapping energies were measured using thermal desorption spectroscopy (TDS). While this technique has been used for pure Al [15,16], and some alloys [17,18], it had not been previously applied in a binary alloy where the alloying content or aging condition has been varied systematically to study trapping at solute atoms and precipitates in Al.

The overarching technical goal of this project was to forward the understanding of H-materials interactions in the Al-Cu system. Ultimately, we would like to have continuum level models for simulating the long-term exposure of Al-alloys to H-isotope environments. This project establishes the foundation for understanding the fundamental mechanisms responsible for the H effects on the alloys of interest. This work provides an invaluable, density functional theory (DFT) informed, Al-Cu-H interatomic potential. This potential now gives us the ability to do ground breaking studies using Molecular Dynamics (MD) and Monte Carlo (MC) simulations to further study adatoms, trapping energies and additional absorption mechanisms, validated with experiments. Additionally, we now have a capable three-dimensional material defects (dislocations, precipitates) model, so termed defect dynamics (DD). This DD capability allows us to begin forming more accurate crystal plasticity and continuum models to represent real materials with complicated microstructures. We plan to continue building on this multiscale modeling framework and answer many of the fundamental questions regarding the interaction of H-isotopes with AlCu-alloys.

2. AN ANALYTICAL BOND-ORDER POTENTIAL FOR THE ALUMINUM, COPPER, AND HYDROGEN TERNARY SYSTEM

The majority of the work that follows is included or will be included in three separate publications [19–21], the published work will be summarized here with further details in the references.

2.1. Introduction

The parameterization of a ternary BOP requires the development of seven total potentials, Al-Al, Cu-Cu, H-H, Al-Cu, Al-H, Cu-H, and Al-Cu-H. Each of these potentials must be parameterized and validated before a high fidelity ternary potential is completed. Six specific measures can be used to determine if an Al-Cu-H interatomic potential achieves the required fidelity: (1) the potential gives a high stacking fault energy of Al observed in experiments [22], as this property critically impacts mechanical behavior; (2) the potential captures Al-rich side of the Al-Cu phase diagram [23], meaning that any $Al_{1-x}Cu_x$ system with an overall composition $0 < x < 0.333$ needs to separate to Al + Al_2Cu two phases [24]; (3) the potential prescribes a reasonable positive heat of solution of Cu in Al; (4) the potential can simulate the $H_2 \leftrightarrow 2H$ chemical reaction in order to study how hydrogen is incorporated into the material when the surface interacts with H_2 gas; (5) the potential predicts the $Al_{1-x}H_x \rightarrow Al + H_2$ and $Cu_{1-x}H_x \rightarrow Cu + H_2$ phase separations as shown by the experimental Al-H [25] and Cu-H [26] phase diagrams; and (6) the potential is well fitted to properties of a variety of structures including stable ones observed in experiments and metastable ones calculated from quantum mechanical methods, so that any non-equilibrium local environments encountered during deformation and fracture can be accurately accounted for. If all of these criteria are met, then the potential should enable fundamental studies of Al-Cu alloys to reach such a point that they can replicate the relevant experimental observations, promote understanding of mechanisms, and guide material improvement. We are not aware of any Al-Cu-H ternary potentials in literature (check). However, tremendous efforts have been made to develop interatomic potentials for Al-Cu [4,27–44], Al-H [5,6], and Cu-H [45–48] systems. These efforts indicate that meeting the six criteria for the Al-Cu-H potential is extremely challenging.

First, the abnormally high stacking fault energy of Al is difficult to capture [20] and as a result, of all the potentials cited above, only those developed by Mendelev *et al*. [32,37], Mishin *et al*. [39,40], and Jelinek *et al*. [42] achieves this. Furthermore, some of these potentials [39,40] achieve high stacking fault energies by allowing the potential functions to have multiple energy minimums, which is an undesirable feature.

The $Al_{1-x}Cu_x \rightarrow Al + Al_2Cu$ phase separation has also not been well addressed by literature potentials [20]. The potential published by Mishin *et al*. [39–41] is perhaps the most carefully parameterized because the authors did demonstrate lower energies for the two commonly observed Al_2Cu phases, θ and θ’, when compared to a large number of other crystalline phases at the same composition. The problem is that such a comparison does not ensure the lowest energies for the θ and θ’ phases when compared to all other competing configurations because regardless of how many phases are included in the study, they do not cover an infinite number of amorphous structures, nor mixtures of multiple phases. In fact, we [20] discovered that Mishin *et* *al.*'s potential [40] predicts a much lower energy for a mixture of Al and AlCu (B2 crystal) than for a mixture of Al and Al_2Cu (θ or θ'). Hence, even the most successfully parameterized (and most widely applied) Al-Cu potential [20] available today does not capture the Al-rich side of the Al-Cu phase diagram.

In past potential development, the dilute heat of solution of Cu in Al is usually assumed to be the energy change by taking a Cu atom from a large Cu crystal and putting it back into a large Al crystal, which gives a negative value. According to the phase diagram, the experimental dilute heat of solution of Cu in Al should be the energy change by taking an Al_2Cu molecule from a large Al_2Cu crystal and putting it back into a large Al crystal [20], which gives a positive value. It is desired for the potential to best capture the experimental $Al_2Cu \rightarrow Al$ heat of solution over the quantum mechanical $Cu \rightarrow Al$ one.

Simulating chemical reactions (e.g., $H_2 \leftrightarrow 2H$) is always a challenge in conventional MD simulations, although direct MD simulations of the $O_2 + 2H_2 \leftrightarrow 2H_2O$ combustion processes have been recently demonstrated using reactive force field (ReaxFF) [49]. Unfortunately, none of the Al-H [5,6] and Cu-H [45–48] potentials cited above allows chemical reactions. Consequently, these potentials also do not capture the $Al_{1-x}H_x \rightarrow Al + H_2$ and $Cu_{1-x}H_x \rightarrow Cu + H_2$ phase separations that involve H_2 molecules.

In recent years, the present authors have developed bond order potentials (BOPs) for both Al-Cu [20] and Cu-H [19] binary systems. Our BOPs capture property trends of a variety of structures as obtained from experiments and quantum mechanical calculations. In addition, our potentials have unique advantages as they predict a high stacking fault energy of Al without multiple energy minimums, replicate the Al-rich side of the experimental Al-Cu phase diagram, give a positive $Al_2Cu \rightarrow Al$ heat of solution, allow direction MD simulations of $H_2 \leftrightarrow 2H$ chemical reaction, and capture the $Cu + H_2$ equilibrium over the entire composition range as seen in the experimental Cu-H phase diagram. We found that the key to achieve these is to not only fit properties of many structures as is usually done, but also to use high temperature MD simulations to validate the correct structural evolution from initial chaotic configurations to final equilibrium phases. Such MD simulations are sufficiently stringent that they can usually ensure the lowest free energy for the equilibrium phase as compared to any other configurations. This is because the configurations sampled during the chaotic to crystalline transformation can in fact cover an infinite number of amorphous phases, and the ones that do not get sampled are because they have higher energies. To reflect this, Mishin *et al.*'s Al-Cu potential [40] does not pass the MD vapor deposition simulation tests as it would predict amorphous growth when Al and Cu atoms are injected to θ or θ' substrate at the stoichiometric ratio Al:Cu = 2:1. Our BOP [20], on the other hand, predicts crystalline growth of both θ and θ'.

The present work looks to construct an Al-Cu-H ternary BOP based on previously developed Al-Cu and Cu-H BOPs. In addition to fitting property trends of a variety of elemental and compound configurations (with coordination varying from 1 to 12 including small clusters, bulk lattices, defects, and surfaces), we focus to iteratively improve the potential using stringent molecular dynamics simulation tests so that the six criteria described above are all met by the Al-Cu-H potential.

2.2. General Expression of Bond-Order Potential

Based on the approach developed by Pettifor *et al*. [7–9,50,51], the total energy of our BOP for a system containing N atoms (i=1,2,…N) is expressed as

$$E = \frac{1}{2}\sum_{i=1}^{N}\sum_{j=i_1}^{i_N} U_{ij}(r_{ij}) - \sum_{i=1}^{N}\sum_{j=i_1}^{i_N} V_{ij}(r_{ij})\cdot\Theta_{ij} - \sum_{i=1}^{N}\sum_{j=i_1}^{i_N} V_{2,ij}(r_{ij})\cdot\Theta_{2,ij} \qquad (1)$$

where $U_{ij}(r_{ij})$, $V_{ij}(r_{ij})$, and $V_{2,ij}(r_{ij})$ are pairwise functions, Θ_{ij} and $\Theta_{2,ij}$ are many-body variables that can be calculated from atom positions, and the list $j = i_1, i_2, \ldots, i_N$ represents neighbors of atom i. The mathematics of the BOP is fairly complex, and may not be of interest to majority of readers. Hence, detailed expressions for $U_{ij}(r_{ij})$, $V_{ij}(r_{ij})$, $V_{2,ij}(r_{ij})$, Θ_{ij} and $\Theta_{2,ij}$ are given in Ref. [19], as well as all fitting procedures.

2.3. Evaluation of the potential

Using parallel MD code LAMMPS [52,53] , extensive simulations are performed to characterize our Al-Cu-H BOP. In addition to providing static properties obtained from energy minimization simulations, we also validate the potential using stringent MD simulations. Static properties include cohesive energies and crystal dimension (atomic volumes or lattice constants) of various lattice structures; and elastic constants, melting temperatures, stacking fault and surface energies, properties of common point defects (vacancies, interstitials), and heats of formation of the lowest energy phases. MD simulations will involve chaotic configurations so that structures that are not included in energy minimization calculations are all tested.

To illustrate the ability of our BOP for simulating non-equilibrium configurations, cohesive energies and atomic volumes of various structures and element combinations, characteristic of different local environments, are in Figure 1-Figure 5. For each of the figures, open circles represent the results from BOP, stars are from experiments, and the orange lines connect the scaled DFT data. Here the scaled DFT data are obtained by multiplying the original DFT data with a constant so that the DFT and the experimental properties exactly match for the equilibrium phases.

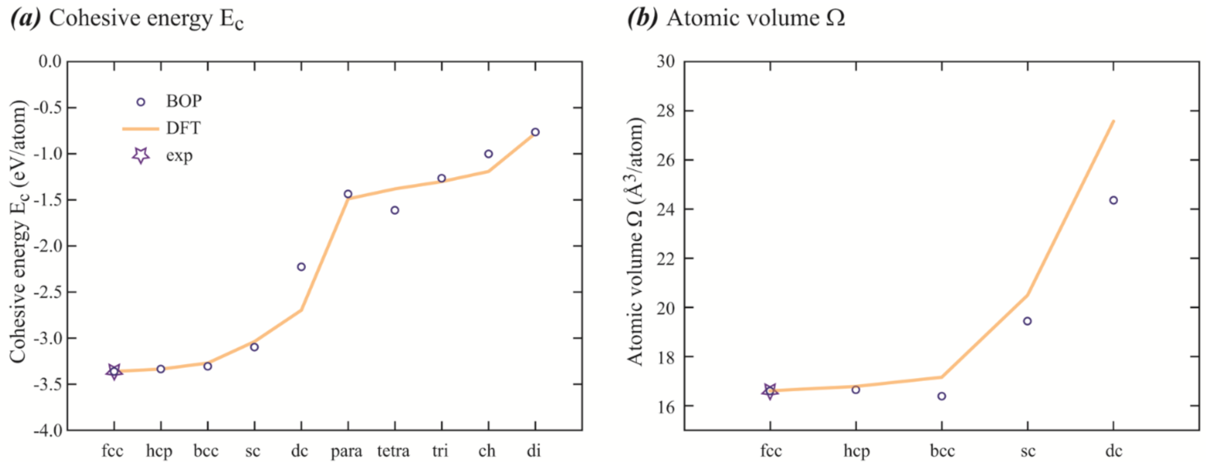
(a) Cohesive energy E_c ***(b)*** Atomic volume Ω

Figure 1. (a) Cohesive energies and (b) atomic volumes of various Al structures as obtained from BOP, DFT, and experiment [54,55]. Note: the orange lines are composed of straight-line segments connecting the neighboring data points (for clarity, the data points at the junctions of the segments are not shown). These segments do not imply continuity of data, but are used to guide the eye.

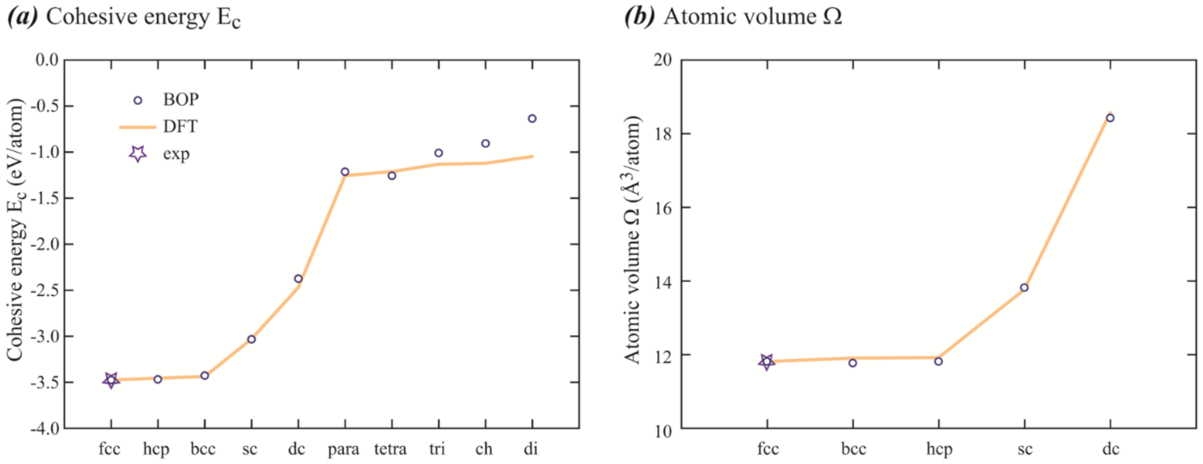

Figure 2. (a) Cohesive energies and (b) atomic volumes of various Cu structures as obtained from BOP, DFT, and experiment [54,55]. See Figure 1 for explanation of the lines.

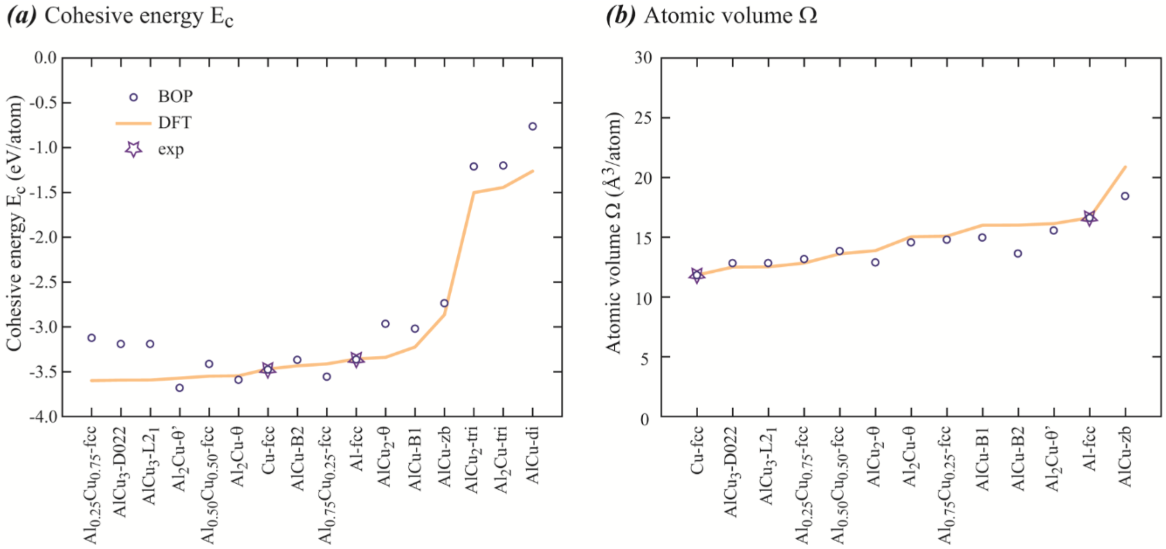

Figure 3. (a) Cohesive energies and (b) atomic volumes of various Al_nCu_m compound lattices as obtained from BOP, DFT, and experiment [54,55]. See Figure 1 for explanation of the lines.

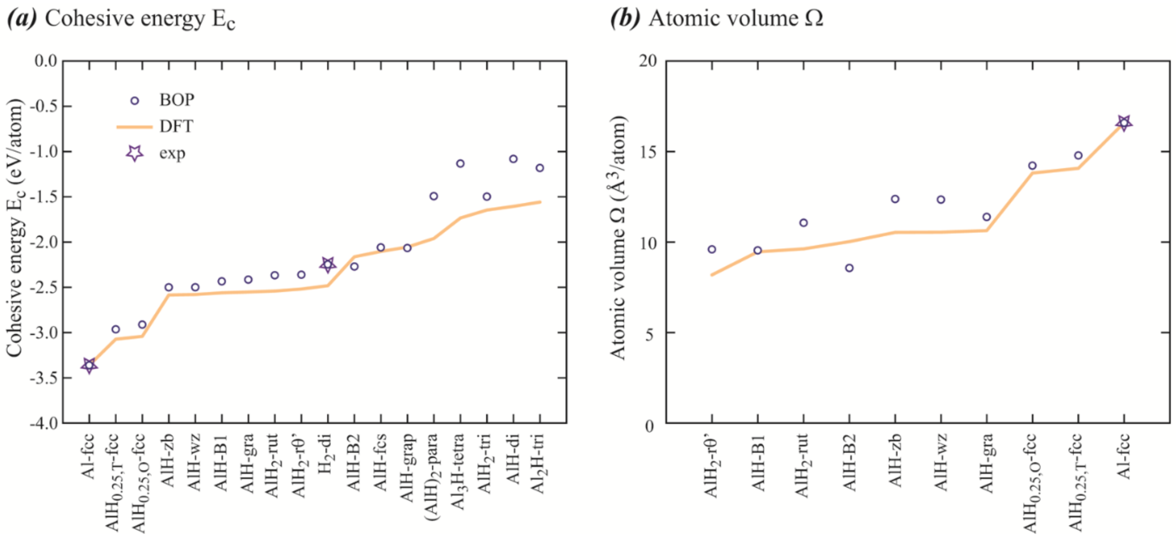

Figure 4. (a) Cohesive energies and (b) atomic volumes of various Al-H structures as obtained from BOP, DFT, and experiment [54,55].

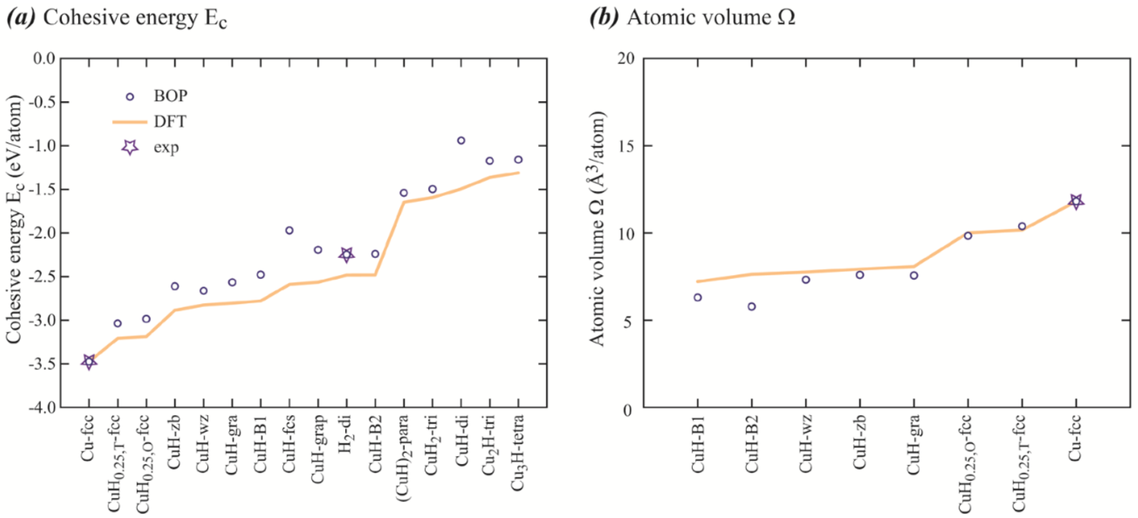

Figure 5. (a) Cohesive energies and (b) atomic volumes of various Cu-H structures as obtained from BOP, and DFT (experimental data [54,55] elemental phases are included for reference).

It is clear from these Figures that BOP does a tremendous job of capturing the property trends for these elemental combinations.

Beyond the just the energy and structural trends of materials it is also important to capture the correct heat of solution, particular for alloys with propensity to have concentrations of solutes. For Al-Cu solid solutions, our BOP gives a dilute heat of solution for Al_2Cu in Al as $\Delta E_s = 0.14$ eV. Historically, interatomic potentials are fitted to heat of solution of Cu in Al. As a result, the (Al_2Cu in Al) heat of solution predicted by the BOP is significantly closer to the experimental value of 0.45 eV [20] than those predicted by other potentials. For instance, the angular dependent potential developed by Apostol and Mishin [6] gives a value of 1.09 eV, whereas the EAM potential developed by Cai and Ye gives a negative value of -0.06 eV [31] .

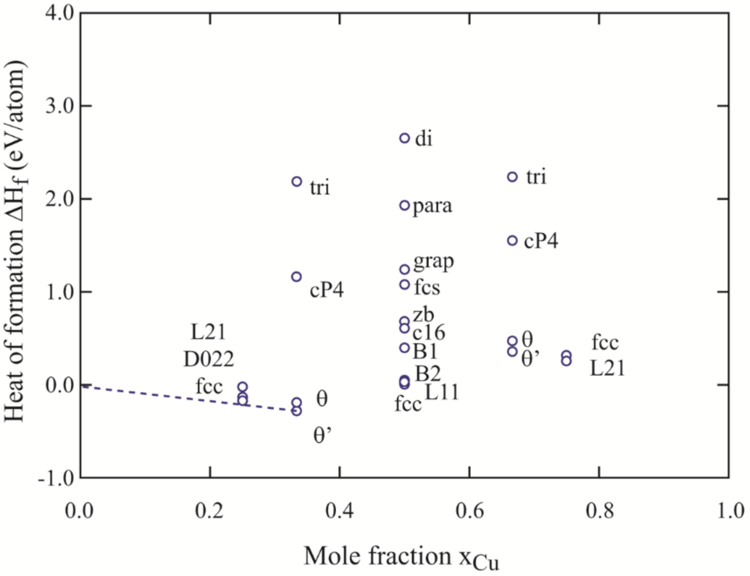

Figure 6. Heats of formation of ΔH$_f$ as a function of mole fraction x$_{cu}$ for various Al$_n$Cu$_m$ compounds.

While the metal-H interactions have already been presented above, it is still important to discuss the H-H interactions. The chemistry involved with H interactions is typically difficult for classical empirical interatomic potentials. However, BOP is capable of capturing the chemistry involved in H bonding. For the equilibrium H_2 gas phase, our BOP gives an equilibrium diatomic bond length d = 0.752 Å, and a cohesive energy E_c = -2.247 eV/atom. These are exactly the same as our CCSD(T) (coupled-cluster theory with single, double and perturbative triple excitations) quantum mechanical value d = 0.752 Å [19] and experimental value E_c = 2.247 eV/atom [54]. Other than the H_2 gas phase, the most important property of hydrogen is the reactivity during $H_2 \rightarrow 2H$ dissociation. A more stringent test is to examine the $H + H_2 \rightarrow H_2 + H$ chemical reaction because this reaction is associated with an energy barrier. Physically, when an H_2 molecule is approached by a third H atom, the incoming H may react with one H atom in the molecule to form a new H_2 molecule while ejecting the other H atom to vapor. A full geometry of this process is shown in the inlet of Figure 7, where an H atom approaches the H_2 molecule at a constant incident angle θ and the distance between the H atom and the H_2 molecule is represented by d. Energy minimization simulations are used to calculate the total energy of the $H + H_2$ system as a function of d at three different incident angles $\theta = 60^o$, 120^o, and 180^o, assuming that the bond length of the H_2 molecule is always relaxed in response to the incoming atom. The results obtained from BOP and scaled CCSD(T) [19] are shown in Figure 7using data points and solid lines respectively, with the experimental H_2 energy [54] represented by the horizontal dashed line

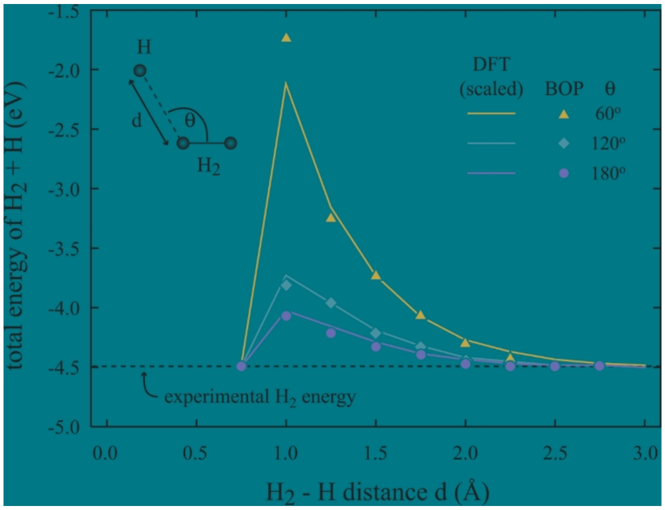

Figure 7. Energy profiles of H + $H_2 \rightarrow H_2$ + H reaction at different incoming atom incident angle θ. Data points and solid lines are obtained from BOP and scaled CCSD(T) respectively, and the horizontal dash line shows the experimental total cohesive energy of an H_2 molecule

The static calculations presented above are not sufficient to prove that any of the predicted low energy phases are indeed stable relative to any other configuration. Stringent MD vapor deposition simulations of each of the potentials are required to confirm the low energy configurations. During an MD simulation of growth, adatoms randomly injected towards a surface of an equilibrium substrate are allowed to form any unconstrained configurations. If the underlying phase is indeed stable, crystalline growth is expected. Otherwise the simulation will likely result in an amorphous growth due to transition towards a lower energy alternative structure. One typical result of our MD simulations of growth on Al (111) is shown in Figure 8, where the original substrate is shaded in pink. Clearly, crystalline growth is obtained, strongly validating that our BOP correctly captures the Al-fcc as the lowest energy equilibrium phase. These simulations are performed for the Al-Al, Cu-Cu, and Al-Cu potentials and the results are given in Figure 8-Figure 10.

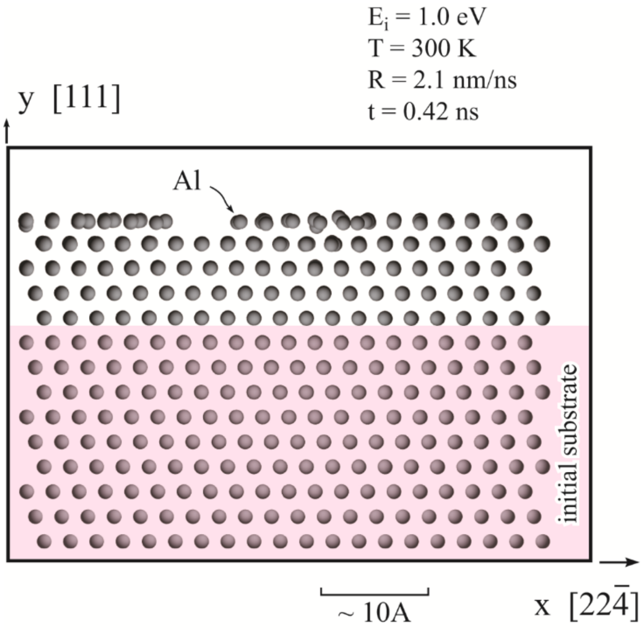

Figure 8. MD simulations of Al (111) growth

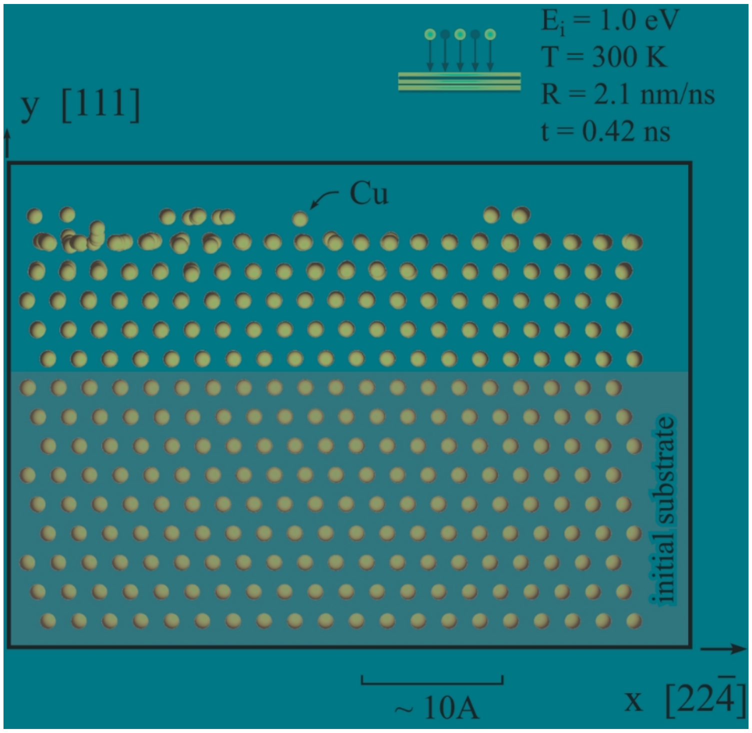

Figure 9. MD simulations of Cu growth.

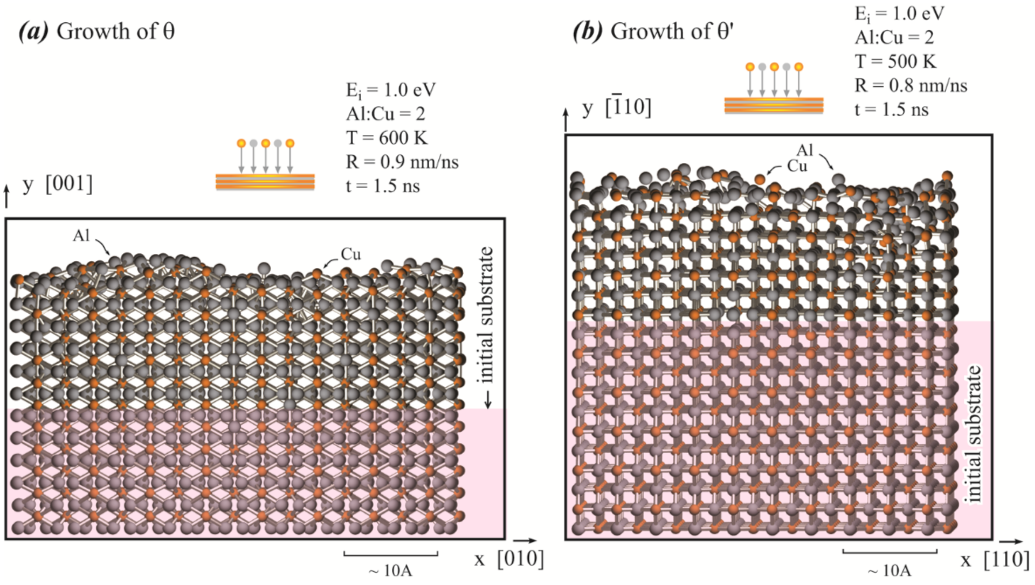

Figure 10. MD simulations of vapor deposition growth of (a) Al_2Cu-Θ and (b) Al_2Cu-Θ'.

Each of the growth simulations confirms that the BOP correctly predicts the low energy structures.

Additionally, it is important to look at the result when H is introduced into the deposition simulations. The resulting configuration obtained after 1.0 ns deposition is shown in Figure 11. It can be seen that although about the same number of Al and H atoms are injected to the surface, the deposited film is mainly composed of Al. This means that a majority of H2 molecules re-evaporate back to the vapor. Such a result again strongly validates that the BOP captures the phase separation. Interestingly, a small amount of H2 molecules dissociate into H atoms. Some H atoms are incorporated in the film, but most of the dissociated H atoms segregate on the surface. All of these observations are consistent with experimental results

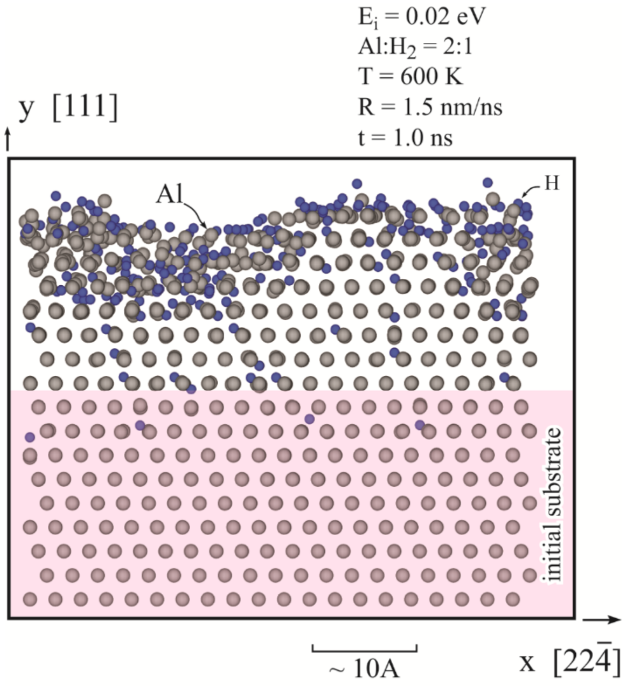

Figure 11. MD simulations of Al growth under H_2 irradiation.

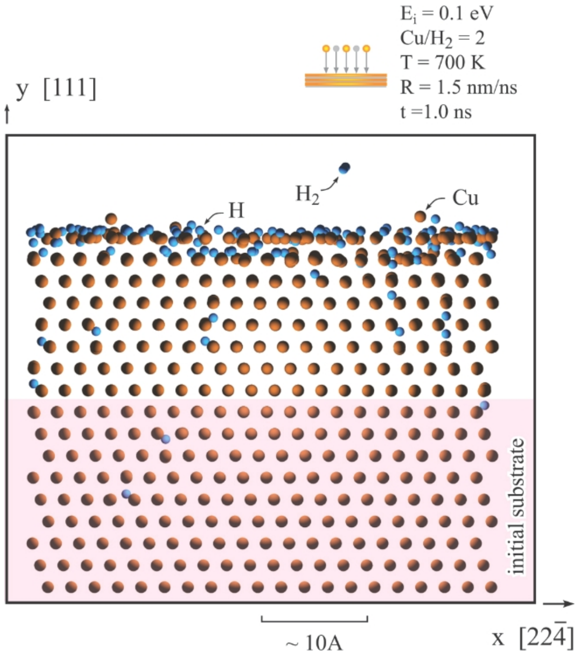

Figure 12. MD simulations of Cu growth under H_2 irradiation.

The results for the Cu-H system are essentially the same. While in our simulation about the same number of Cu and H atoms are injected to the surface, Figure 12 indicates that the deposited film is mainly composed of Cu. This means that a majority of H_2 molecules re-evaporate back to the vapor. Such a result again validates that the BOP captures the phase separation.

Finally, for the Al-Cu-H component of the potential, because no equilibrium phase exists for the system a few metastable configurations are chosen. The metastable structures chosen are the tetrahedral interstitials in a Al_xCu_{1-x}–fcc ordered crystal. Those results are given in Table 1. In particular, it is important recognize that the BOP prediction is closer to DFT values at small x_{Cu}, which is more relevant to the Al-rich Al-Cu alloys, and H occupying tetrahedral interstitial sides gives lower ΔH than occupying octahedral interstitial sites, which is in good agreement with experimental observation that H atoms occupy tetrahedral interstitial sites [56].

Table 1. Partial enthalpy change ΔH (eV/atom) for an H interstitial atom to occupy a tetrahedral site T, an octahedral site O_1 surrounded by Al and Cu atoms, and an octahedral site O_2 surrounded by all Al or All Cu atoms, in Al_xCu_{1-x} alloys.

	$Al_{0.75}Cu_{0.25}$-fcc			$Al_{0.25}Cu_{0.75}$-fcc		
	H in T	H in O_1	H in O_2	H in T	H in O_1	H in O_2
BOP	-2.2094	-1.5132	-1.4331	-1.4166	-1.2789	-1.6326
DFT	-2.0803	-1.3501	-1.4350	-1.5161	-1.5001	-1.6362

To further test the robustness of the potential, we perform an MD vapor deposition simulation to grow Al2Cu-θ and Al2Cu- θ’ with a high flux of H2 simultaneously impacting the growth surface. Figure 13 confirms crystalline growth for both θ and θ’ phases, and majority of H2 molecules are re-evaporated. This strongly validates that our BOP captures the H2 phase separation in ternary compositions.

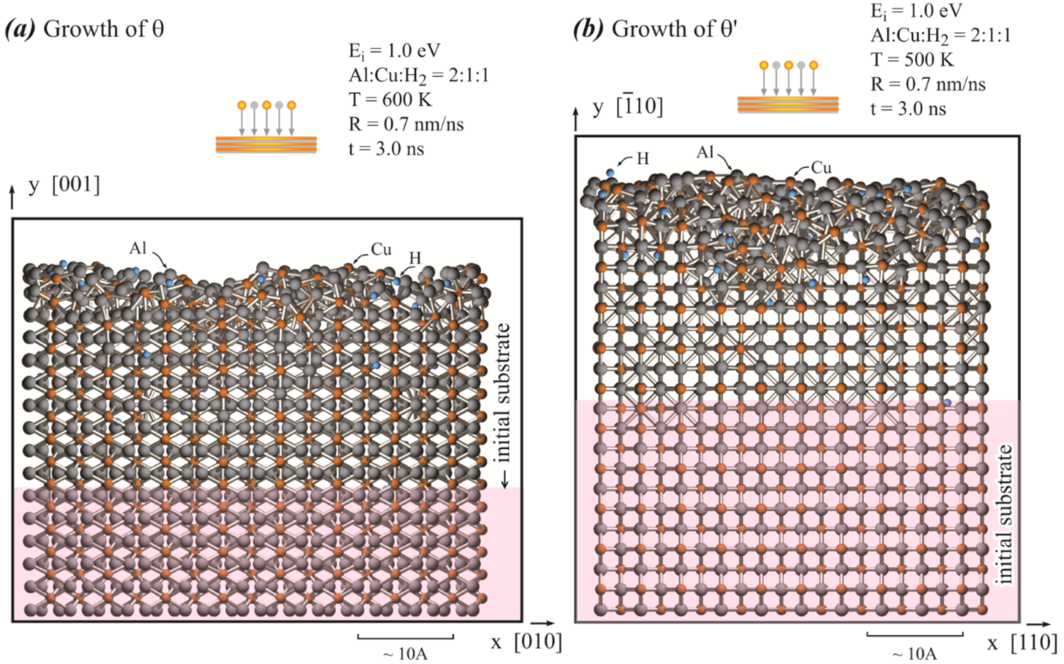

Figure 13. MD simulations of (a) Al_2Cu-Θ and (b) Al_2Cu-Θ’ growth under H_2 irradiation.

2.4. Conclusions

We have developed an Al-Cu-H ternary interatomic potential using the analytical bond-order potential format. In addition to being an Al-Cu-H ternary potential, our BOP has unique advantages over literature binary potentials as it simultaneously meets six criteria: (1) gives a high stacking fault energy of Al seen in experiments; (2) replicates the Al-rich side of the experimental Al-Cu phase diagram; (3) yields a positive heat of solution for Al2Cu in Al; (4) allows simulations of H2 → 2H chemical reactions; (5) predicts correctly Al + H2 and Cu + H2 phase separations; and (6) captures property trends of a variety of Al, Cu, H, Al-Cu, Al-H, Cu-H, and Al-Cu-H structures. We demonstrate the fidelity of our potential not only through energy minimization simulations, but more convincingly through stringent MD simulations that involve chaotic initial configurations. High quality parameterization is achieved by considering a large number of target structures with coordination ranging from 2 to 12; imposing correct parameter bounds; using different minimization schemes; and iterating the parameterization with stringent MD simulation tests. Finally, we will publish our Al-Cu BOP through LAMMPS [52] package, and provide a temporary service prior to the LAMMPS publication where readers can acquire the Al-Cu-H BOP and the related LAMMPS codes by contacting us.

3. ATOMISTIC CALCULATIONS OF DISLOCATION CORE ENERGY IN ALUMINUM

3.1. Introduction

High-fidelity dislocation dynamics (DD) [57] simulations provide fundamental understanding of mechanical properties needed to develop new aluminum alloys. One key input for DD simulations is dislocation core energies.

Dislocation core energies can be calculated using quantum mechanical or empirical atomistic simulations under either continuum boundary [58–62] or periodic boundary [63–71] conditions. A problem with using continuum boundary conditions is that they are only specific to a single dislocation type, and it is extremely challenging to enable the boundary conditions to self-consistently evolve when the dislocation type changes (e.g., a perfect dislocation becomes two partials) during the simulations. Periodic boundary conditions are usually implemented using a so-called quadruple dislocation configuration [63], where positive and negative dislocations (lying in z) alternate the sign in both x and y directions so that a negative dislocation can recover the crystal periodicity destroyed by the preceding positive dislocation in both x and z directions. While the quadruple configuration requires an orthogonal computational cell to include four dislocations, it can be replicated by a non-orthogonal cell containing only two dislocations [63]. A potential difficulty with this method is that because positive and negative dislocations are on the same slip plane (x direction), they may annihilate so that systems can only be relaxed with molecular statics (MS) at 0 K rather than MD at finite temperatures. A more general dislocation configuration that enables an offset of dislocations on different slip planes may solve this problem [69–71]. Finally, we would like to point out that dislocation core energies of aluminum have been calculated using the generalized stacking fault energy obtained from density functional theory [72]. Because core relaxation and dislocation line information are not treated directly, it will be interesting to compare this method with the conventional atomistic simulation approach.

Recently, we have developed a new MD method for calculating core energies of edge dislocations under the periodic boundary condition [73]. This approach eliminates the alternation of dislocations in x, which greatly stabilizes the systems and enables MD simulations to relax dislocation cores. As will be shown below, the use of MD is critical to produce precise results with virtually zero numerical errors. The purpose of the present chapter is threefold: (a) further extend this method to mixed dislocations; (b) generate a complete set of aluminum dislocation core energy data including the functional dependence on the angle β between dislocation line and Burgers vector, and (c) discuss physical insights of the results. We will ensure the quality of our results by utilizing a high-fidelity Al-Cu-H bond order potential (BOP) [21].

3.2. Methods

3.2.1. Edge Dislocation

The geometry of the method for edge dislocations is shown in Figure 14. The system has a dimension of L_x, L_y, and L_z in the x, y, and z direction, respectively, and contains an edge dislocation dipole in y. When the system has $[1\bar{1}0]$ direction in x and $[111]$ direction in y, an edge dislocation dipole with a Burgers vector $[1\bar{1}0]a/2$ and a dislocation line direction parallel to $[\bar{1}\bar{1}2]$ in z can be created by removing a $(1\bar{1}0)$ plane or equivalently two $(2\bar{2}0)$ planes as indicated by the white line in Figure 14. The distance between the dislocation dipoles, d, equals the height of the missing planes. Under the periodic boundary conditions, the dislocations are infinite in the z direction, and the dislocation spacing in the x direction, Sx, equals the system dimension, L_x.

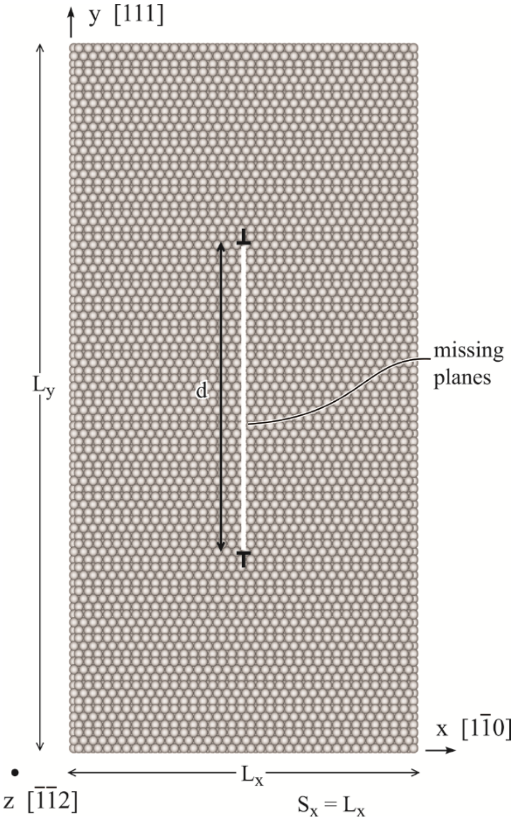

Figure 14. Geometry for edge dislocation dipoles (dislocation spacing S_x equals system dimension L_x).

The study of dislocation dipoles under periodic boundary conditions does not impact the calculations of core energies of isolated dislocations. In fact, a continuum expression of energy of a periodic dislocation array is given by Eq. (C1) in the appendix. The unknown parameters in this expression include core energy E_c and core radius r_0 of isolated dislocations, in addition to shear modulus G, and Poisson's ratio v. Hence, fitting Eq. (C1) to atomistic energy of a periodic dislocation array allows us to determine core energy and core radius of isolated dislocations.

3.2.2. Mixed Dislocation

The method described above cannot be applied to mixed dislocations because the shear deformation of the screw component will destroy the periodic boundary conditions. We note that if the dipole distance is exactly half of the system dimension as shown in Figure 15(a), i.e., $d = L_y/2$, then each dislocation causes the dark and light regions to be displaced exactly by $\pm\frac{1}{2}\vec{b}$. Figure 15(b) shows a 60º dislocation where the dislocation line z $[\bar{1}10]$ and Burgers vector $\vec{b} = [0\bar{1}1]a/2$ forms a 120º (or equivalently, 60º) angle. The plane stacking in the x $[11\bar{2}]$ direction is ABCDEFABCDEF… It can be seen that a C plane can recover to another C plane if it is shifted by 2. Hence, periodic boundary conditions can be maintained for the 60º dislocation if we create four dislocation diploes in the computational cell as shown in Figure 15(a). Similarly, 30º dislocations shown in Figure 15(c) can also be simulated under the periodic boundary conditions by creating four dislocation dipoles per cell. This allows our method to be extended to mixed dislocations.

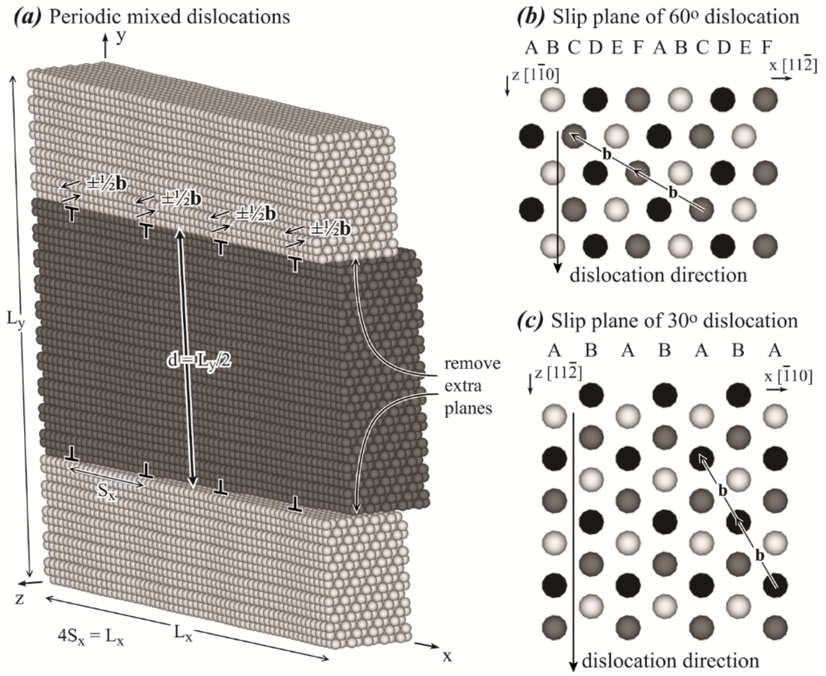

Figure 15. Geometry for mixed dislocations: (a) Three-dimensional configuration; (b) top-view of 60º dislocation slip plane; and (c) top-view of 30º dislocation slip plane.

The approach described above requires adding more dislocations for mixed dislocations. To reduce computational cost, we propose to use non-orthogonal systems where one axis aligns with the dislocation line, another axis aligns with the Burgers vector, and the third axis is perpendicular to the slip plane. Such a system would require only one dislocation dipole per cell in exactly the same way as shown in Figure 15. Non-orthogonal systems, which do not create error for defect-free systems, may introduce artificial effects at the presence of defects (although for specific configurations, the errors are not significant [71]). Since the goal of present chapter is to create most accurate results to confidently explore the physics of dislocation core energies, we use orthogonal systems.

3.2.3. Time-Averaged MD Simulations

We found that while MS energy calculations can give low relative errors, they produce large total errors that increase statistically as the system dimension increases [73]. This is not satisfactory for calculating dislocation energies that are related to total energies of (dislocated and perfect) systems. Time-averaged properties of long time MD simulations are found, somewhat surprisingly, to have virtually zero total errors regardless of the system dimensions [73]. Additional advantages of MD simulations are their incorporation of the finite temperature effect, and their abilities to fully relax the structures. All energies presented in this paper are time-averaged properties from long MD simulations. Unless otherwise indicated, our simulations us the NPT (constant number of atoms, pressure, and temperature) ensemble with the dimension in the dislocation line direction (*z*) further fixed to match the plane strain assumption used in the classical dislocation theories. For comparison, some simulations allow the z dimension to change. The initial crystals are created using an aluminum lattice constant of 4.0494 Å.

3.3. Results and Discussion

3.3.1. Edge Dislocations

Two series of simulations are performed. The crystal used in the first series contains 72 $\left(2\bar{2}0\right)$ planes in x, 174 $\left(111\right)$ planes in y, 30 $\left(\bar{2}\bar{2}4\right)$ in z, and the dislocation dipole distance d varies from 3, 15, 33, 51, 69, 87, 105, 123, 141, 159, to 171 $\left(111\right)$ planes. MD simulations are then performed for 4 ns at 300 K. After discarding the first 0.8 ns to establish the equilibrium, the system energy and dimension are averaged over all the time steps for the remaining 3.2 ns. The same simulations are repeated for both perfect and dislocated crystals, and dislocation energies are calculated based on the energy difference. Standard deviation of the calculations is also estimated by sampling the data at different times. The results of dislocation energies and their standard deviation are shown as a function of dislocation dipole distance in Figure 16(a) using the data points, where the line is based on Eq. (C1) that is fitted to the MD data.

It can be seen from Figure 16(a) that our MD data virtually have no error bars, and all the data points fall right on top of the continuum line. The same simulations are repeated at 100 K, and the results are included in Figure 16(a). It can be seen that temperature does not impact dislocation energies.

Figure 16(a) shows that the dislocation energies are symmetric with respect to dipole distance d. This is because when d is small, dislocations and their dipole counterparts annihilate leading to a small energy. When *d* is large (close to L_y), dislocations and their other dipole counterparts (periodic images) also annihilate leading to a small energy. Capturing this phenomenon is one strong validation of our MD data.

In the second series, the crystal contains 174 $\left(111\right)$ planes in y, 30 $\left(\bar{2}\bar{2}4\right)$ in z, the dislocation dipole distance d equals 87 $\left(111\right)$ planes, and the x dimension of the system varies from 120, 144, 168, 192, 216, to 240 $\left(2\bar{2}0\right)$ planes. The same method is used to calculate the dislocation energies. The corresponding results are shown in Figure 16(b) as a function of dislocation lateral spacing S_x (= L_x). Again, Figure 16(b) indicates that the MD results virtually have no error bars.

(a) Effect of dislocation spacing d

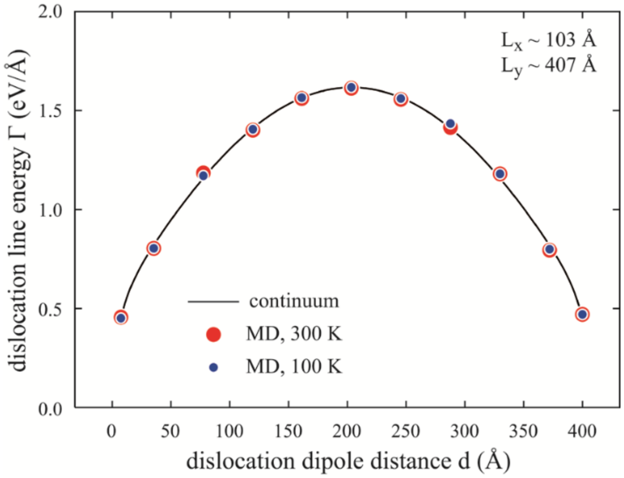

(b) Effect of system size L_x

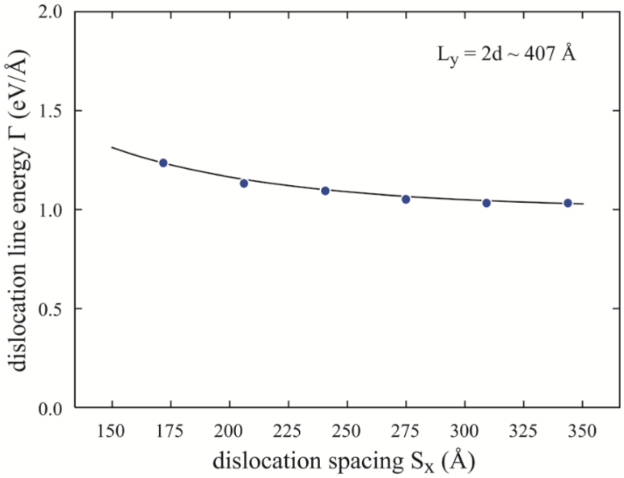

Edge dislocation, core radius 10 Å, core energy 0.622 eV/Å

Figure 16. Edge dislocation line energy as a function of (a) dislocation dipole distance d and (b) dislocation spacing S_x (= L_x).

3.3.2. 60º, 30º,10.89º, 49.11º, 70.89º Dislocations

(a) 30°, 60° dislocations

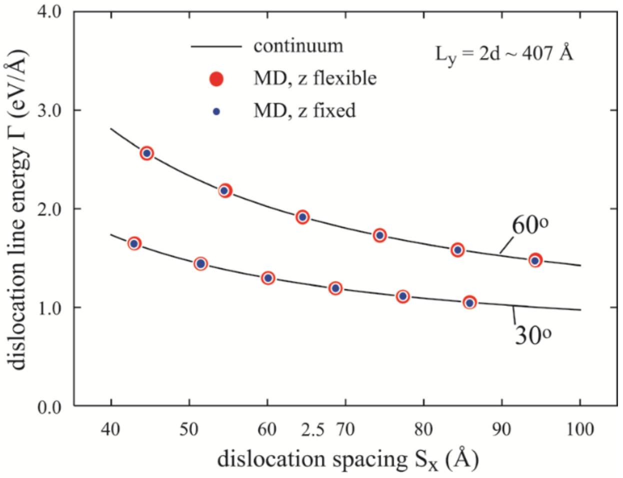

(b) 10.89°, 49.11°, 70.89° dislocations

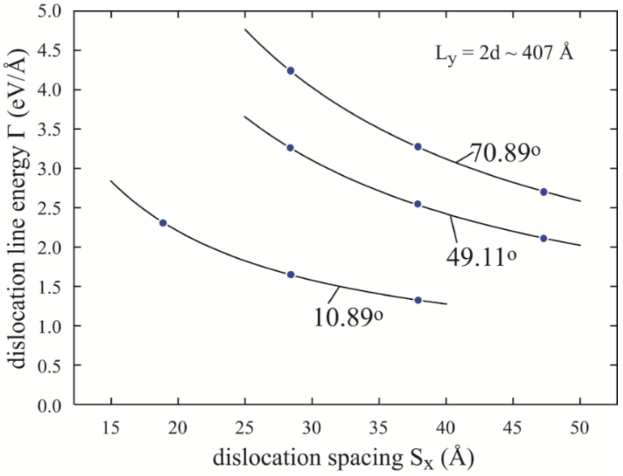

Figure 17. Line energies as a function of dislocation spacing S_x for (a) 30° and 60°, and (b) 10.89°, 49.11°, and 70.89° dislocations.

We found that our method cannot be used for 0° screw dislocations because the two opposite dislocations will cross slip and annihilate. However, we do perform calculations for 60°, 30°, 10.89°, 49.11°, and 70.89° dislocations. The crystal for the 60° *d* contains 174 (111) planes in *y* direction, 16 $(2\bar{2}0)$ in *z*, the dislocation dipole distance d equals 87 (111) planes, and the *x* dimension of the system varies from 216, 264, 312, 360, 408, to 456 $(22\bar{4})$ planes. The crystal for the 30° dislocation simulations contains 174 (111) planes in *y*, 30 $(22\bar{4})$ in *z*, *d* equals 87 (111) planes, and the *x* dimension varies from 120, 144, 168, 192, 216, to 240 $(\bar{2}20)$ planes. Four dislocation dipoles are created in the computational cell as shown in Figure 15(a), so that the lateral dislocation spacing S_x equals $L_x/4$. The crystals used for the 10.89°, 49.11°, and 70.89° dislocations are the same, containing 174 (111) planes in *y* direction, 54 $\left(\frac{9}{7}\frac{36}{7}-\frac{45}{7}\right)$ planes in

z, 87 (111) planes for the dislocation dipole distance d, and various x dimensions of the system from 1050, 1575, 2100, to 2625 $\left(-\frac{45}{7}\frac{30}{7}\frac{15}{7}\right)$ planes. The only difference is that the 10.89º, 49.11º, and 70.89º dislocations correspond to Burger vectors of $\check{b} = \left[01\bar{1}\right]a/2$, $\left[\bar{1}01\right]a/2$, and $\left[\bar{1}10\right]a/2$, respectively. Unlike the 60º and 30º dislocations, the non-regular angles 10.89º, 49.11º, and 70.89º require 28 dislocation dipoles to be used in the computational cell to maintain periodic boundary conditions. As a result, $S_x = L_x/28$. Following the same method as described above, dislocation energies are calculated as a function of S_x and the results are shown in Figure 17(a) regular angles and in Figure 17(b) for non-regular angles. Again the MD results have imperceptible error bars.

For comparison, some 60º and 30º simulations are performed with flexible z dimension, and the results are included in Figure 17(a). It can be seen that whether the z dimension is fixed or not does not impact the results, validating the plain strain simplification assumed in classical dislocation theories.

3.3.3. Dislocation Core Energies

The continuum expression for energy of periodic dislocation arrays, Eq. (C1), involves three parameters: dislocation core radius r_0, core energy E_c, and elastic constants G and ν. The parameters can be fitted to MD data. By concept, any value can be used for r_0 as long as it is above a threshold so that the material outside of the r_0 core can be well fitted to the linear elastic theory. Ideally, small r_0 is preferred so that the volume that is not treated by the linear elastic theory is minimized. We find that when r_0 is significantly smaller than ca. 1 Å, the fit is not satisfactory. However, when r_0 exceeds ca. 1 Å, the fit is extremely good. Table 2shows our fitted dislocation core energies and elastic constants obtained for different dislocations and different chosen core radii. Remarkably, the elastic constants do not depend on core radii, confirming that all the core radii are above the threshold. Although the lines in Figure 16 and Figure 17 are produced at r_0 = 10 Å, there is really no difference if other r_0 is used. The convergence to a single core energy at different dislocation spacings for a given dislocation direction and a given core radius, the convergence to a single set of elastic constants for all dislocation spacings, orientations, and core radius, and the exact match between MD results and continuum expression, strongly validate our methods and results.

Table 2. Dislocation core energy E_c (eV/ Å) determined at six selected values of core radius r_0 (Å).

Dislocation	E_c (eV/ Å)						G (eV/Å^3)	ν
	$r_0 = 1$	$r_0 = 5$	$r_0 = 10$	$r_0 = 15$	$r_0 = 20$	$r_0 = 25$		
10.89º	0.156	0.368	0.457	0.507	0.542	0.568	0.178	0.404
30.00º	0.147	0.363	0.454	0.506	0.541	0.568		
49.11º	0.187	0.474	0.595	0.663	0.711	0.746		
60.00º	0.179	0.458	0.575	0.642	0.687	0.722		
70.89º	0.214	0.546	0.686	0.765	0.820	0.860		
90.00º	0.192	0.502	0.632	0.706	0.757	0.795		

3.3.4. Dislocation Line Direction Revisited

Table 2indicates an interesting phenomenon not revealed in previous studies: dislocation core energies exhibit local minimums at regular angles such as 30º, 60º, and 90º, and they abruptly increase when dislocation line deviates from these angles. Because our data is strongly validated, and our method does not even involve such tangential approximation as non-orthogonal periodic cells, this phenomenon is real. To understand the physics of this phenomenon, we compare three consecutive (111) planes of the crystals used for regular (30º) and no-regular (10.89º, 49.11º, 70.89º) angle dislocations in Figure 18(a) and 5(b), where the vertical lines indicate the planes containing the dislocations. There are at least two mechanisms contributing to high energies for non-regular angles. First, the plane separating left and right sides of the dislocation is $\{112\}$ for the 30º dislocation and $\{145\}$for the three non-regular angle dislocations. High index planes mean more cross-plane bonds and therefore distorting these bonds due to the formation of a dislocation will result in a higher energy. This is similar to the high surface energies for high index surfaces except that the cross-plane bonds are broken rather than distorted in the surface case. Second, it can be seen that atoms marked with the red dots are equivalent in the 30º case, but non-equivalent in the non-regular angle case. This means that the dislocation will cause different distortion energies for atoms in the non-regular angle cases. Violating the equal-partition of energies also results in high total energies.

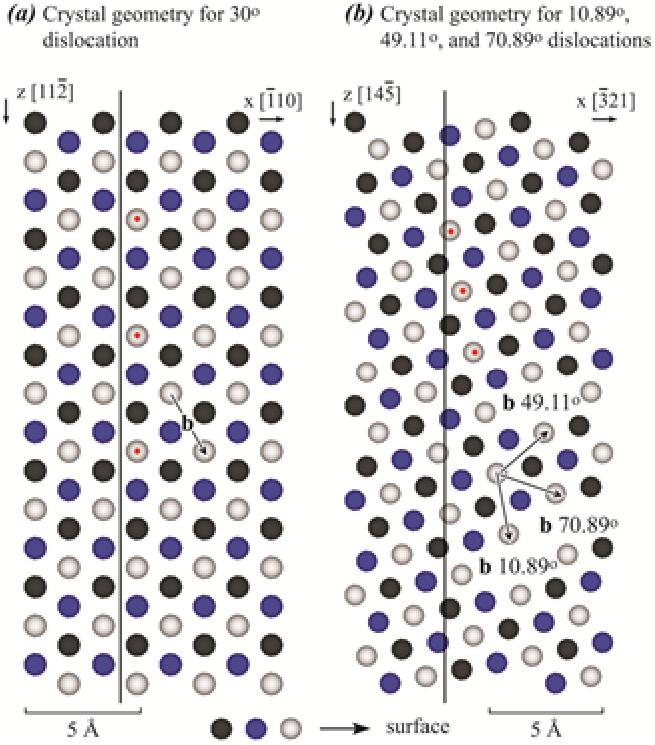
(a) Crystal geometry for 30º dislocation

(b) Crystal geometry for 10.89º, 49.11º, and 70.89º dislocations

Figure 18. Examination of geometries of dislocation lines: (a) 30º dislocation; (b) 10.89º, 49.11º, 70.89º dislocations.

3.3.5. A mode for Dislocation Core Energy as a Function of Direction β

The results discussed above indicate that dislocations strictly constructed along non-regular angles have high energies. These dislocations are unlikely to be observed in reality because they will be relaxed to low energy segments. These insights allow a simple dislocation core energy model to be developed.

Assume that MD simulations produce N core energies $E_{c,i}$ for dislocations along N directions α_i, $i = 1, 2, \ldots, N$. We can always imagine that a dislocation with an arbitrary angle β can be split into these N segments with each segment having a length l_i. For these N segments to give a unit length of a dislocation along β, we have to satisfy geometry constraints $\cos\beta = \sum_{i=1}^{N} l_i \cos\alpha_i$ and $\sin\beta = \sum_{i=1}^{N} l_i \sin\alpha_i$. The energy of the total segments is then $E_{tot} = \sum_{i=1}^{N} l_i E_{c,i}$. Minimizing this energy with respect to l_i under the geometric constraints should give an "equilibrium" core energy seen in experiments. Further work is needed to validate this model.

3.4. Conclusions

A robust MD model has been developed to calculate the core energies of mixed dislocations. This model does not require continuum boundary conditions, and produces results with virtually no numerical errors. Based on a high-fidelity bond order potential, we have used this model to calculate dislocation core energies of aluminum as a function of dislocation angle β. The following conclusions have been obtained:

1. Dislocation core radius in aluminum is as small as $r_0 = 1$ Å;
2. Values of $r_0 > 1$ Å can also be used, but the additional volume added to the core satisfies the linear elastic theory;
3. Dislocation energy as a function of dislocation angle satisfies the $C_1 \cdot \cos^2\beta + C_2 \cdot \sin^2\beta$ law;
4. Dislocation energies are independent of temperature.

4. ADDITIONAL MOLECULAR DYNAMICS SIMULATIONS

This work is expected to be included in a number of future submissions to peer reviewed journal articles.

4.1. Hydrogen adsorption on clean Al surfaces

The primary focus of this project is exploring the interaction of H with Al-Cu binary surfaces. However, before exploring the binary system a detailed understanding of the pure Al surface must be established. To study these surface interactions, MD simulations explored the low energy H-surface configurations as well as the sticking coefficients of atomic H at different temperatures.

4.1.1. Hydrogen adatom energies and locations

To simulate the low energy configurations of atomic H on pure Al, an MD model of a clean free surface is employed. The free surface is constructed out of an MD cell which is periodic in two directions (x and z) with a free surface in the +/- y directions. The result of such a configuration is essentially a thin infinite plate with two free surfaces. Surfaces with either a [100] or [111] normals were explored. For the [100] surface, the crystal was oriented x=[100], y=[010], and z=[001], while the MD cell measured 4×16×4 lattices, with a lattice parameter defined by that of the potential. The cell was then completely populated in the x and z direction, but only within the middle 10 lattices in the y direction. This construction resulted in 3 lattice units of vacuum above and below the free surfaces and resulted in a slab with dimensions of 16.2 Å x 40.5 Å x 16.2 Å. For the [111] surface, the crystal was oriented $x=\left[\bar{1}\,\bar{1}\,2\right]$, $y=\left[1\,1\,1\right]$, and $z=\left[\bar{1}\,1\,0\right]$ again with a vacuum above and below the [111] surfaces. In this case the final dimensions of the crystal are 22.91 Å x 70.15 Å x 39.63 Å. As a check, before adding H to the surface, the surface energies were confirmed for these configurations as 0.0601 eV/Å^2 and 0.0528 eV/Å^2, for the [100] and [111] surfaces, respectively.

Each surface has the potential for an infinite number of adatom locations. However, only a few are considered stable with energies low enough to actually exist. The locations examined in this study are shown in Figure 19. The [111] surface has four potential stable adatom locations, bridge, hcp hollow, fcc hollow, and top. While the 100 surface has thre potentially stable locations, the bridge, hollow, and top locations. The energy of each H adatom location was calculated with molecular statics by placing a single H atom at each of the different adatom locations and calculating the change in the system energy. In order to prevent atoms from falling into lower energy sites, the displacement of the H were restricted to only allow movement in the direction orthogonal to the surface. The energies of each location are given in Table 3.

[111] [100]

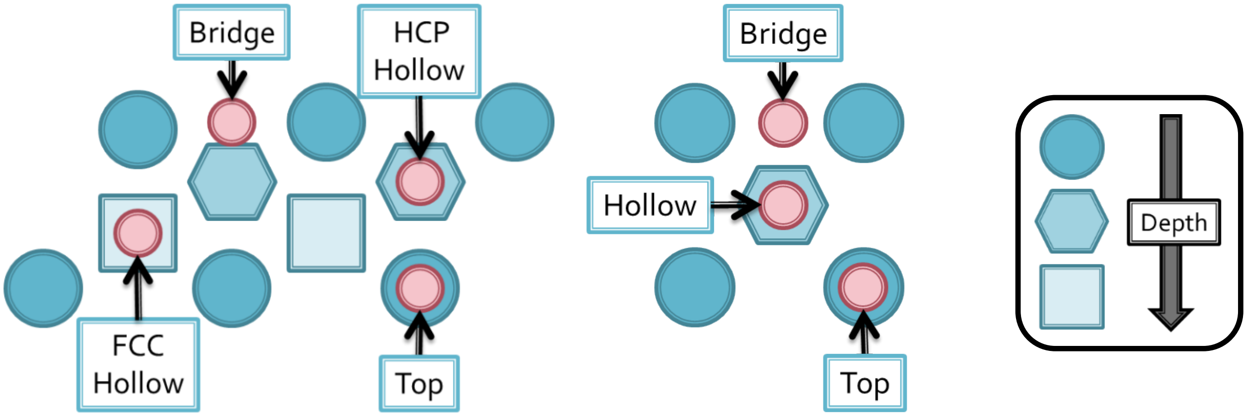

Figure 19. Schematic of the possible adatom locations for H (red) on Al (blue) [111] and [100] surfaces.

Table 3. Energy of different adatom locations for [100] and [111] surfaces. Low energy locations are bolded and italicized. The "*" indicates the low energy location as determined by DFT in this study.

[100] Surface	
Site	**Energy (eV)**
Top	-1.872
Hollow	-1.728
Bridge	***-2.038****
[111] Surface	
Site	**Energy (eV)**
Top	-1.728
HCP Hollow	-2.058
fcc Hollow	***-2.071***
Bridge	-1.464*

The low energy locations are the bridge and fcc hollow for the [100] and [111] surfaces, respectively. For the [100] surface, this result is in agreement with the DFT results performed here. Previous experiments have also predicted this location as a low energy site [74]. However, there is a discrepancy between this result and our experiments discussed in Section 6. Our experiments predict a hollow adatom location. This discrepancy is not fully understood and requires further analysis. For the [111] surface we predict an fcc hollow low energy location. However, this interaction is expected to be much more complicated. Studies have shown that the interaction between H and the Al[111] surface is highly reactive [75]. Further discussion of the high reactivity will be discussed below.

4.1.2. Hydrogen surface coverage at finite temperature

Beyond the low energy adatom locations, it is important to look at the effects of dynamics on adatom attachment. The technique described above restricts the atoms from moving out of the defined locations. It is likely that many of these locations are metastable and will not be seen in simulations performed at a finite temperature. With the energy of each adatom location calculated statically, the surface concentration can then be calculated with dynamics as a function of applied H pressure. The surface concentration is given as a percent monolayer, which is defined as the number of adsorbate atoms as a percent of the number of surface atoms.

To calculate the surface concentration, we use the same geometry as described above, for the Al surfaces. Atomic H is then introduced into the vacuum region with a velocity of 0.1 Å/ps, directed normal to the surface (-y). To keep H from leaving the cell, a reflective barrier is introduced at the top of cell, which confines the H to the simulation cell. Simulations were run in an NPT ensemble at various temperatures with a pressure of 1 bar in the lateral/periodic directions. To prevent the bulk aluminum from accelerating downward, 3 planes of atoms on the bottom of the simulation were fixed in place.

Over the course of the simulation, the system's temperature was trying to expand the aluminum, whereas the pressure induced by the hydrogen was trying to compress the aluminum. Therefore, after running each simulation, for each temperature and number of hydrogen atoms, we had to calculate the height of the surface.

In order to calculate the surface concentrations for these simulations, a definition of the top surface must be defined. As a result of the applied temperature and pressure the surface of the simulation expanded and fluctuated as a result of lattice expansion. This proved to be more challenging than expected, particularly for the (111) surfaces. During the simulations many of the Al atoms reacted with the H to produce alane compounds above the surface. The alane structures are very similar to those discussed in previous literature [75]. The formation of alanes move Al atoms above what would normally be considered the surface normal. This causes issues numerically for determining the absolute surface height. Ultimately the height of the surface at each timestep is the average of all Al atoms with a y coordinate within 1.5 Å of the initial maximum Al y value. The distance of each H relative to the Al surface is then calculated relative to this new surface height. All of the y coordinates of the hydrogen were collected into an array and a distribution plot was made. An example of one of these distribution functions is given in Figure 20. The curve is normalized such that the integral between any two heights is the number of hydrogen per cross-sectional area expected to be found between those heights.

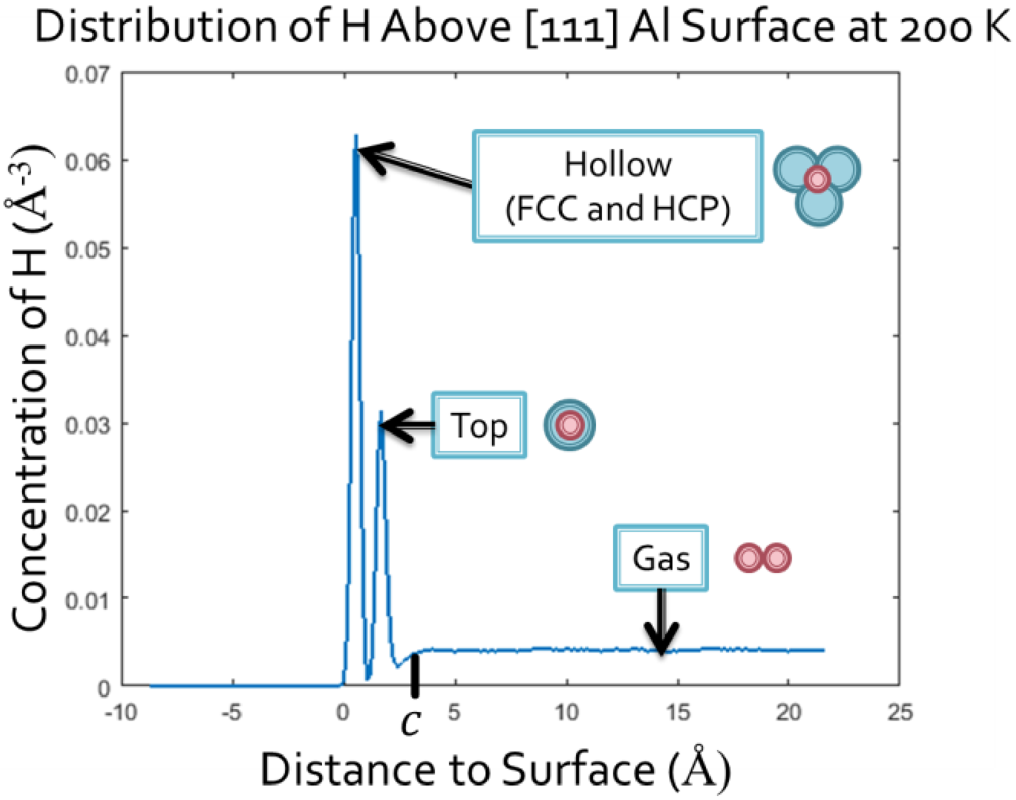

Figure 20. The distribution of hydrogen above a [111] Al surface at 200 K. The two peaks correspond to hollow and top sites, and the long tail corresponds to the uniformly distributed gas.

For the [111] surfaces, the distribution function had two peaks. Through visual inspection these to peaks were ascribed to the hollow and top locations, the two low energy locations according to our energy calculations. Hydrogen were observed in both the HCP and fcc hollow sites, which makes sense considering the energies for those sites are remarkably close. The long tail of the distribution plot represents the atoms not bound to the surface, which exist in a dimerized gas. The [100] distribution plots looked quite similar to the [111] plots, also having a two peaks. However, analysis of the visualizations showed that the [100] peaks corresponded to the bridge and top locations, which are also the low energy locations according to our above calculations.

To determine the atomic coverage of each surface, a cutoff is selected to separate the adatoms from the gas molecules. This cutoff (marked *c* in the above image) was chosen such that none of the peaks were cut off for all of the distribution graphs. Additionally, some atoms diffuse from the surface into the bulk, so any atoms below the surface were also omitted. Using these cutoffs, we were able to determine the number of adatoms at every timestep, which we did to ensure convergence. This analysis did result in a substantial amount of noise, which was attributed to gaseous molecules bouncing off the surface, entering the “bound” region for very brief amounts of time thus being counted in the total. To not include these, we used the mode of the entire trajectory to determine the number of adatoms.

This procedure was used to calculate the adatom concentrations for a range of temperatures from 100-500K with H molecules ranging from 25-250. Using the ideal gas law, we can then calculate the pressure of hydrogen as a function of the number of hydrogen and the temperature. The results for both the (111) and (100) surfaces are given in Figure 21 and Figure 22, respectively.

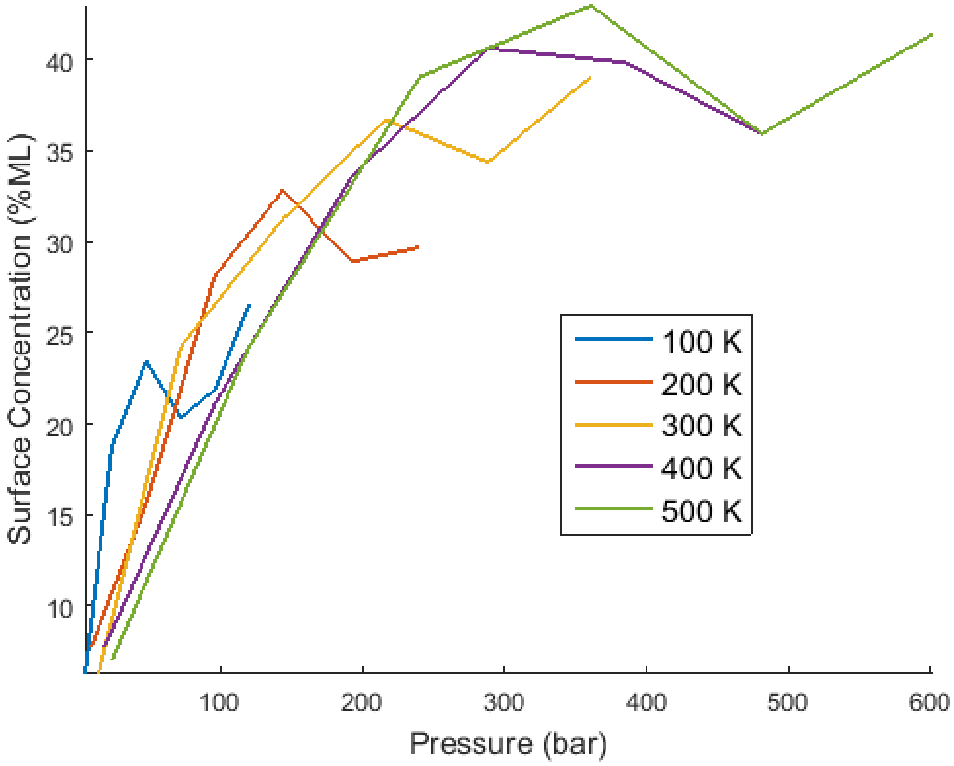

Figure 21. Surface concentration of hydrogen Al(111) surface as a function of the pressure of hydrogen at different temperatures.

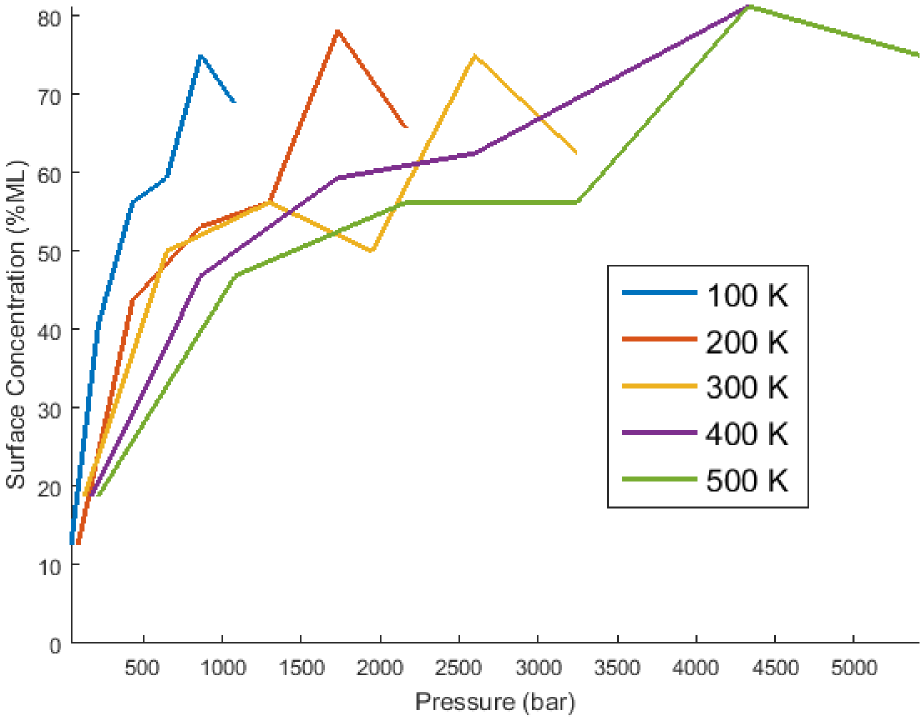

Figure 22. Surface concentration of hydrogen Al(100) surface as a function of the pressure of hydrogen at different temperatures.

These results are in relative agreement with the experiments that will be presented in Section 6. The surface concentrations do seem to increase with pressure up to some saturation limit, though the increase is notably not monotonic for all of the temperatures. This is most likely due to the statistics as the surfaces begin to saturate. Further analysis and simulations are necessary. Additionally, the concentration decreases as a function of temperature, which makes intuitive sense because at higher temperature, H atoms have more kinetic energy with which to escape the surface.

4.1.3. Trapping of H near Cu Precipitate

In order to understand the trapping site of atomic H within the precipitated alloy, MD simulations were performed to explore the energy landscape of the precipitate. A precipitate with a radius of 20 Å was inserted into an Al cell, similar to those cells constructed for the misfit strain simulations. These simulations show that the binding energy of the tetrahedral interstitial nearest the surface of the precipitate is significantly lower than the binding energy in the bulk Al lattice, by ~-2eV. This is attributed to fact that the precipitate causes a very high compressive stress in the Al lattice. The introduction of H near the precipitate assists in mitigating the lattice mismatch and ultimately reduces the strain energy near the precipitate.

4.2. Atomistic input for discrete dislocation simulations

4.2.1. Precipitate Misfit Strain

Precipitation is a primary hardening mechanism for AlCu alloys [76]. The movement of dislocations is the main method of plastic deformation in metals. Gaining an insight into the strength of AlCu alloys thus requires studying the movement of dislocations. Precipitates are a strengthening mechanism because they obstruct dislocation motion. A dislocation in fcc metals at ambient temperatures and typical applied stresses has ways to bypass preciptates in a glide plane: (i) it can bow around the precipitate, through-Orowan looping [77] (energetically favored for large precipitates), or (ii) it can cut through the precipitate (energetically favored for smaller precipitates.)

The number of dislocations and the size and number of precipitates that can be modelled by MD is extremely limited by computational time and memory. In order to gain insight into how the material behaves at the defect scale, a mesoscale model must be used. To this end, DD [57] simulations were used (see Section 5). For high fidelity DD simulation calibration, several parameters need to be determined from atomistics. These are the dislocation core energy and radius, already presented in Section 3, the misfit strain, the equilibrium position of the dislocation in the presence of a precipitate, and some quantitative understanding of the cutting interaction. The following is concerned with last three of these.

Molecular statics simulations were used to calculate the misfit strain of GP-I zone and GP-II zone precipitates. As a basis of comparison, a pure Al crystal of 100×100×100 lattices was simulated to calculate the lengths of the cell in the absence of any precipitates. To model a GP-I zone, atoms within a square of side length d, on a [100] plane, were replaced with Cu atoms and the system was relaxed. For each value of d (the precipitate diameter), the engineering strain $\varepsilon_x=((L_x-L_0)/L_0$ was calculated in each of the Cartesian directions. The value of the strain was then divided by the un-relaxed volume of the precipitate, taken to be the number of atoms in the precipitate times the volume per atom in bulk Al. The procedure is the same for GP-II zones, which are modelled as two circular disks of Cu of diameter d separated by three planes of Al. The results are given in Figure 23.

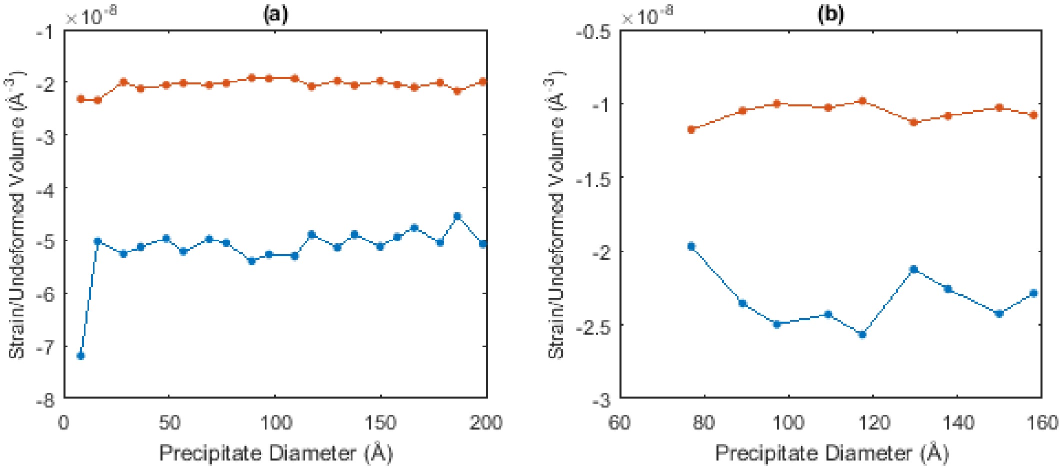

Figure 23. Misfit strain per unit undeformed volume in *x* (blue) and *y* (red) directions of GP-I zone (a) and GP-II zone (b) as a function of precipitate diameter (d)

After removing the first data point as an obvious outlier and averaging, the strains per simulation volume for the GP zone are $(-5.05\pm0.09)\times10^{-8}$ Å^{-3} and $(-2.04\pm0.05)\times10^{-8}$ Å^{-3} for the x and y directions, respectively. The x direction was chosen to be the direction normal to the plane of the precipitate, making the y and z directions parallel to the plane of the precipitate. The strains in the y and z directions were identical due to symmetry. For determining deformed volume of the GP-II zone all atoms—Al or Cu—within the cylinder bounded by the two disks of copper were considered part of the precipitate. The strain per simulation volume in the x and y directions are $(-2.3\pm0.1)\times 10^{-8}$ Å^{-3} and $(-1.06\pm0.04)\times 10^{-8}$ Å^{-3}. The use of these calculated strains will be discussed in Section 5.

4.2.2. Equilibrium dislocation precipitate configuration

As a point of comparison with DD, the equilibrium position of a dislocation when placed in a cell with a GP-I zone was determined. The isolated dislocations are constructed using the same technique as described by Zhou [78]. A precipitate with a radius of 40Å is then inserted into the cell, similarly to the process described in the previous discussion. In order make sure our results were not dependent on the size of the simulation box, five simulations of different dimensions were run (see Table 4). In addition, to ensure that the equilibrium position of the dislocation was not dependent on the initial configuration of the system, several additional simulations of constant size were ran with different initial positions of the precipitate and the dislocation. Simulations were run in an NPT (constant pressure and temperature) ensemble at 10 K under 1 bar of isotropic stress for 100 ps of simulated time.

Table 4. Dimensions of the different simulations run and the results of the dislocation precipitate interaction.

Sim #	X (Å)	Y (Å)	Z(Å)	Result of Simulation
1	271.966	168.5128	118.92	Dislocation cut precipitate
2	548.156	308.79	118.9824	Dislocation cut precipitate
3	271.966	168.345	237.918	Dislocation cut precipitate
4	1098	589.378	119.0136	Dislocation moving in direction of cutting precipitates
5	273.324	168.345	475.836	Dislocation cut precipitate

At the end of the trajectory, the dislocations in all of the simulations had either lodged themselves inside the precipitate with both Shockley partials having cut through the precipitate or were moving in the direction of lodging themselves in the precipitate. This attraction and lodging is independent of the starting location of the dislocation and precipitate. With the implementation of periodic boundary conditions along the dislocation line and the direction of the Burgers vector, implies that the dislocation is attracted to one side of the precipitate and repelled from the other direction. The comparison of these results with the DD simulations is presented in Section 5.

4.2.3. Dislocation cutting stress

The final information necessary for performing high fidelity DD simulations is the cutting force. This set of simulations presented to different problems. First, because one side of the precipitate attracts a dislocation it is nearly impossible to get a cutting stress in that direction. Secondly, thermal and pressure fluctuations resulted in very inconsistent results when employing MD simulations. Additionally, DD simulations incorporate temperature through mobility laws and thermal activation parameters. Ideally, zero temperature simulations would result in a better comparison to DD. To resolve the first issue, stress is applied to the simulation to drive the edge dislocation towards the repulsive side of the precipitate. This offers a more reasonable method for extracting a cutting stress. The second issue is resolved by performing iterative molecular statics simulations. Force is added in opposite directions to the top and bottom atoms creating the free surfaces in small increments. After the application of force, the system is minimized and the stress is determined for the fully minimized configuration. The atomic positions are inspected and it is determined whether or not cutting has occurred. If cutting occurs, the force increment is refined to have a higher resolution for the stress definition. If cutting has not occurred, the force is increased and the minimization continues.

The cutting was analyzed for three different cell sizes and three different cutting locations, along the precipitate. The results from these cutting simulations are given in Table 4.

Table 5. Cutting stress as determined from atomistic simulations of a GP-I Al-Cu precipitate by a pure edge dislocation at different heights of different simulation cell lengths.

		Precipitate Height (Å)		
		-20	0	20
		Cutting Stress (MPa)		
Cell Length (Å)	118.92	272.4768	325.8363	336.0547
	237.918	136.2843	168.0271	163.4861
	475.836	72.6605	90.8255	86.2843

These simulations suggest that with increasing cell size, or decreasing precipitate density, the cutting stress goes down. Additionally the cutting height for these simulations does not result in significantly different results. This is a product of the atomistic simulations having discrete properties. By simulating a circular precipitate with a small radius (40Å), results in a circle with small differences in thicknesses. These results are further put into context in Section 5.

5. DISLOCATION DYNAMICS SIMULATIONS OF AL-CU ALLOYS

5.1. Introduction

Dislocation dynamics (DD) is a tool for studying the behavior of networks of dislocation lines at the length scale of a few microns and the time scale of a few microseconds. With the ability to provide insight into the mechanics of dislocation interactions at these scales, DD can be used to understand the physics of strengthening and toughening in crystalline solids. In the context of this project, DD is a tool for taking insights gained from atomistic simulations of dislocation-precipitate and dislocation-hydrogen interactions, and assessing the resulting impacts on mechanical properties. Thus, DD provides a critical link between basic dislocation interactions and their mechanical consequences.

To date, a number of researchers have utilized DD simulations to study precipitation-strengthened materials [79–82]. However, these approaches have a number of shortcomings that make them inappropriate for Al-Cu alloys. First, mainly spherical precipitates have been considered to date, and since precipitates in the Al-Cu system (GP zones, θ”, θ’, θ) are disk-shaped platelets this leads to a significant error in their geometric representation. Second, while they consider purely dilatational misfits, we will show that Al-Cu precipitates have strongly non-dilatational misfits, and neglecting this can lead to large errors in the longer-ranged dislocation-precipitate interactions. And lastly, some existing algorithms may miss dislocation-precipitate contact interactions if the time step size is too large. Missing these “collisions” between dislocations and precipitates can lead to significant inaccuracies, for example failing to capture the formation of a dislocation loop around a precipitate, called an Orowan loop.

Given the shortcomings found in existing DD precipitate formulations, we have developed a new formulation. The goal of this formulation was to allow for DD simulations with arbitrarily shaped ellipsoids having arbitrary misfits with the lattice of the matrix material they are embedded in, and to ensure reliable dislocation-precipitate collision detection. We choose an ellipsoidal precipitate geometry because ellipsoidal inclusions (and inhomogeneities) are well studied in elasticity theory and many common precipitate geometries are well approximated as ellipsoids (e.g. disk, rods, spheres etc.) Another important feature of dislocation-precipitate interactions is cutting: after a dislocation collides with a precipitate, it may shear through the precipitate if the applied stress is large enough and if the energy barrier is below that for Orowan bypass. Capturing these cutting events is important, so we have also made this a feature of the new formulation. In order to maximize the accuracy of our model, we have utilized atomistic simulations to determine parameters characterizing the dislocation-precipitate interactions and validate our approach.

Below we present our new approach as follows. First we discuss the basic features of our dislocation-precipitates interaction algorithm and its implementation. Next we discuss how parameters for this model can be extracted from atomistic simulations, and give results for the Al-Cu system. In the final section, we present a sample large-scale DD simulation of an underaged Al-Cu alloy.

5.2. Algorithm and Implementation

There are four basic elements to our formulations for dislocation-precipitate interactions: 1) detection of collisions between dislocation segments and precipitates, 2) remeshing the dislocation line discretization at the surface of precipitates, 3) cutting of precipitates by dislocations, and 4) computation of forces on dislocations due to precipitate misfit fields. These additions provide a framework that can capture a large number of dislocation-precipitate processes, such as cutting, Orowan looping, or obstacle avoidance by climb or cross-slip (if dislocation lines are able to climb or cross-slip). Each of these elements is given a subsection below. In the final subsection we discuss the parallel implementation of the formulation in the DD code ParaDiS.

5.2.1. Collision Detection

When a dislocation encounters the stress-field of a precipitate that has a nonzero cutting resistance, it will initially be arrested at the surface of the precipitate. We can think of this as the dislocation line "colliding" with the surface of the precipitate. Being able to detect these collisions is critical to the accuracy of the DD code—if collisions are missed important physics will be absent in the simulation results.

In ParaDiS, dislocations are discretized into linear segments. Thus, detecting collisions between precipitates and dislocations means detecting collisions between ellipsoids and line segments. To reliably detect collisions we employ the interval halving method [83]. This approach was recently applied to dislocation segment-segment collisions [84], and here we extend it to dislocation-precipitate collisions for the first time. In contrast to other commonly used methods, the interval halving method is capable of detecting a collision at any point in time over a given time step based on a segment's nodal positions at the old and current time steps, making it significantly more accurate and reliable. After a collision is detected, a new node is introduced at the collision point and is pinned in place until the "release" code (discussed below) lifts the pinned constraint.

All that the interval method requires is the ability to compute the minimum separation distance between a dislocation segment and an ellipsoidal precipitate at any point in time. Computation of this distance requires solving a constrained quadratic minimization problem [85]. In the case of a spherical precipitate, this problem can be solved analytically; however for a general ellipsoid, it must be solved numerically. A numerical solution is obtained as follows. First, the minimum distance between any point in space and the ellipsoid is obtained using Newton's method with a Lagrange multiplier. With this capability, the distance can be minimized along a line segment using the golden section search method—a derivative-free minimization algorithm.

5.2.2. Remeshing

While the collision code reliably detects and handles collisions between dislocation segments and precipitates, it does not control the quality of the discretization of the collided segments. Control of the discretization is important for a number of reasons. For one, adding dislocation segments to the simulation adds computational expense because they introduce additional forces, making unnecessarily small segments undesirable. At the same time, if the segments are too large, the representation of the surface of the precipitate may be poor, making the associated dislocation stress field inaccurate. And finally, the forces on the segments pinned at the precipitate are used to decide if a cutting event should occur: a poor discretization will lead to inaccurate cutting computations.

Remeshing is already applied to the dislocation lines in the bulk (not pinned at precipitates) to control the discretization. However the algorithm and parameters used are often inappropriate for precipitates; for example, nodes may be added or removed based on how segments are moving, so pinned segments are ignored. Therefore, we have developed a separate “precipitate remeshing” code which operates on the basis of two new parameters: the minimum angle allowed between segments pinned on the same precipitate and the minimum segment length allowed on a precipitate. Nodes are added or removed until these criteria are satisfied.

5.2.3. Cutting and Releasing Nodes

Once a node has been pinned at the surface of a precipitate, it can be released if one of two conditions is met: 1) the dislocation’s velocity upon being released is in the direction of the precipitate’s local outward normal (moving away from the precipitate) or 2) a *cutting event* occurs. Determining whether a cutting event occurs requires input from a cutting model. We can think of the cutting model as providing information regarding the short-ranged interactions between a dislocation and a precipitate, which occur while the dislocation is in contact with and/or penetrating the precipitate. Many different short-ranged mechanisms are known to resist penetration and cutting of a precipitate by a dislocation (e.g. chemical, order, and stacking fault strengthening) [86]. Given the complexity of these mechanisms, and the fact that usually many mechanisms operate simultaneously, we advocate the use of atomistic simulations for developing a cutting model. Two simple cutting models are as follows. An athermal strength model would decide whether a cutting event occurs when the force exerted by a dislocation line on a precipitate exceeds the strength of the precipitate. This model is temperature insensitive and deterministic. In contrast, a thermally-activated model would predict cutting stochastically on the basis of the energy barrier associated with a cutting event. Generally dislocation-precipitate interactions are thought to be athermal [87], but the cutting of weak and/or small precipitates may be thermally-activated [86,88]. In Section 1.3 we will demonstrate the merit of an athermal strength model to characterize the cutting of GPI zones by comparing with atomistic simulations at 0 K.

5.2.4. Misfit Force Calculation

Precipitates are known to interact at a distance with dislocations via two mechanisms: coherent lattice misfit and elastic modulus mismatch. If a precipitate is coherent (as with GP zone and θ” precipitates) or semicoherent (as with θ’ precipitates), and has a lattice constant different from the parent (matrix) material, the resulting misfit generates a stress field in the matrix that can exert forces on dislocation lines. The character of this misfit field is set by the type of misfit (e.g. dilatational and/or shear) and the shape of the precipitate. Additionally, if the precipitate has elastic constants that differ from the matrix, forces can arise on dislocations as well. This elastic mismatch effect is complex to address for arbitrary geometries and usually requires the use of a finite element solver (or some other numerical technique), making it computationally complex and expensive. Furthermore, long-ranged modulus mismatch effects are often second-order relative to misfit effects [86]. For these reasons, we will neglect long-ranged modulus mismatch effects and focus only on the misfit force. Note that short-ranged modulus mismatch effects may still be incorporated through the precipitate cutting model.

The stress field of a misfit ellipsoidal inclusion in an infinite body is known analytically [89], however the resulting expressions are complex and difficult to implement in DD. Instead, we have developed a numerical approach for computing the misfit stress field based on adaptive quadrature over a sphere. The method allows for arbitrarily shaped ellipsoids with arbitrary misfit. The basic idea is to compute the stress field σ_{ij} based on the tractions exerted by the precipitate on the matrix (the hole it has been fit into) using the elastic Green's function. This requires evaluating the integral [90].

$$\sigma_{ij} = \frac{1}{2} C_{ijkl} \int_{S_0} C_{mnop} \varepsilon^*_{op} n_m(\mathbf{x}')[G_{kn,l}(\mathbf{x},\mathbf{x}') + G_{ln,k}(\mathbf{x},\mathbf{x}')] dS(\mathbf{x}') \tag{2}$$

where C_{ijkl} is the stiffness tensor, ε^*_{ij} is the eigenstrain tensor characterizing the misfit of the precipitate, $\mathbf{n}(\mathbf{x})$ is the outward normal unit vector of the precipitate, G_{ij} is the isotropic elastic Green's function (known analytically [89]), and S_0 is the surface of the precipitate. Here we use Einstein notation (repeated indices are summed) and commas denote differentiation. This integral can be evaluated numerically in MATLAB using the quad2d function after transforming the domain of integration to a sphere using spherical coordinates. The stress field for any precipitate can then be pretabulated and interpolated during a DD simulation. To get the force on a node, the stress field is integrated along the segment weighted by the linear shape function for that node; this is accomplished using Gauss quadrature.

5.2.5. Implementation in ParaDiS

Implementation of the new precipitates algorithm in ParaDiS required the introduction of a new *Precipitates* module, a misfit force subroutine, and two new input files with associated parsers. During each time step after time integration for that step, the *Precipitates* module is called, which then handles dislocation-precipitate collisions, remeshes segments on precipitates, and then handles release of nodes pinned at precipitates. When a node becomes pinned at a precipitate, the *prec* flag for that node is set to the index for that precipitate, allowing us to keep track of which nodes are pinned on which precipitates. Additionally, each time the nodal forces are computed the misfit force subroutine is called. To specify the distribution of precipitates for a simulation, a *.prec* file must be specified. In this file, the position, shape, orientation, eigenstrain, and cutting parameters for each precipitate are provided. Additionally, a list of *precstress* files may be specified in the *.prec* file. These files contain the pretabulated misfit stress fields; the code will associate each precipitate with its appropriate stress table during initialization. Parallelizing this implementation required two minor additions to the code: MPI send buffers for nodal data had to be extended to include their *prec* flags and a *Change_Prec* operation had to be defined for communicating to other domains when nodes become pinned at or released from precipitates. The newly developed code is a available for use upon request (rbsills@sandia.gov).

5.3. Atomistic Computation of DD Parameters

Since DD is a mesoscale model, it requires input from more fundamental models in order to capture the relevant physics. Here we demonstrate how atomistic simulations can be utilized to provide these inputs. First we discuss computation of the dislocation core energy in pure aluminum, which is necessary to compute core forces in DD. Then we discuss two features of dislocation-precipitate interactions that are difficult to determine without an atomistic model: a precipitate's misfit eigenstrain and the precipitate cutting interaction.

5.3.1. Core Energy

The core energy is defined as the energy of a dislocation that is not characterized by elasticity theory. The structure at the core is sensitive to nonlinear interatomic interactions, and requires a model with atomistic resolution to characterize. Core energies can be computed atomistically at a variety of dislocation character angles φ (angle between the line direction and the Burgers vector), and using this data we can develop a core energy function $E_c(\varphi)$. The core force resulting from $E_c(\varphi)$ exerted on a node by a (linear) segment connected to that node with (unit) line direction **t** and Burgers vector **b** is

$$\mathbf{f} = -E_c(\theta_i)\ \mathbf{t} + \frac{dE_c(\theta_i)}{d\theta}\left(\frac{\mathbf{b}_e}{\left\|\mathbf{b}_e\right\|}\right) \tag{3}$$

where $\mathbf{b}_e$ is the edge component of the Burgers vector, $\mathbf{b}_e = \mathbf{b} - (\mathbf{b}\bullet\mathbf{t})\mathbf{t}$, and the character angle of segment is $\varphi_i = \cos^{-1}(\mathbf{b}\bullet\mathbf{t})$.The first term acts to shorten the segment and reduce its line energy (line tension) and the second term acts to rotate the segment into orientations with lower energy.

At the time of the report, some complexities of the core energies for aluminum as calculated from MD have not been resolved (See Chapter 3 for details). The MD simulations are showing that the dislocation core energy does not increase monotonically with character angle. Without complete understanding of the physics responsible for this result, we are not comfortable implementing these results in the DD simulations. Instead, we use the default (deWit and Koehler) line tension model in ParaDiS for core forces, scaled according to the computed edge dislocation core energy of 0.3963 eV/Å for a core radius of 1 *b*.

5.3.2. Precipitate Misfit

The eigenstrain tensor that characterizes the misfit for a precipitate is an important DD input. For large coherent precipitates, the eigenstrain is defined by the lattice mismatch between the precipitate and matrix:

$$\varepsilon_{ij}^{\mathrm{coh}} = \frac{a_P - a_M}{a_M} \tag{4}$$

where a_P and a_M are the lattice constants for the precipitate and matrix, respectively. However, when the precipitate is small, the interactions between the precipitate and matrix atoms at the surface of the precipitate become very important, and the simple coherency argument (based on bulk atomic interactions dominating) breaks down. In this case it is necessary to compute the misfit atomistically.

It turns out that the eigenstrain for an arbitrary precipitate can be computed quite easily using atomistics. To do so, all one has to do is insert a precipitate in a simulation cell under periodic boundary conditions, and then relax the cell at zero or finite temperature. The resulting strain of the cell after relaxation is $\varepsilon_{ij}^{\text{cell}}$. If the initial volume of the cell is V and the volume of matrix removed to introduce the precipitate is v, then the eigenstrain for the precipitate is simply

$$\varepsilon_{ij}^{*} = \frac{V}{v}\varepsilon_{ij}^{\text{cell}} . \tag{5}$$

We have used this approach to compute the eigenstrains for GP-I precipitates of various radii. These precipitates can be characterized by a diagonal eigenstrain tensor when the coordinate system is in the plane the platelet. The results are presented in Figure 24. Also shown with a solid black line are the nominal "coherency" eigenstrains using Eq. (4). The eigenstrains in the plane of the precipitates (ε_{xx}^{*} and ε_{yy}^{*}) and the nominal eigenstrain are very close since the bulk interactions dominate them (they do not match exactly because of the modulus difference between the precipitate and matrix). The eigenstrain component normal to the plane (ε_{zz}^{*}) is drastically different however, demonstrating the importance of using an atomistic approach for computing misfit eigenstrains. When the precipitate is larger than a few Å the eigenstrains are independent of radius.

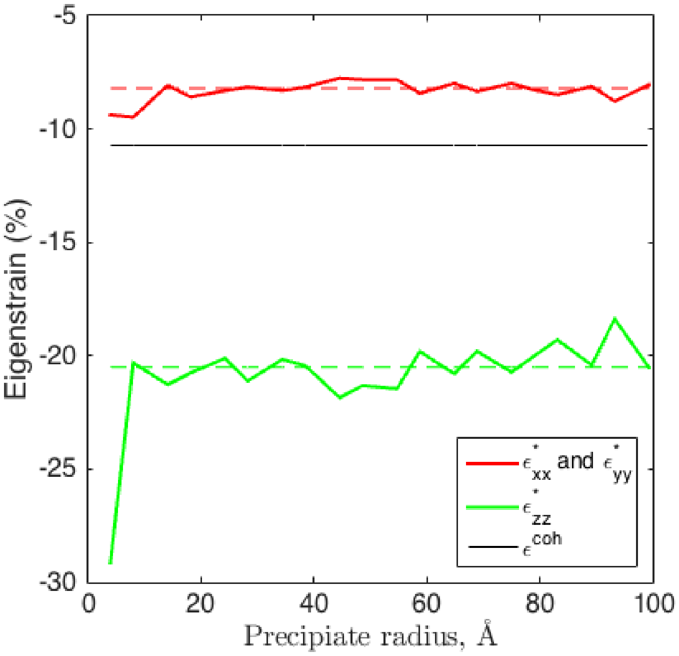

Figure 24. GP-I zone eigenstrains computed from atomistic simulations as a function of zone radius. The zone lies in the *x-y* plane. The solid black line is the coherency eigenstrain using Eq. (3). Dashed lines show values used in DD simulations.

5.3.3. Cutting Strength of a GP-I Zone

As a preliminary investigation for a precipitate cutting model, atomistic simulations were run with an edge dislocation at 0 K to investigate the cutting strength of a GPI zone. With a precipitate radius of 40 Å, simulations were run with simulation cell sizes (precipitate spacings) of 119, 234, and 476 Å. Other details of these simulations are discussed in Section 4.2.3. With the geometry used, the dislocation is attracted to one side of the precipitate and repulsed from the other. A shear stress was imposed on the system so that the dislocation was forced to cut on the repulsive side. The minimum applied shear stress necessary for cutting for each spacing is presented in Table 5. It can be seen that the cutting stress varies with spacing, meaning it is not a unique parameter governing the strength of the precipitate.

Table 6. MD and DD GP-I zone cutting simulations results

Precipitate Spacing (Å)	MD Cutting Stress (MPa)	DD Cutting Force (nN)
119	326	0.33 ± 0.05
234	168	2.2 ± 0.2
476	90.8	2.4 ± 0.2

Using the new DD model with the misfit and core energy computed from atomistics (discussed above), the exact same cutting simulations were run. A radius aspect ratio of 0.1 was used to imitate the geometry of the GP-I zone. With the precipitate treated as impenetrable, the MD cutting stress was imposed and the simulation was run until the equilibrium configuration was achieved under that stress. The total cutting force exerted on the precipitate by the dislocation, computed as the sum of forces acting orthogonal to the precipitate's surface at each node in contact with the precipitate, was then computed in that configuration; those results are presented in Table 5. Snapshots from the cutting configurations for MD and DD are shown in Figure 25.

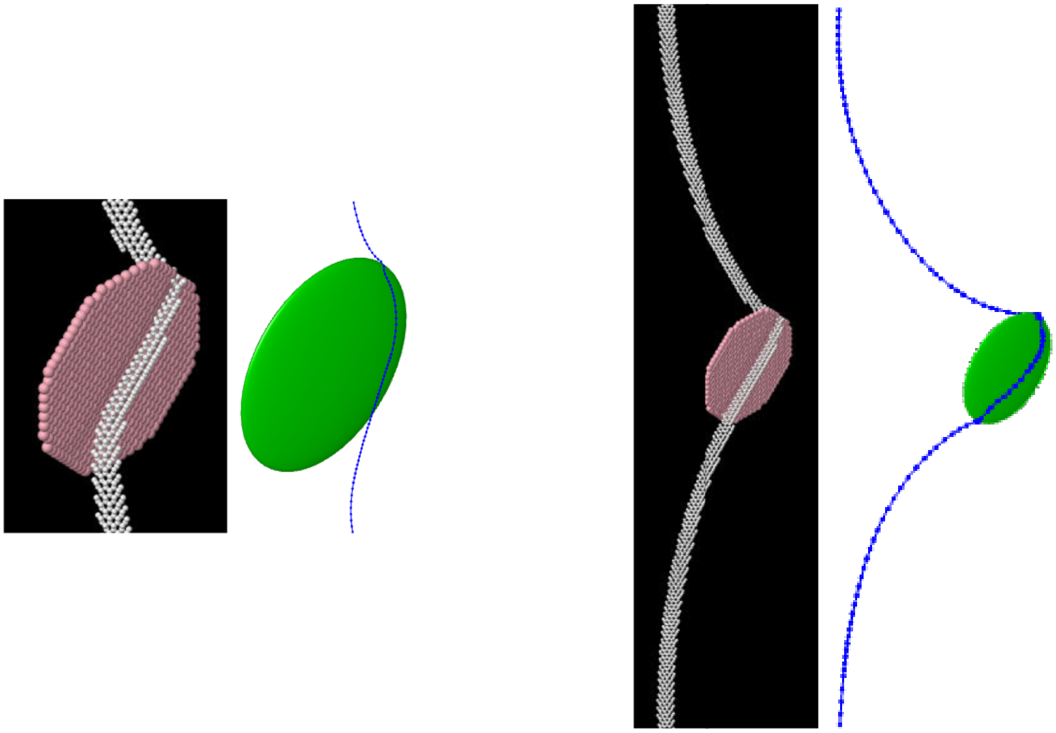

(a) (b)

Figure 25. Configurations just below the cutting stress from MD and DD simulations with precipitate spacings of (a) 119 Å and (b) and 476 Å.

If the cutting force is a unique metric characterizing the strength of a precipitate, then it should be independent of the precipitate spacing. We see that the cutting forces from the two larger box sizes are indeed close to each other, however the result from the smallest box size is about an order of magnitude lower. Examining the DD configurations, we see that the misfit field prevents the dislocation line from contacting the precipitate over a large area, in conflict with the MD results where the dislocation appears to be in full contact. Additionally, the dislocation line bows out more with DD than is observed atomistically. Perhaps a more careful selection of the precipitate aspect ratio would remedy these issues. Further investigation is necessary to resolve these differences and develop a robust cutting model for DD.

5.4. Large-scale Simulation

To showcase the new capabilities within ParaDiS, a large-scale simulation was performed using a precipitate microstructure emulating that found in underaged Al-Cu alloys. This microstructure consists of GP-I zones in randomly oriented {001} planes with radii selected at random from the Wagner-Lifshitz-Slyozov distribution using an average radius of 50 Å and distributed in space according to the method developed by Mohles and Fruhstorfer [91]. The misfit shown in Figure 24 was used for misfit field computation. An aspect ratio of 0.1 was used for the major and minor precipitate radii. Due to the issues discussed above, cutting was not allowed and precipitates were treated as impenetrable. A cubic simulation cell 0.25 μm long on each edge containing 1728 precipitates was used; this gave a number density of 1.1×10^5 μm^{-3}, as may be observed in an underaged Al-4 wt. pct. Cu alloy [88].

Dislocation lines were only allowed to move in their predefined glide planes (no cross-slip). The atomistically computed edge core energy was used for core force computation. The dislocation microstructure started as 10 randomly orientated lines of random character. A stress of 500 MPa was applied in the [001] direction to load the system in uniaxial tension. The resulting microstructure after 0.2% plastic strain is presented in Figure 26. The simulation was run in parallel using 8 CPUs. Using the newly developed code, large-scale simulations of the sort presented here can be used to study strengthening and hardening in precipitation-strengthened materials.

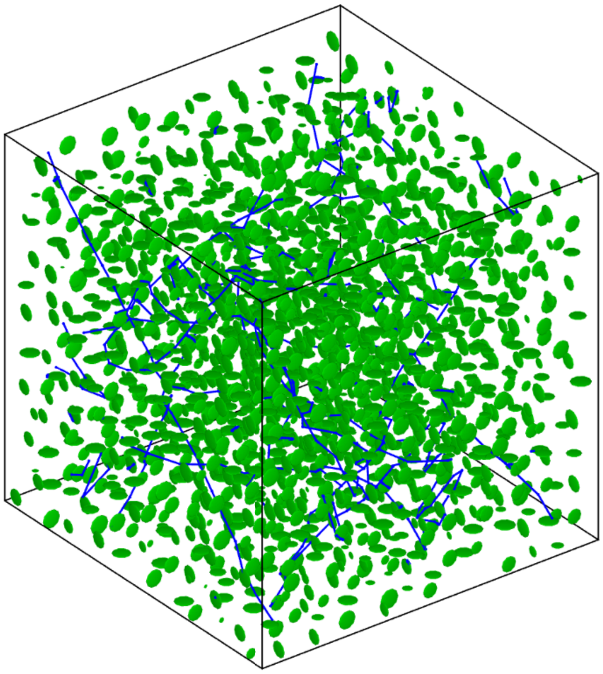

Figure 26. DD simulation of an underaged Al-Cu alloy after 0.2% plastic strain.

6. ANALYSIS OF GAS-SURFACE INTERACTIONS

6.1. Introduction

Predicting how structural materials will respond to exposure to high pressure hydrogen environments requires a comprehensive understanding of the gas-solid interface. In the case of aluminum surfaces, two factors serve to enhance their "immunity" to hydrogen effects. First, the sticking coefficient for molecular hydrogen (H_2) on atomically clean surfaces is known to be quite low (estimated to be $<10^{-4}$) [92]. (Here we define the sticking coefficient, S_0, as the ratio of H that adsorb on the surface to the arriving flux.) Furthermore, oxygen has a strong affinity for Al surfaces; for most metals this introduces a considerable barrier for dissociative chemisorption.

Rigorously asserting that the above conditions hold for a wide range of structural material compositions, pressures, and thermal conditions is more challenging. For example, while the sticking coefficient of $H_2(g)$ is quite low, atomic hydrogen readily sticks to Al surfaces (i.e. $S_0 = 0.6$ for both Al(100) and Al(111) [92].) While this is not a problem for protium (H) or deuterium (D), the low energy β-decay of tritium (T) ensures that a small fraction of the gas is in atomic form. Therefore, for reservoirs containing tritium, an enhanced pathway for hydrogen isotope diffusion into the material may be present. Another consideration is that alloying species common to Al alloys (e.g. Cu, Fe, and Ti) are known to readily dissociate hydrogen isotopes, and may in a similar manner promote hydrogen adsorption. Furthermore, the robustness of the oxygen passivation layer, particularly in conditions where the surface under load, is also of concern, as elegantly described by Somerday and colleagues for the specialized case of cyclical loading of stainless steels in mixed H+O environments [93]. Ion beam analysis has provided evidence that hydrogen can even diffuse through oxides as a molecule [94] under appropriate conditions.

We envision that the following key science questions need to be addressed:

- What are the binding energies of atomic H to practical Al alloy surfaces containing defects?
- What are the activation energies for atomic H migration on Al surfaces and how do these parameters affect surface recombination kinetics?
- How do adsorbed species (e.g. oxides) prevent the uptake of hydrogen? What are pathways by which H can enter a passivated surface? (These questions are particularly important for T_2 gas, which contains a small fraction of atomic T that can readily adsorb on clean Al.)
- Under what conditions is enhancement of dissociative chemisorption of H_2 on Al surfaces by alloy species (particularly Cu) a significant effect? (Can we bound the problem to state that for most Al-alloys this is not a concern?)
- Do a small number of defect sites (e.g. step edges or vacancies) enhance H_2 dissociation on Al or provide energetically favorable pathways for H to enter the bulk material?

Fundamental modeling and experimental studies, such as the work undertaken in this project, can be used to bound the conditions for where hydrogen exposure will not pose a threat to structural metals. In this section, we describe experimental measurements of how H and D adsorb on and bind to Al and Al-Cu alloys. Detection of hydrogen on surfaces is notoriously difficult, and most available analysis tools provide only indirect information, or overwhelmed by substrate effects. In this work, we use two complementary forms of low energy ion beam analysis: low energy ion scattering (LEIS) and direct recoil spectrometry (DRS). Both techniques are unique for being able to *directly* detect adsorbed hydrogen, and provide isotopic sensitivity. Compositional information is obtained from the energies of the scattered and recoiled particles, which are typically detected with an electrostatic analyzer or time of flight system. Structural information is provided through "shadowing" effects, where surface atoms are blocked from the analysis beam by their neighbors.

6.2. Experimental Configuration

All of the experimental work described here was performed using an angle-resolved ion energy spectrometer (ARIES). This instrument uses an ion source (Colutron) to produce a well-defined, mass-separated beam of low-energy (0.5 – 3 keV) He+ and Ne+ ions. The ion energy spread, measured by passing the beam directly into an electrostatic analyzer (ESA), spanned ~ 1 eV FWHM for a 3 keV He^+ beam. Neutral particles are removed by electrostatically deflecting the charged species through a mechanical bend into an analysis chamber maintained at a base pressure of 5×10^{-10} torr. The sample itself is mounted to a manipulator that allows for translation along 3 axes, as well as polar (α) and azimuthal (ϕ) rotations. (See Figure 26 for angle definitions.) To ensure a uniform distribution of ion flux on the sample surface, we raster the beam over a 2 mm × 2 mm rectangular area and adjust the raster amplitude to compensate for varying polar angle. Typical ion fluxes for this system range between 10^{13} – 10^{14} $cm^{-2}s^{-1}$. The angular position of the aforementioned ESA may be adjusted via a rotating platform over a range of $15° \leq \theta \leq 90°$. As an additional check of the surface cleanliness, an electron gun for Auger electron spectroscopy (AES) is also available. Samples can be readily heated to 1000 °C using a small button-style heater mounted beneath the sample.

As part of this LDRD effort, we added a cryogenic cooling stage to the sample manipulator. This enabled cooling of sample to -160 °C through contact with a liquid nitrogen reservoir. The advantage of such measurements was that it allows for the accumulation of much higher hydrogen concentrations on the surface than is possible at room temperature. The new configuration and stage are shown in Figure 27.

Electrostatic analyzers only detect charged particles, which may comprise just a small fraction of the scattered and recoiled species. To supplement the incomplete picture provided by the ESA, we developed a time-of-flight (TOF) spectroscopy system capable of detecting both ions and neutrals. To enable coaxial ICISS measurements, we added a 40 mm dia. annular micro-channel plate at the exit of the ion source to detect of directly backscattered particles over a range of $165° \leq \theta \leq 180°$. The TOF system uses a fast-rise time pulse generator to apply a high voltage to a set of steering plates within the beam line, sweeping the ions across an aperture downstream. This creates a well-defined ion packet (< 7 ns pulse width) that travels through the ion optics to the sample. After the ion packet scatters from the surface, the aforementioned MCP detector collects the scattered particles. The pulse produced by ion impact on the MCP passes through conditioning electronics and into a time-to-amplitude converter measures the corresponding flight times, which are finally histogrammed by a multi-channel analyzer. Taking into account the dead times of the detector and electronics, the above process can be repeated up to a rate of about 30 kHz.

6.2.1. Surface Preparation

We considered high-index single crystal surfaces, including the (100) and (111) planes, as well as highly stepped surfaces (332) with ordered defects. We also considered samples of the AA2219 alloy as well as a custom-prepared Al-Cu containing (20% Cu at.) All single crystal materials were prepared by MaTecK GmbH. The crystals were polished and aligned to within 0.1° of the desired plane and secured to our manipulator with thin tantalum wire along a small grove at the crystal periphery to avoid any shadowing effects from the incident ion beam. Our procedure for cleaning the Al surfaces included cycles of low energy sputtering and annealing to 550 °C. Prior helium-atom scattering measurements by Hinch *et al*. [95] indicate that Al(332) surfaces tend to form facets depending on the annealing temperature, with "freezing" of the step structure for $T_{surf} < 550$ K. With this in mind, we used rapid cooling as a means to stabilize the steps.

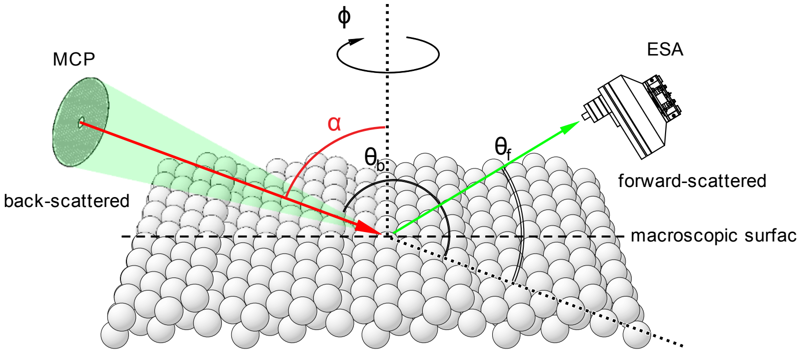

Figure 27. Analysis geometry for LEIS and DRS measurements. Note in particular the angular definitions: the beam incidence angle (α), crystal azimuth (ϕ), and detection angle (θ).

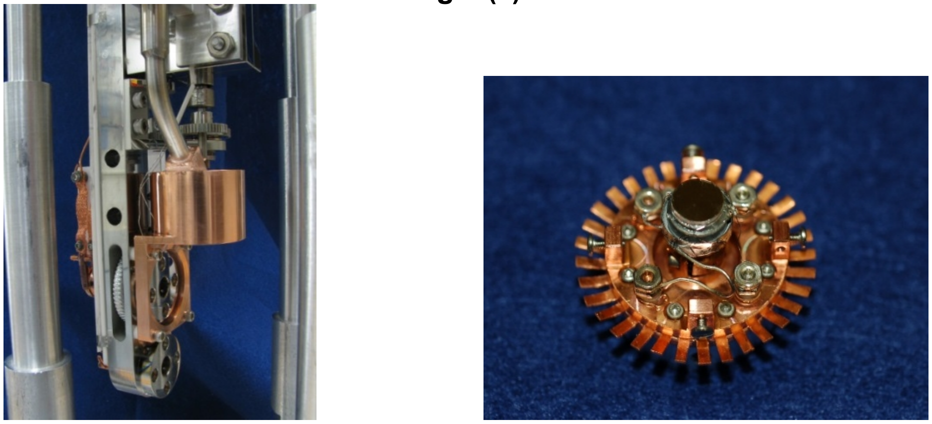

Figure 28. Low temperature sample stage for analysis of surfaces at cryogenic temperatures. Image on the left shows the manipulator with modified LN2 reservoir, whereas the image on the right shows a sample holder with Cu spring to provide contact with Cu heat sink.

6.3. Analysis of Adsorbed Hydrogen

As previously discussed, information from LEIS/DRS on surface composition is obtained from a scattered/recoiled ion energy spectrum. An example is shown in Figure 28 for H adsorption on an $Al_{0.8}Cu_{0.2}$ alloy. In this case, all scattered and recoiled particle energies are normalized to the energy of the incident beam (3 keV Ne^+.) Distinct peaks associated with the Ne^+ ions scattering from Al and Cu present on the surface are visible at relative energies of E/E_0=0.53 and E/E_0=0.68, respectively. These are close to the theoretical values for these energies determined from classical kinematics, taking into account a small amount of inelastic loss. (Please see Appendix A for further details.) A smaller peak associated with Al appears at E/E_0=0.24; this corresponds to doubly ionized (Ne^{++}) that pass through our detector at approximate half of the pass voltage of Ne^+.

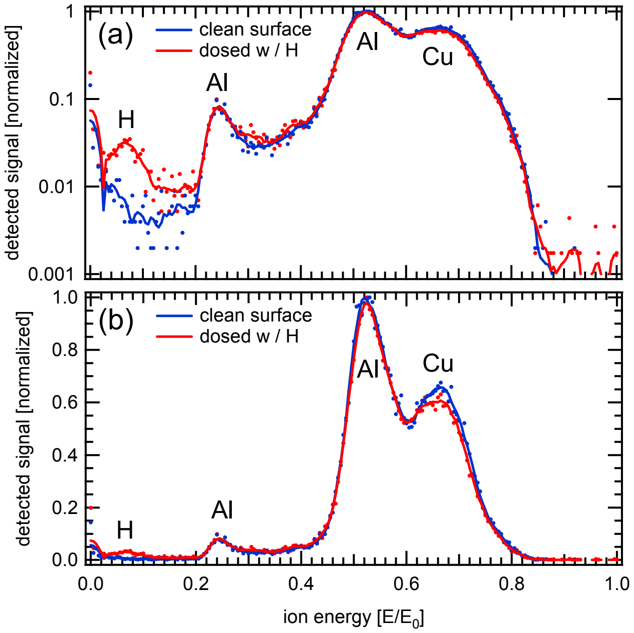

Figure 29. Ion energy spectrum showing composition of Al-Cu alloy surface. Note that (a) is shown in log coordinates to emphasize the shape of the H peak, whereas (b) is in linear coordinates to illustrate the subtle decrease in scattering from Cu after adsorption. It is possible that H prefer to bind in sites closer in proximity to Cu atoms, and are largely responsible for this decrease.

Our ARIES system includes an atomic doser based on the design described in Ref. [96]. It consists of a tungsten capillary (heated to a temperature of 1650 °C by energetic electron bombardment) to dissociate the hydrogen gas. We adjusted the hydrogen flow rate through the capillary to vary the atomic flux to the surface. This flow rate was monitored indirectly using the QMS within the main analysis chamber; a H_2(g) partial pressure of 10^{-6} torr corresponds to an H atomic flux of 10^{14} H cm^{-2} s^{-1}.

Consistent with expectation, simply introducing H_2(g) into the vacuum system produced no discernible change in the intensity of the various scattering and recoil signals. However, as illustrated in Figure 28, introducing atomic hydrogen at a low level increases the H recoil signal while decreasing the scattering/recoiling associated with the Al-Cu substrate. Even when the sample was not exposed to atomic hydrogen a recoil signal associated with hydrogen was still present. Possible sources of this signal include residual water vapor chemisorbed on the surface, hydrogen dissolved within the bulk migrating to surface sites, or dissociation of hydrogen by the various filaments within our vacuum system.

We observed rapid adsorption of hydrogen when an atomic doser is used. However, it reaches saturation within a few seconds at room temperature. A fundamental question is: how much hydrogen is present on the surface under these conditions? For LEIS/DRS measurements, the surface coverage (θ_H) may be estimated from:

$$\theta_H = \frac{S_H / (p_H \sigma_H)}{S_{Be} / (p_{Be} \sigma_{Be}) + S_H / (p_H \sigma_H)} \tag{6}$$

In the above expression, the signal strength (S_i) is measured directly, and collision cross-sections (σ_i) are well-established quantities. The cross sections can be calculated based on the observation angle θ, the incident ion energy of E_0, and assuming a suitable inter atomic potential (typically based on the Ziegler-Biersack-Littmark empirical fit [97]). The ion survival probability (p_i) refers to the likelihood that a recoiled particle will emerge from a surface as an ion rather than a neutral particle. While the survival probabilities are subject to some uncertainty, a number of relatively straightforward approximations are available, as discussed in Ref. [98]. Taking this into account, and considering that the collision cross-sections for H and Al are comparable, we must conclude that the saturation coverage of H is well below a single monolayer ($\theta_H < 0.2$) at room temperature for the dosing conditions considered here. Further increases in dosing flux resulting only in chemisorption of impurity species.

For the conditions of this experiment, the incident atomic hydrogen flux produced by our doser is 10-100 times larger than the ion flux from our analysis beam. With this in mind, that ion-induced desorption would result in a negligible perturbation to the adsorbed hydrogen layer. We observed initial rapid uptake of H on the surface, consistent with previous findings that suggest the sticking coefficient for the clean surface is near unity [92].

It is intriguing to note that while adsorption of hydrogen results in a slight decrease in the scattering peaks from both the both of the main metallic species within the surface, it has a more pronounced effect on the Cu signal. One possible explanation for this is that the H is in closer proximity to the Cu atoms, suggesting a preference for binding to those atoms.

6.3.1. *Adsorption Profiles*

In a high-pressure environment, the surface concentration of hydrogen on the surface is likely to be much higher than in the UHV conditions of the experiments described here. Fortunately, it is possible to increase the surface coverage through cryogenic cooling of the substrate. The advantage of undertaking this step is that it will enable us to calibrate our analysis beam signals for saturation coverage. Furthermore, it is expected that surface diffusion will be minimized under these circumstances. As will be discussed later in this section, this may enable easier identification of hydrogen binding sites on surfaces.

The higher surface concentration of hydrogen achievable with cryogenic cooling is evident from Figure 29. In this case, the surface was brought to 450 °C and sputter-cleaned. The temperature was slowly reduced to room temperature, at which point liquid nitrogen was used to further cool to -160 °C. The concentration at this temperature was approximately 6 times higher than at 25 °C, consistent with our prior estimates from the scattering and recoil peak heights.

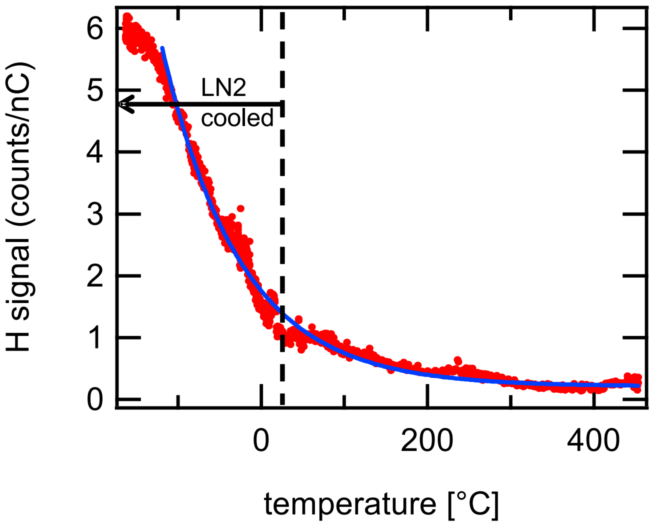

Figure 30. Adsorption profile for H on an Al-Cu specimen. The data plotted represents the height of the recoiled hydrogen signal as a function of temperature. Note that the sample was heated to 450 °C, sputter cleaned, and subsequently cooled with liquid nitrogen to -160 °C. The blue curve represents a two-term exponential fit.

To provide insight into surface recombination and diffusion, we adopted a method of controlled adsorption experiments based on a technique developed in Ref. [99]. We assessed the adsorbed hydrogen concentration by monitoring the height of recoiled hydrogen peak, using a 3 keV Ne^+ analysis beam at an incidence angle of α=80°. We heated each specimen to 450 °C and exposed it to a constant flux of D and H. The sample was held at this temperature for 30 min while it was sputter cleaned. At 450 °C, the adsorbed H concentration was near the detection limit of our instrument. Afterward, we cooled each sample to room temperature at different linear rates ranging between 1.8 - 14.2 °C/min, corresponding to ramp times between 15 min – 2 hr.

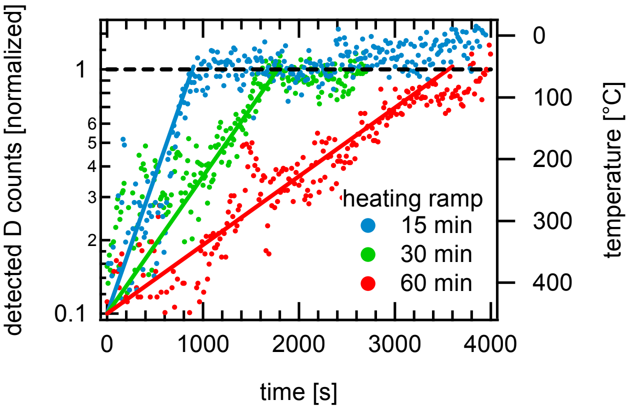

Figure 31. Adsorption isobars for varying heating rates. Here D adsorption is monitored on an Al(100) crystal using a 3 keV Ne+ ion beam.

The adsorption isobars for each thermal ramp are illustrated in Figure 30. To emphasize the relative behavior between each run, the various curves are normalized to the surface coverage at

50°C. In Figure 31, the adsorption curves are rendered in Arrhenius plots. It is striking to note that for all four thermal ramps, the same basic adsorption curve shape is evident, with the adsorbed concentrations following a linear dependent behavior over the entire temperature range considered here. Of particular interest was to assess the effect of alloying species on the kinetics of hydrogen adsorption. For this purpose we also considered the aforementioned Al-Cu alloy, and a comparable set of adsorption isobars are shown in Figure 31b. We observed a relatively modest difference between the two cases, indicating that the addition of Cu has only a modest influence on the uptake of H.

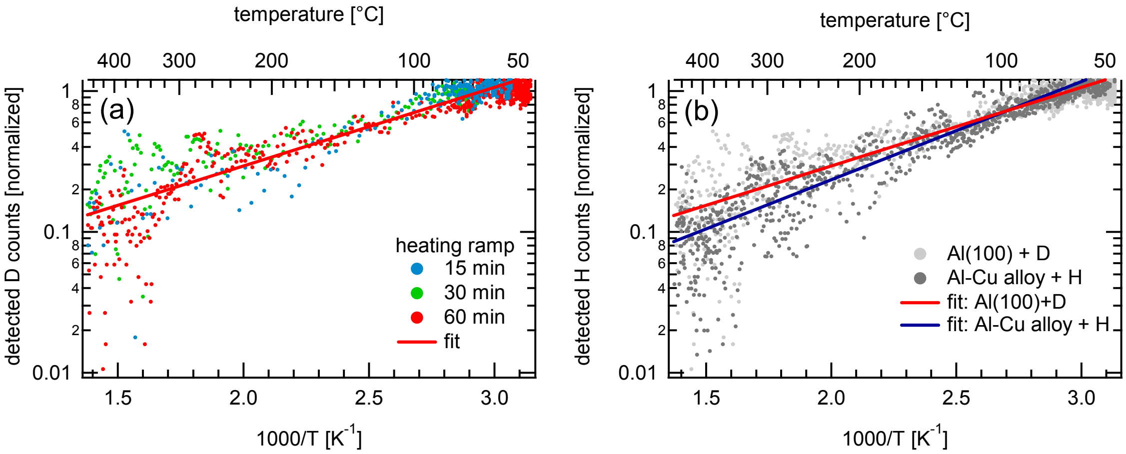

Figure 32. Adsorption isobars for adsorption on (a) an Al(100) single crystal. Similar data is shown in the comparison plot in (b) for the Al-Cu alloy. Only a modest difference between the two cases was noted.

It is important to note that the concentration of Cu in the material tested here (~20%) far exceeds the amount that would be expected in practical alloys. Hence, from the conditions considered here, it appears that Cu would not act as a catalyst for hydrogen dissociation on the surface in an appreciable manner.

6.4. Adsorbate Binding Configuration

The binding configuration of hydrogen on surfaces can be used to validate fundamental MD and DFT models, as well as to provide insight into energetics. As discussed in the introductory section, the LEIS and DRS also provide information on the structure of surfaces. We previously developed a technique for determining the binding configuration of hydrogen on surfaces: low-energy channeling of ions [14]. The basic approach involves considering ion beams at grazing incidence directed along open channels on low index surfaces. The presence of adsorbed H along these open surface directions results in de-channeling of ions, as well as enhanced recoil signals, both effects that can be observed with LEIS. We refer the reader to Ref. [14] for a more comprehensive description.

In Figure 32, we illustrate several possible configurations for hydrogen adsorbed on Al(100), including top, 4-fold hollow, and 2-fold bridge sites. (Here the small markers indicate the adsorbed H, whereas the larger markers denote the first-layer Al atoms.) The arrows indicate prominent open channels for ion focusing. Whether hydrogen is present along these directions depends on the binding site occupied.

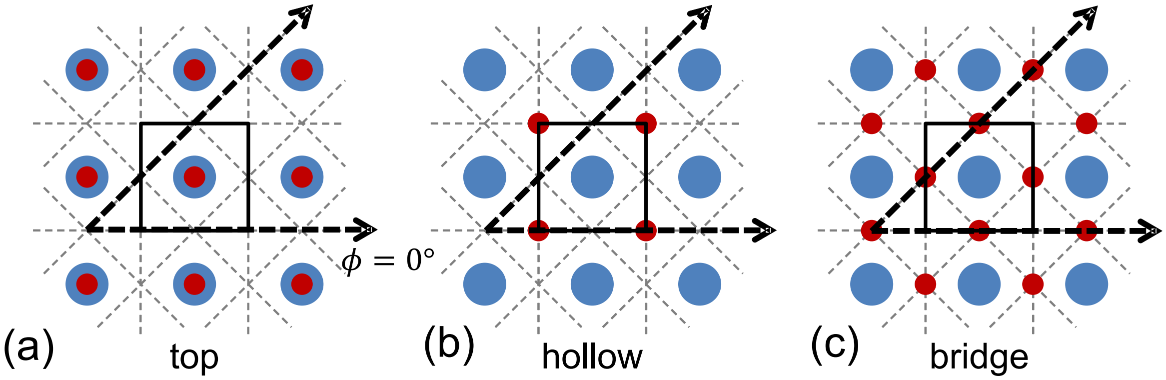

Figure 33. Potential high-symmetry binding sites for hydrogen adsorption on Al(100).

Generally a first step in this procedure would involve a detailed analysis of ion focusing effects on the substrate. Details of this process for Al are described in a prior publication [100].

By rotating the crystal azimuth (i.e. varying ϕ, as shown in Figure 26) one can examine these effects in further detail. First consider the variation in Al peak height shown below in Figure 33. Note that ϕ = 0° is referenced to the direction indicated in Figure 32(a). Immediately evident is the four-fold symmetry of this crystal plane. Furthermore, along directions corresponding to ϕ = 0°, 90°, 180, etc., there a considerable drop in scattering from surface Al atoms. This is due to shadowing effects; the Al surface atoms are blocked from the incident Ne^+ by adjacent atoms.

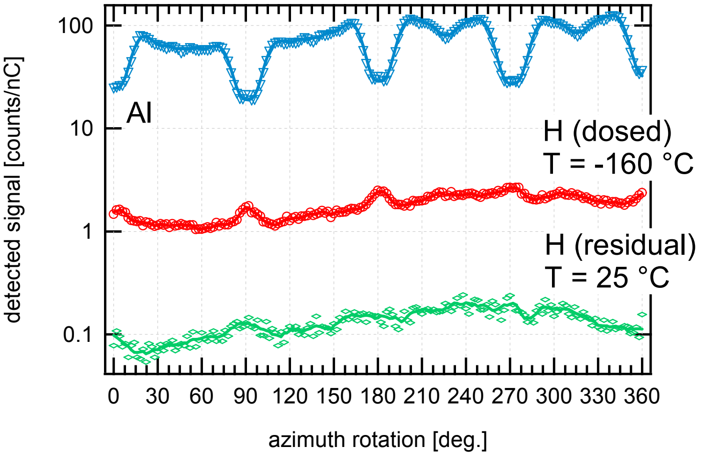

Figure 34. Azimuthal scan showing variation in Al and H signals as a function of crystal azimuth (ϕ).

The variation in hydrogen recoil intensity is also shown in Figure 33. At 25 °C, the signal is essentially lacks structure, and appears as a uniform background. However, cooling the sample to -160 °C allows for much more accumulation of hydrogen on the surface. In addition, a clear structure appears: maxima in the recoiled hydrogen intensity appear along open channels at ϕ = 0°, 90°, 180°, etc.

The enhanced hydrogen recoil signals at 90° intervals indicate hydrogen resides in hollow sites on the surface. Had hydrogen been in bridge sites, we would have expected to see enhancement in hydrogen recoil intensity at 45° intervals in ϕ.

6.5. Concluding Remarks and Outlook

There are several avenues of further study not covered by the work in this project that could be used to address how surfaces respond to high pressure hydrogen:

- MD simulations of the surface diffusion on AlCu system. These will simulations will validate our models against the experiments described here. (Note that the comparison will focus on activation energy barrier, mechanisms, and trends, not directly on the coverage due to differences in the experimental and simulation timescales.)
- Expand the range of alloy species considered in both experiments and simulations, with emphasis on the constituents of AA2219.
- Determine how hydrogen interacts with oxygen-covered surfaces using temperature programmed desorption (TPD), scanning probes, and LEIS. The combination of these aforementioned techniques can provide unique insight into coverage and adsorption energies needed to model realistic surface conditions.
- Benchmark the above experimental results with tritium experiments (e.g. permeation, tritium imaging plate profiling.) Identify any anomalous results in comparison with D only tests.

7. HYDROGEN ISOTOPE TRAPPING IN AL-CU BINARY ALLOYS

7.1. Introduction

The work that follows will be submitted for inclusion in a peer reviewed journal.

Current materials used for hydrogen storage such as steels are prone to hydrogen embrittlement, in part due to hydrogen trapping at defects. This embrittlement causes concerns over structural integrity and safety. While austenitic stainless steels (SS) are less prone to these issues than high-strength ferritic steels, embrittlement is still a concern at higher pressures and temperatures [101]. As interest in hydrogen as an alternative fuel source rises, there is a search for other materials for hydrogen transport and storage. Aluminum alloys are strong candidate materials for many structural applications due to their low density ($2.7\ \mathrm{g \cdot cm^{-3}}$ vs. $7.8\ \mathrm{g \cdot cm^{-3}}$ for SS) and reasonable yield strength (~290 MPa for AA 2219/T6 vs. ~230 MPa for annealed 304). They are particularly attractive to hydrogen environments because of their extremely low solubility for hydrogen (5.6×10^{-6} mol $\mathrm{H_2 \cdot m^{-3} \cdot MPa^{-0.5}}$ [102,103] vs. 17 mol $\mathrm{H_2 \cdot m^{-3} \cdot MPa^{-0.5}}$ for SS [101,102] at ambient temperature) and hence their relative immunity to embrittlement in dry hydrogen environments [104–107]. However, microstructural defects in Al may trap hydrogen, changing the effective retention and diffusivity of hydrogen in Al alloys significantly [15,103,104,108–120].

Young and Scully [15] conducted a comprehensive study of hydrogen in pure Al. Using thermal desorption spectroscopy (TDS) on as received, cold worked, and annealed Al wire, they derived the binding energies of hydrogen to vacancy ($27.3\ \mathrm{kJ \cdot mol^{-1}}$) and dislocation ($68.6\ \mathrm{kJ \cdot mol^{-1}}$) traps. These deep and plentiful traps are responsible for discrepancies in the apparent diffusivity of and solubility for hydrogen in Al reported in the literature. The concentration of trapped hydrogen often exceeds the concentration of soluble hydrogen [103,108].

The precipitates and solid solution of Al alloys may act as additional trap sites. In the 2xxx series of alloys and in the Al-Cu binary alloys considered here, age hardening forms Al-Cu intermetallic precipitates that strengthen the material. Previous works investigating Al-Cu precipitates has determined the temporal evolution of the precipitates phases:

$$\alpha \rightarrow \mathrm{GP1} \rightarrow \mathrm{GP2}/\Theta'' \rightarrow \Theta' \rightarrow \Theta$$

Increasing Cu content leads to an increase in the amount of hydrogen retained in solid Al-Cu alloys [121]. Internal friction experiments have placed an upper bound for a binding energy to Cu in solution to 0.05 eV [122]. Tritium autoradiography experiments have shown that in Al-Cu (unlike Al-Si alloys), all of the metastable and stable precipitate phases may trap hydrogen [116].

Detailed analysis of trapping energies is often complicated by multiple phases with similar trapping energies, and because the temperatures accessed during charging and TDS often cause the coarsening and/or dissolution of precipitates. The microstructural features responsible for trap sites are inferred from relative energies and occupancies and this is more difficult as the number of trap sites increases. Further, typical analysis of TDS presumes a first order desorption process, a condition that may not be met if binding energies are larger than the energies required to cause coarsening or dissolution [16,17]. Other alloys, such as steels, share these challenges and researchers have relied on differential scanning calorimetry (DSC) and X-ray diffraction to further support their inferences [123]. Hydrogen trapping energies for various phases in Al-Li-Cu-Zr have been determined, but the team that performed the study did not observe significant trapping in binary Al-Cu alloys [17]. Nonetheless, traps have been attributed to not only Mg_2Si (β), but also Al_2Cu (θ) phases in AA 2024/T4 (Al-4.35 Cu-1.5 Mg (compositions in wt.%; Mn composition not specified, but presumably 0.5-0.6)) [109]. Subsequent studies of AA 2024/T351 attributed the higher energy trap observed there instead to Mg-containing S-phase (Al_2CuMg) [112]. Neither work determined the binding energy or occupancy of the trap, though.

Due to the discrepancies in trapping measurements to Al-Cu precipitates in the literature, this work uses high pressure (140 MPa) deuterium (D_2) charging at elevated temperatures (200-300 °C), variable ramp rate TDS, electrical conductivity, and DSC to study the binding energy and typical occupancy of these precipitate traps.

7.2. Experimental

7.2.1. Materials and Deuterium Charging

Table 7. Compositions of Al-Cu alloys studied

Alloy Name	Cu [at.%]	Si [at.%] x 10^{-4}	Fe [at.%] x 10^{-4}	Zn [at.%] x 10^{-4}
Al-0.0 Cu	0.00068	23.	20.	2.0
Al-0.1 Cu	0.0816	29.	13.	19.
Al-0.2 Cu	0.209	42.	14.	25.
Al-0.4 Cu	0.414	48.	15.	37.
Al-0.8 Cu	0.837	31.	16.	17.
Al-1.3 Cu	1.28	37.	17.	19.
Al-1.7 Cu	1.70	39.	17.	25.
Al-2.6 Cu	2.61	50.	17.	5.1
Al-3.4 Cu	3.44	54.	17.	64

Nine different Al-X Cu (0.00 at. % < X ≤ 3.44 at.%) castings were cut into ca. 2 cm x 2 cm x 1.34 mm strips. The greatest impurities were determined to be Si, Fe, and Zn; all are less than 7 x10^{-3} at. %. Compositions are given in Table 6. Deuterium was charged into the sample at in a 130 MPa D_2 for either 68 days at 200 °C or 30 days at 300°C. The expected bulk concentration (mol D/mol Al) in pure Al would be 4.45×10^{-7} and 2.59×10^{-6} for these TABLE 1. respective methods [102,103]. Upon the completion of the charging, the furnace is air cooled to ambient temperature and the samples are immediately placed in a freezer of -54 °C where D_2 diffusion in the sample is very slow (1.7×10^{-12} m^2/s [15,102]). Deuterium is an isotope of hydrogen with a single neutron; it was chosen for this study because it is not naturally abundant in the earth (only 0.0115% of natural hydrogen is deuterium) and environmental deuterium in the vacuum system is well below the detection limit of the residual gas analyzers used in this experiment. Deuterium is a good model for hydrogen interaction in the material, having the same solubility and trapping and diffusivity, D, that is known to scale as $D_D = D_H\sqrt{\frac{m_H}{m_D}}$, where m is the mass of the respective isotope and the subscripts D and H refer to deuterium and hydrogen, respectively.

7.2.2. Electrical Conductivity

The electrical conductivity (σ) measurements were taken at ambient temperature with an SigmaCheck Eddy Current conductivity meter manufactured by ETHER NDE. Four separate measurement frequencies (60, 120, 240 and 480 Hz) were used on every specimen and the meter was calibrated independently at each measurement frequency using pure Al and pure Cu. Changing the frequency changes the depth of the measurement and is done to ensure the through-thickness homogeneity. Uncharged specimens with less than 1.3 at.% Cu were solutionized at 550 °C for 72 hrs to establish the dependence of electrical conductivity on the Cu in solution. The maximum solid solubility for Cu in Al is 2.4 at.% [124], so these samples are assumed to be fully solutionized.

Electrical resistivity, ρ, is the inverse of electrical conductivity, $\rho=1/\sigma$, and increases proportionally to solute content, C. As precipitates nucleate and grow, C decreases, decreasing ρ and increasing σ. Charged specimens were measured to determine these electrical conductivity changes due to precipitate evolution during charging and/or the D present in the materials. Finally, samples were tested after various segments of thermal ramps to determine the solute/precipitate temporal evolution.

7.2.3. Differential Scanning Calorimetry

In this study, a STA 449 F3 Jupiter manufactured by Netzsch was used for DSC measurements. By calibrating with both an inert reference (empty crucible) and a sapphire sample of known heat capacity, the data for the heat capacity of Al-Cu samples of interest are also obtained. In this study, uncharged Al-Cu samples were used to identify the temperature range where the precipitates dissolve.

7.2.4. Thermal Desorption Spectroscopy

The mass and electrical conductivity of the samples were measured before and after the thermal desorption spectroscopy (TDS) experiments at room temperature. A scale accurate on the order of micrograms manufactured by Mettler Toledo measured the masses of the samples. On average, the total transfer time between removing the sample from the freezer to starting the TDS system was 15 min.

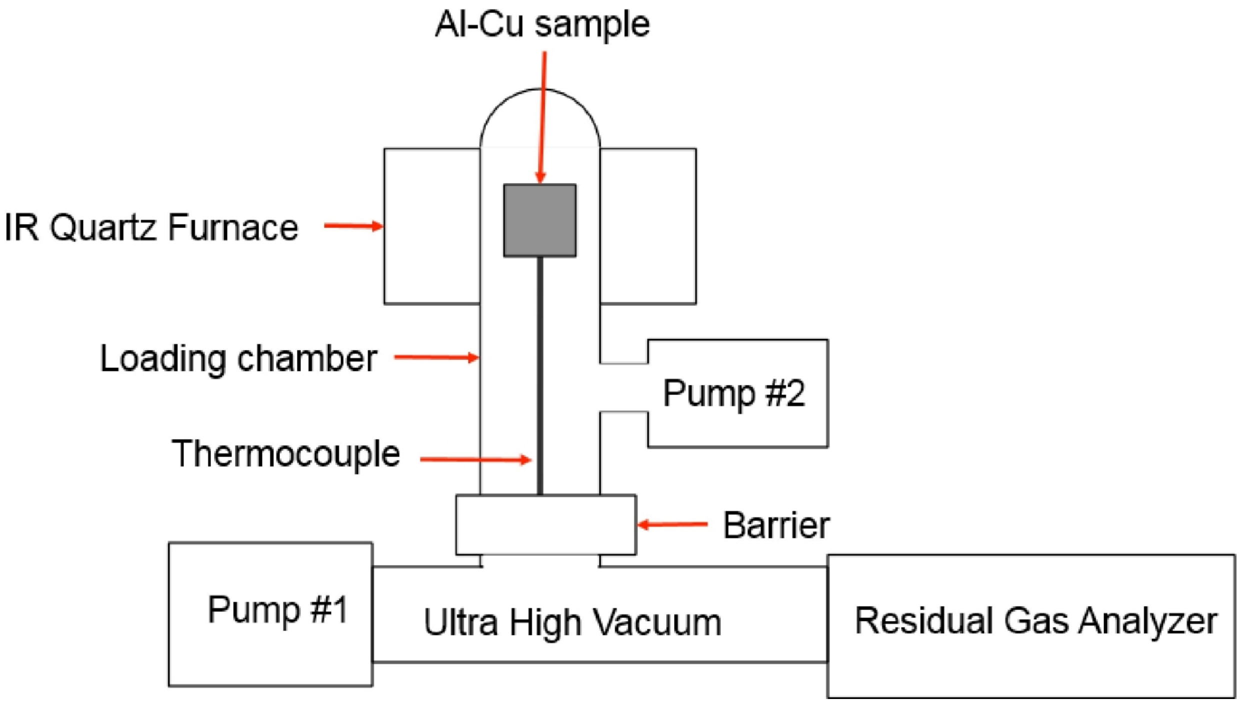

Figure 35. Schematic of the TDS system used. There were two separate chambers: loading chamber and Ultra High Vacuum Chamber. The heating element was an infrared quartz furnace with a thermocouple to measure the temperature.

The system used in these experiments is shown schematically in Figure 34. Constant heating rate tests from 0.5°C/min to 5°C/min were performed. To start, a sample was placed in the loading chamber in the quartz furnace at room temperature. After sealing the system, the chamber was then pumped down to around 12 mtorr before the barrier between the ultra high vacuum chamber (1×10^{-8} torr) was opened. The experiment began when the chamber achieved a pressure of 1×10^{-6} torr. A residual gas analyzer (RGA) was used to monitor the partial pressure of D (from both mass 3 (HD) and mass 4 (D_2)) outgassing from the sample. The signal from these peaks was large enough that the Faraday cup was able to detect these without the use of a channel electron multiplier. The furnace temperature was measured by a thermocouple in the quartz thimble that the tantalum sample holder was attached onto. These Al-Cu samples were heated to just below their melting point (550 °C).

In addition to the ramped TDS experiments, interrupted TDS experiments were also conducted. The furnace was programmed to bring the temperature of the sample to the intended start temperature held isothermally for 5 min to insure temperature stabilization then is heated at a predetermined constant rate to the incremented stop temperature and also held isothermally before cooling to room temperature. The temperature increment was 100°C – so for these samples, the TDS was interrupted 3 times (at 200°C, 300°C, and 400°C). In between each of these increments, the mass and electrical conductivity of the sample were measured.

A multi-peak Polanyi-Wigner fit implemented in GNU Octave [125] to the TDS data determines trapping peaks. When the sample is subject to an increasing temperature ramp, it will desorb D from the trap with the lowest to highest binding energy. If all conditions are maintained and the heating rate is adjusted, the peaks will shift; this shift can be plotted on a Kissinger plot to determine the binding energy [126].

7.3. Results

7.3.1. Electrical Conductivity

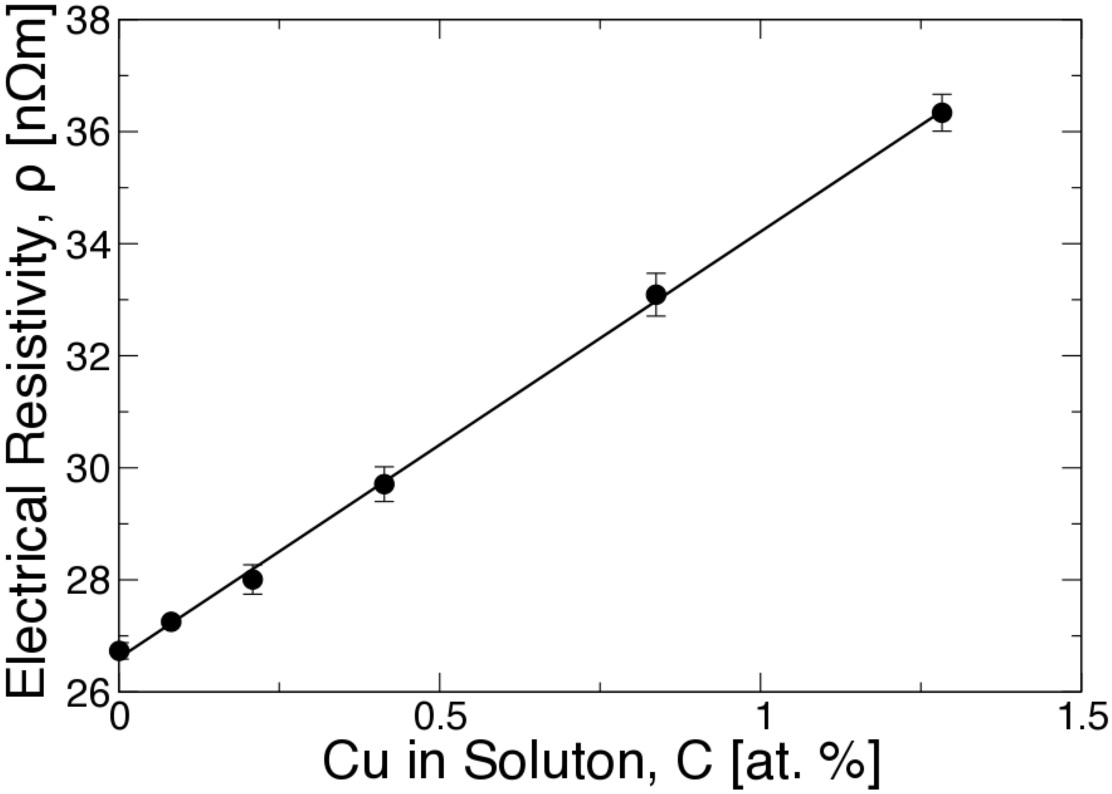

Figure 36. Electrical conductivity of solutionized Al-Cu samples. This linear relationship between the electrical and conductivity allows for the determination of the amount of Cu in solution vs. the amount in precipitates from measured conductivity.

Figure 35 shows the electrical resistivity of solutionized samples ($C<$ at.% Cu). A linear fit to this data shows that:

$$\rho = (7.6 \pm 0.1) \text{ x } C + (26.60 \pm 0.08), \tag{7}$$

where ρ is given in nΩm and C is given in at.% Cu. The intercept of 26.60 ±0.08 nΩm is equivalent to an electrical conductivity of 37.6±0.1 and is in good agreement with the values reported for pure Al at ambient temperature (36.6-37.7 MS/m [124,127,128]). The slope of (7.6 ±0.1) nΩm/at. % Cu is also comparable to literature values.

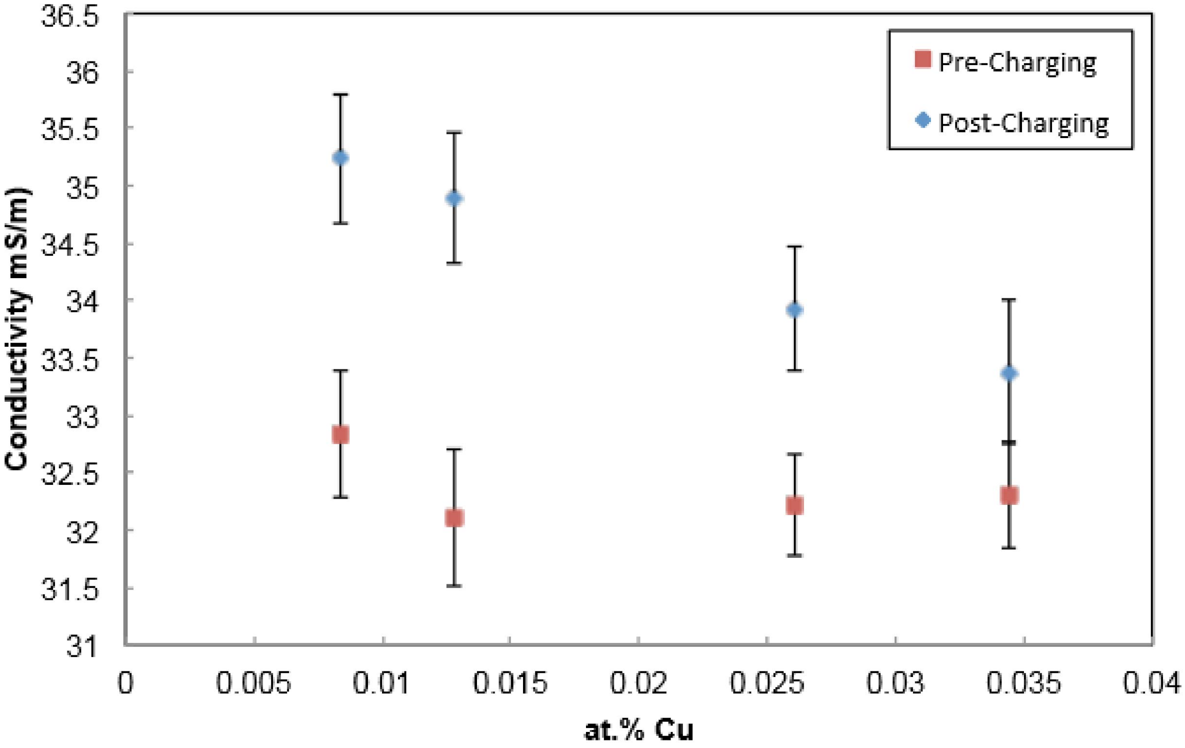

Figure 37. A plot showing the conductivity change of Al-Cu witness samples with varying amount of Cu after undergoing the 300ºC, 30 days and 200ºC, 68 days charging conditions but were never in the presence of deuterium. The increase in conductivity due to charging indicates that there was precipitate growth and coarsening under the charging conditions imposed. There is more Cu in precipitates in samples that were charged for a longer period of time.

Electrical conductivity is also used to track the temporal evolution of the material during charging runs.

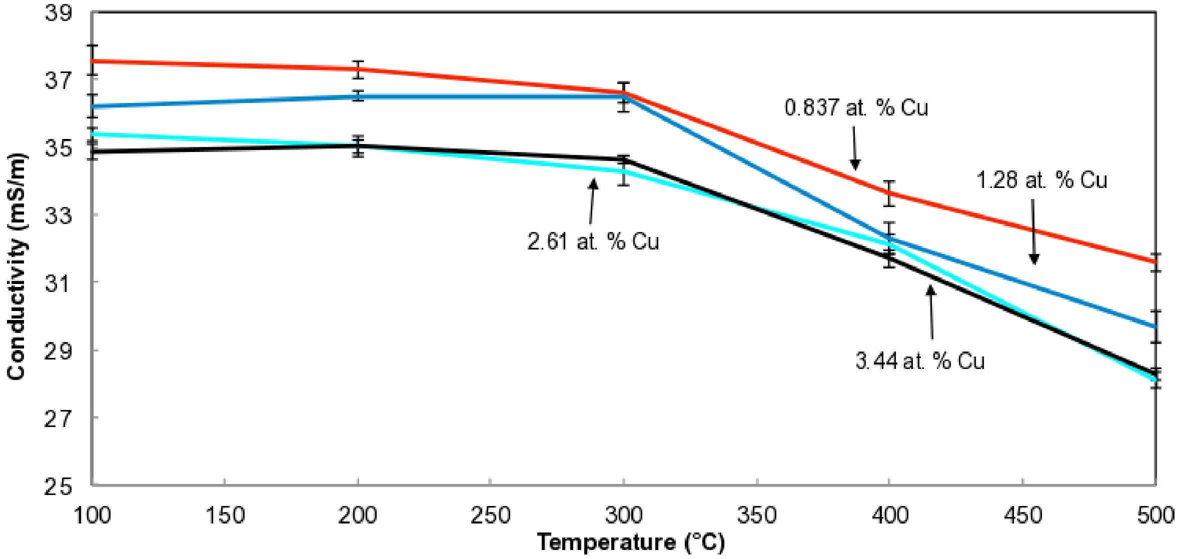

Figure 38. A plot showing the conductivity change for varying samples charged at 200ºC for 68 days during an interrupted TDS experiment. There is a decrease in conductity from 300ºC to 500ºC due to the dissolution of precipitates.

The incremented TDS experiments (Figure 37) show little decrease in electrical conductivity between ambient temperature and 300°C, but show a more substantial decrease between 300°C and 500°C. This is due to the dissolution of precipitates, which results in the increase of Cu in solution.

7.3.2. Differential Scanning Calorimetry

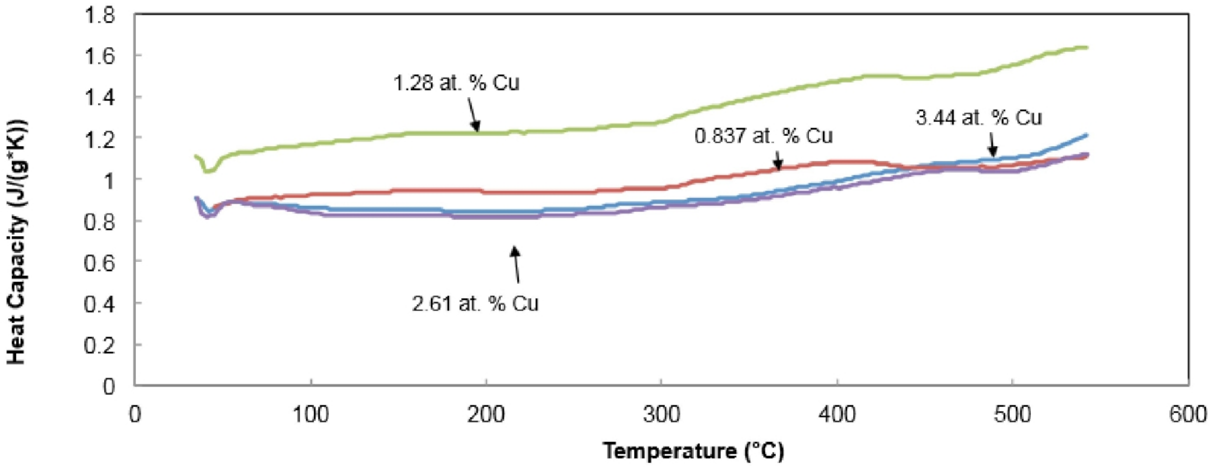

Figure 39. Heat capacity of Al-X Cu (0.837 at. % < X < 3.44 at. %). There is an increase in heat capacity 300°C to 500°C because of the dissolution of precipitates.

Using DSC, the evolution of the precipitates can be observed. The heat capacity results (Figure 37) show relatively no microstructural changes until 300°C when the Cu precipitates begin to dissolve because the exothermic precipitate dissolution increases the heat capacity. The initial dip at 50°C can be accounted to the instrument error as it begins the heating process.

7.3.3. Thermal Desorption Spectroscopy

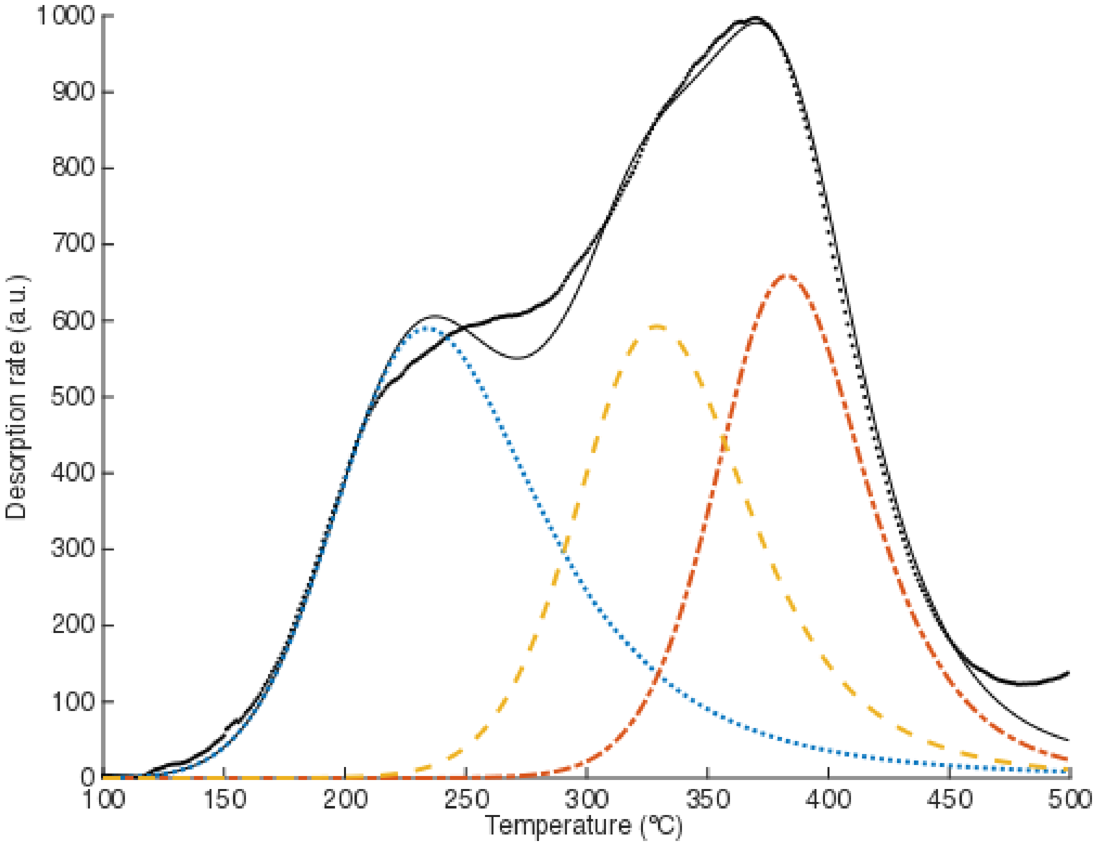

Figure 40. Example of Polanyi-Wigner peak fit of desorption spectra from sample with 3.44 at. % Cu tested at 5°C/min. Each peak indicates a trap site and integrating each peak can give the amount of deuterium in each trap site.

Table 8. Peak positions and amount of D2 desorbed from sample of 2.61 at % Cu charged at 200ºC for 68 days desorbed at a rate of 5ºC/min

Trap Site*	Peak Position (°C)	Concentration of D (mols D/mols Al)
Lattice	234	$3.80\text{x}10^{-7}$
Precipitates	329	$3.15\text{x}10^{-7}$
Dislocations	383	$3.00\text{x}10^{-7}$
Total	--	$9.95\text{x}10^{-7}$
Expected D in Lattice [103]	--	$4.61\text{x}10^{-7}$

* Lattice and dislocation traps are inferred from their good agreement with Ref. [15]. The vacancy peak found there occurs above the maximum temperature of our desorption

experiments, which is set to prevent sample melting. The precipitate trap is inferred here because it is unique to this study and the peak area increased with increasing Cu content.

In Figure 38, three distinct trap states are seen from the peak fit's good agreement with the desorption data. The D desorbed from the sample can be roughly estimated by integrating the TDS spectrum and is reported in Table 7. Lattice and dislocation traps are inferred from their good agreement with Ref. [15]. The vacancy peak found there occurs above the maximum temperature of our desorption experiments, which is set to prevent sample melting. The precipitate trap is inferred here because it is unique to this study and the peak area increased with increasing Cu content. The concentration of D_2 desorbed from the α-Al lattice is comparable to the expected D_2 solubility in pure Al [103] and there is almost as much D_2 in each of the two trapping peaks.

7.3.4. Thermally ramped tests

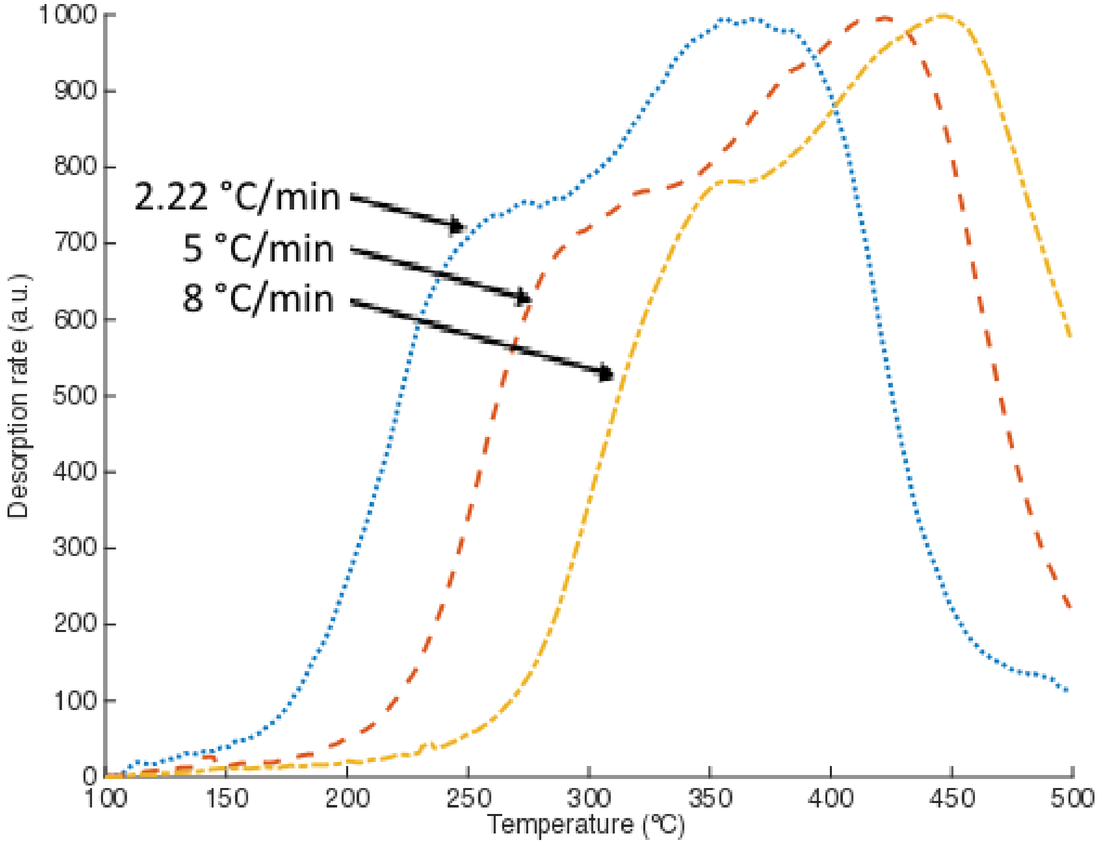

Figure 41. An overlaid desorption spectra of sample of 2.61 at. % Cu at various heating rates. The peaks shifts to a higher temperature range due to increasing heating rate. This peak shift can be used to calculate the binding energy of each trap site.

Using heating rates from 0.5ºC/min to 10 ºC/min, the peak positions from each desorption spectra can be used together to determine the energy of the trap site. As the heating rate increases, the desorption spectra shifts to a higher temperature. As seen from Figure 39, the general shape of spectra does not change. Using the peak fit program to identify the peaks from each experiment with different ramp rates, each peak position individually shifts a different amount and can be plotted on a Kissinger plot to illustrate the peak position change. The resulting data can be used to determine the desorption energy of the trap site by calculating the slope of the best fit line of the peak position.

7.4. Discussion

7.4.1. Al-Cu vs. Pure Al

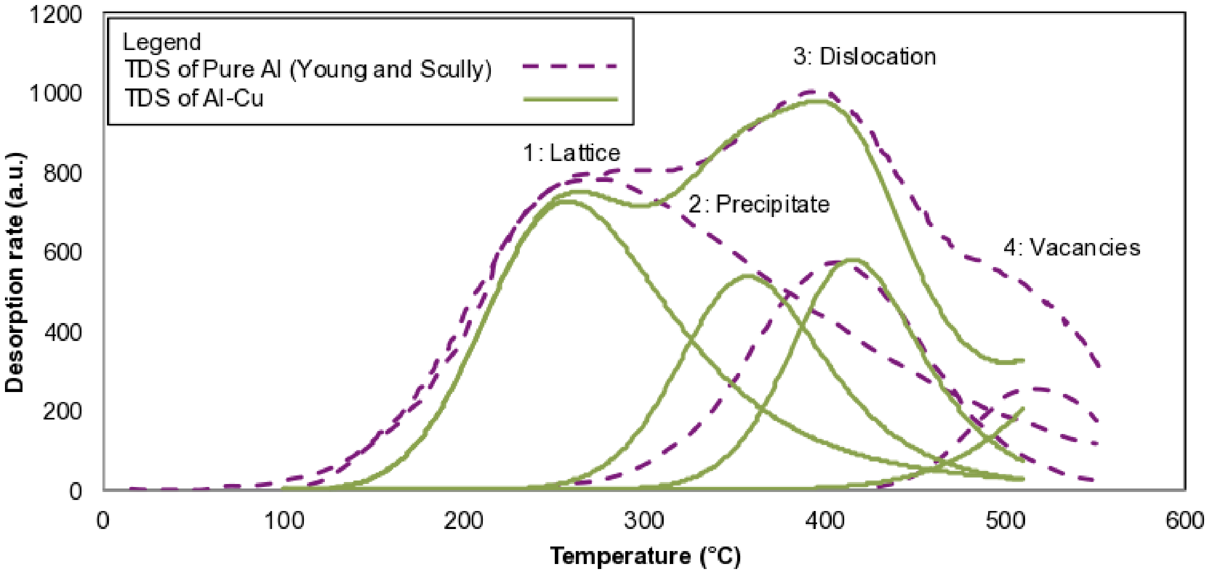

Figure 42. Overlaid desorption spectra of pure Al from Young and Scully [REF] and Al-2.61 at. % Cu at 10°C/min. The peak fits and determined trap locations are also included. Since pure Al has no precipitate microstructure, the appearance of an additional peak in the Al-Cu spectra suggests that it is a precipitate trap site.

Figure 41 displays both the desorption results at 10°C/min from pure Al reported in Ref. [15] and from Al-2.61 at. % Cu of this study with trap states labeled from low temperature to high temperature as #1,2,3,4.. This Al-Cu sample was dry charged at 200°C for 68 days whereas the in Ref. [9] a wet charging method was used. There are three peak positions in good agreement between the two desorption spectra; however, there is an addition peak in the fit for the Al-Cu sample at around 325°C. This peak position appears consistent throughout the ramped TDS data for all runs in this work and the size increases with increasing Cu content, suggesting that there is indeed an additional trap site present in the Al-Cu alloy.

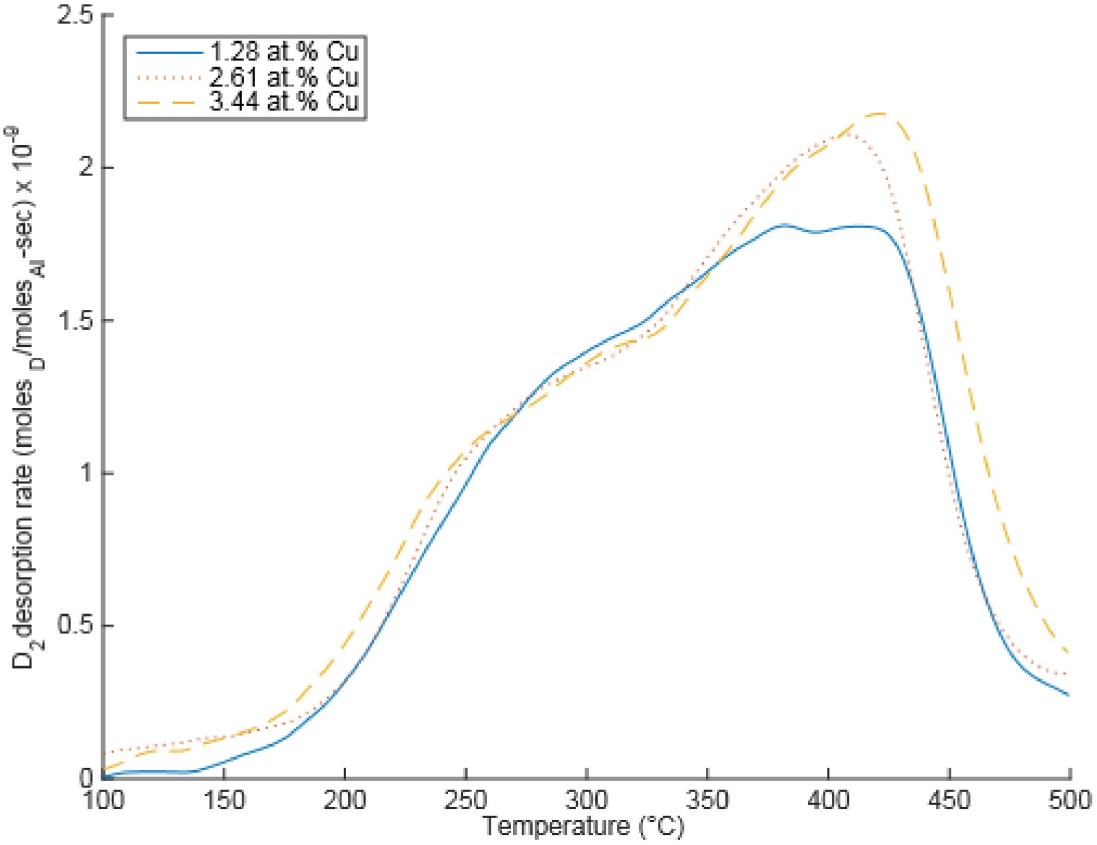

Figure 43. Overlaid desorption spectra of Al-Cu samples of varying Cu content tested at 2.22°C/min.

Observing the overlaid results of the various Al-Cu samples charged at 200ºC for 68 days and desorbed at 0.833ºC/min Figure 42, one can see that the total amount of D_2 increases with Cu content and this increase occurs in the peak we identify as being due to precipitates as well as the dislocation peak. Thermally stable precipitates can increase the dislocation density not only through more misfit dislocations around semi-coherent precipitates, but also by generating them due to the differences in the coefficients for thermal expansion between the α-Al matrix and the precipitates.

7.4.2. Varying Ramp Comparison

When observing the TDS results in isolation, it is impossible to label the trap state of the desorption peak. Only by comparing the data to the pure Al study [103] can the peaks then be labeled. When the peak data is then plotted on the Kissinger plot, the peaks can be labeled to a trap state when comparing to the existing Al data. Some odd observations when varying the ramp rates was in ability to observe the lattice peak at ramp rates slower than 0.83ºC/min. This may be caused by the sample processing when desorbing. Exposure to the environment for extended duration of time before placing into the TDS may have resulted in the diffusion and desorption of D from the lattice.

7.4.3. Charging conditions

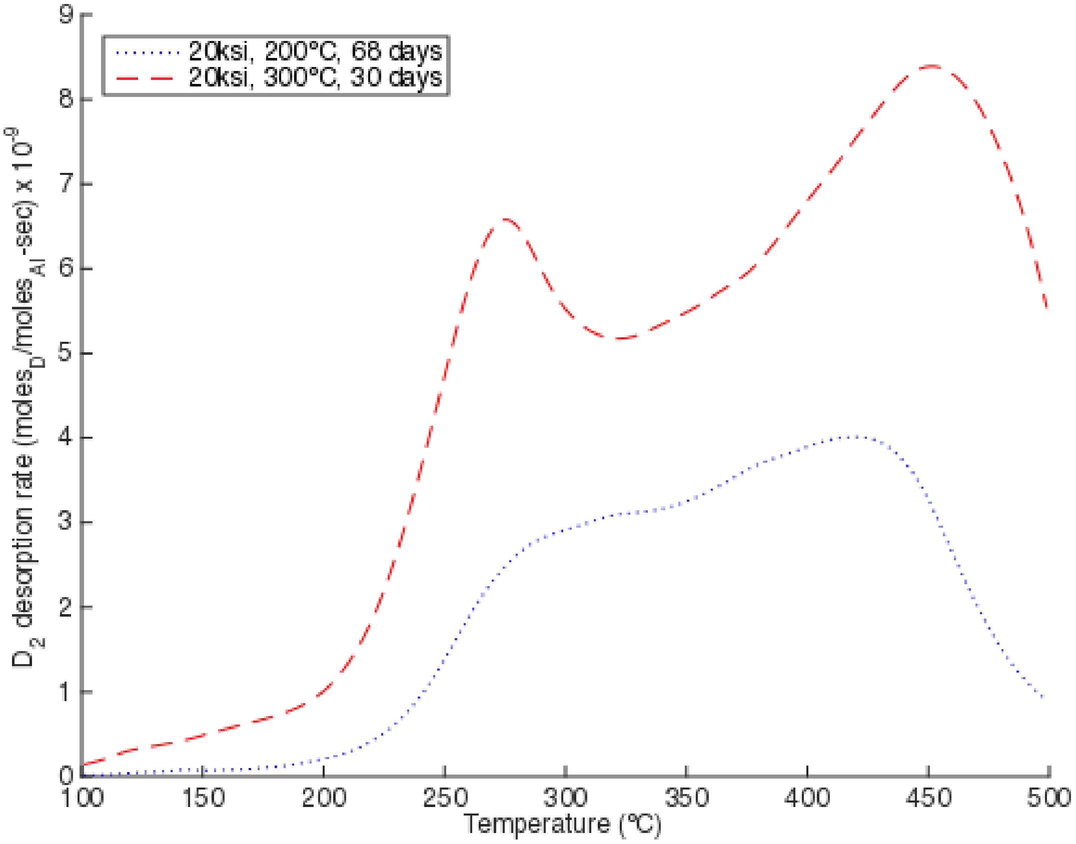

Figure 44. Overlaid desorption spectra tested at 5°C/min of a sample with 2.61 at. % Cu charged at 200°C and 300°C. There was more deuterium in the sample charged at 300°C and the peaks in both desorption spectras are comparable.

The charging conditions of the samples do not greatly alter the peak position of the traps. Instead, it affects the amount of D trapped. As seen in Figure 43 the higher temperature charging conditions resulted in more D trapped as noted by the larger area under the curve. As seen from Figure 35, the conductivity of the sample increased after the charging at 300°C suggesting that Cu left the solution (α) and coarsened the precipitates. Because no missing peak was observed, the precipitate is likely to be the θ'' or θ'. A more accurate guess can be made based on the aging time. There could have also been a temporal evolution during this charging so the type of precipitate is also unknown.

7.4.4. Comparison of thermally ramped tests

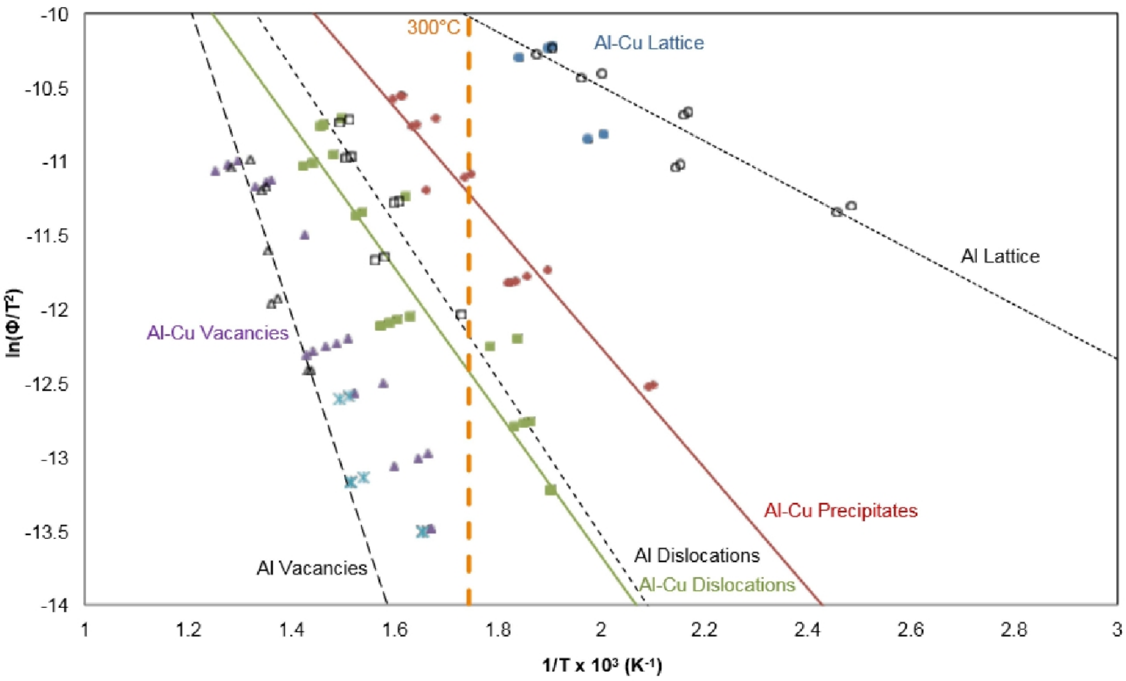

Figure 45. Kissinger plot of the Al and Al-Cu desorption peaks for different ramp rates including a 300°C guideline to indicate the approximate precipitate dissolution temperature. The precipitate trapping peak is independently correlated cross all different desorption experiments of differing heating rates and has a binding energy of 18.4 kJ/mol (0.19 eV).

Table 9. Summary of trapping data determined from TDS.

Desorption Peak	**Trap Site**	**Pure Al Desorption Energy, E_d (kJ/mol)** [15]	**Al-Cu Desorption Energy, E_d (kJ/mol) [This work]**
1	Lattice	15.3 ± 4.8	--*
2	Precipitates	--	33.8 ± 2.5
3	Dislocations	43.5 ± 17.5	40.5 ± 6.0
4	Vacancies	84.8 ± 32.2	--**

[*] The lattice desorption energy calculated here is 36±12 kJ/mol, but the high uncertainty is because it is convoluted with the Cu solute peak.

[**] While some ramp rates in this work had an observable trap close to that found in Ref. [15], most ramp rates there would occur above the maximum temperature of our desorption experiments (Figure 43), so we do not calculate the trapping energy for vacancies in this work.

The binding energy and amount of trapped D can be determined by following the equation that correlates the peak shift due to the varying ramp rates. When comparing the peak positions from the TDS spectrum of the Al-Cu and Al (Obtained from Young and Scully) there is good agreement between the peak positions of defect trapping locations: dislocation and vacancies. It is unknown why there is some cases when the lattice peak does not clearly appear on the desorption spectra. The slower ramp rates produced another peak in the vacancy region that was unresolved; that additional peak in that region was not independently correlated with runs of other ramp rates. However, there is independent correlation among the hypothesized Al-Cu precipitates trapping state that does not lie on the peak data from pure Al [103]. Because the only difference between Al and Al-Cu in terms of trapping locations is the additional intermetallic precipitates whose interface introduce strain energy that can be a trap for hydrogen isotopes. Work done with tritium electron microautoradiograpy has observed the GP zones in Al-4 mass % Cu alloy act as trapping sites for hydrogen[116].

$$\frac{d\ln\left(\Phi / T_{\max}^{2}\right)}{d\left(1 / T_{\max}\right)} = \frac{E_d}{R} \tag{8}$$

7.5. Conclusion

By using the Thermal Desorption Spectroscopy to desorb deuterium from Al-Cu samples and then comparing the results with literature on the TDS results of pure Al, there is an observed precipitate trapping peak with a binding energy of of 18 ± 3 kJ·mol^{-1} (0.19 ± 0.03 eV). Due to the effecting aging conditions of the alloy, it is likely that the θ’ phase is responsible for this trap. Because this is a common phase in peak-aged materials, precipitation-strengthened Al-Cu alloys such as those in the 2xxx series will likely retain more H than pure Al. Use of electrical conductivity as a tool to determine the amount of Cu in solution and precipitate phase in the sample.

8. CONCLUSIONS

The main goal of this project was to establish an understanding of the interaction between H an AlCu alloys, primarily at the surface and near bulk defects. The work was framed around a hierarchical multiscale-modeling framework incorporating DFT, a bond-order interatomic potential and discrete dislocation dynamics. Experiments validated several aspects of the modeling for H interactions of bulk and surface defects. Significant advances were made in all phases of this project elucidating the interactions of H and the metals, as well as the development of new modeling tools for future work.

A high fidelity bond-order interatomic potential was developed for the Al-Cu-H ternary system. In order to parameterize the potential, a substantial DFT library of cohesive energies, geometric parameters, and defect energies, was calculated. The DFT library established a point of reference for the fitting process for the BOP. In addition to the using the DFT to fit the BOP, rigorous MD simulations of vapor depositions confirmed the potentials ability to correctly reproduce the low energy structures. This is the first potential ever capable of predicting the Al rich side of the Al-Cu phase diagram. Also, the potential captures the very difficult chemistry involved in the dissociation of molecular H_2 into atomic H. A number of annealing and deposition simulations further confirm the correct physics for the H-metal potentials.

Employing the BOP allowed for the examination of a range of properties and situations critical for the understanding of the Al-Cu alloys. First the characteristics of dislocations for pure Al were thoroughly examined. A technique was employed for determining dislocation core energy and radius that is purely atomistic. Interestingly, the simulations revealed that the accepted definition of core energy as a function of character is potentially incomplete. While the general trend of the core energy is maintained, the core energy does not monotonically increase with character angle. A few special character angles have lower energies due to symmetry relative to other lower character angle dislocation cores. A simple model was developed to describe this behavior; however, further analysis is required to completely understand this phenomenon.

In addition to the dislocation core properties, a number of other dislocation properties were determined for input into dislocation dynamics models. MD simulations determined misfist strains necessary for the parameterization of DD simulations, these strains were shown to be independent of the simulation cell size and with large enough sizes converged to a per atom value. Along with the misfit strain, equilibrium configurations of pure edge dislocations and GP-I zones were determined. These showed that there is an attractive and repulsive side to the precipitate depending on orientation. When attracted to the precipitate, the dislocation impinges on the precipitate and sticks to the system. Also, the cutting stresses, as a function of precipitate density, into the repulsive side of the precipitate was determined. This work shows that, the cutting stress goes up with increasing precipitate density. These properties are then first used to fit the potentials and also used as a point of validation for the models.

Significant advances were made in the field of DD modeling. Beginning with the ParaDis code, contributions to the code included, new precipitate shapes beyond spherical inclusions, to general ellipsoids. Also, a new detection algorithm was implemented for greater resolution of intersection of dislocations and precipitates. Using these new advances and incorporating the information garnered from the MD simulations results in near identical representation of the MD simulations.

Using low energy ion scattering techniques a number of important discoveries were made. First, there is only a modest change in H uptake on Al-Cu polycrystalline surfaces in comparison with (100) pure Al surfaces. The experiments here are performed with 20 wt.% Cu, which is significantly higher than the 6 wt.% for the alloy of interest, AA2219. This suggests that the introduction of Cu does not act as a significant catalyst for the dissociation of molecular H. In addition to surface uptake, the binding configuration was determined. In contrast to previous studies and our MD and DFT simulations, these experiments determine the hollow site on the (100) surface as the preferred adatom location. This difference is not understood. Further analysis is required to determine this discrepancy.

In conjunction with the surface analysis of LEIS, bulk analysis of H trapping was performed with TDS. Comparing the spectrum of D charged Al-Cu alloys to pure Al samples (and reinforce by literature results) reveals a distinct peak associated with the presence of Cu. The binding energy for this peak was determined to be 0.19 eV. This value is significantly lower than the values calculated using MD simulations (~2eV) for GP-I precipitates. This discrepancy has yet to be. Additionally, these experiments showed that Cu-containing alloys will retain substantially more H than pure Al.

While a number of advances were made in the understanding of H interactions with Al-Cu alloys, a significant amount of work remains to be completed to fully understand how H may interact with materials such as AA2219. The foundation has been established for significant insight in the near future.

9. REFERENCES

1. R.A. Oriani, Hydrogen Embrittlement of Steels, in: *Annu. Rev. Mater. Sci.*, Vol.8, pp. 327–357, 1978.
2. L. Christodoulou and H.M. Flower, Hydrogen embrittlement and trapping in Al-6%-Zn-3%-Mg, in: *Acta Metall.*, Vol.28, pp. 481–487, 1980.
3. J. Albrecht, I.M. Bernstein, and A.W. Thompson, Evidence for Dislocation Transport of Hydrogen in Aluminum, in: *Metall. Trans. A*, Vol.13, pp. 811–820, 1982.
4. J.E. Angelo, N.R. Moody, and M.I. Baskes, Trapping of hydrogen to lattice defects in nickel, in: *Model. Simul. Mater. Sci. Eng.*, Vol.3, pp. 289–307, 1995.
5. W.-S. Ko, J.-H. Shim, and B.-J. Lee, Atomistic modeling of the Al–H and Ni–H systems, in: *J. Mater. Res.*, Vol.26, pp. 1552–1560, 2011.
6. F. Apostol, Angular-dependent interatomic potential for the aluminum-hydrogen system, in: *Phys. Rev. B*, Vol.82, p. 054116, 2010.
7. D.G. Pettifor and I.I. Oleinik, Analytic bond-order potentials beyond Tersoff-Brenner. I. Theory, in: *Phys. Rev. B*, Vol.59, pp. 8487–8499, 1999.
6. D.G. Pettifor and I.I. Oleinik, Bounded Analytic Bond-Order Potentials for σ and π Bonds
9. D.G. Pettifor and I.I. Oleinik, Analytic bond-order potential for open and close-packed phases, in: *Phys. Rev. B*, Vol.65, p. 172103, 2002.
10. D.A. Murdick, Analytic bond-order potential for the gallium arsenide system, in: *Phys. Rev. B*, Vol.73, 2006.
11. D.K. Ward, Analytical bond-order potential for the cadmium telluride binary system, in: *Phys. Rev. B*, Vol.85, p. 115206, 2012.
12. A. Arsenlis, W. Cai, M. Tang, M. Rhee, T. Oppelstrup, G. Hommes, et al., Enabling strain hardening simulations with dislocation dynamics, in: *Model. Simul. Mater. Sci. Eng.*, Vol.15, pp. 553–595, 2007.
13. R.D. Kolasinski, J.A. Whaley, and R. Bastasz, Real-space ion scattering maps of the Mg(0001) surface, in: *Phys. Rev. B*, Vol.79, p. 075416, 2009.
14. R.D. Kolasinski, N.C. Bartelt, J.A. Whaley, and T.E. Felter, Channeling of low-energy ions on hydrogen-covered single-crystal surfaces, in: *Phys. Rev. B*, Vol.85, p. 115422, 2012.
15. G.A. Young and J.R. Scully, The diffusion and trapping of hydrogen in high purity aluminum, in: *Acta Mater.*, Vol.46, pp. 6337–6349, 1998.
16. J.R. Scully, G.A. Young, and S.W. Smith, Hydrogen solubility, diffusion and trapping in high purity aluminum and selected Al-base alloys, in: *Mater. Sci. Forum*, Vol.331-337, pp. 1583–1599, 2000.
17. S. Smith and J. Scully, The identification of hydrogen trapping states in an Al-Li-Cu-Zr alloy using thermal desorption spectroscopy, in: *Metall. Mater. Trans. A*, Vol.31, pp. 179–193, 2000.
18. M.E. Krug and D.C. Dunand, Modeling the creep threshold stress due to climb of a dislocation in the stress field of a misfitting precipitate, in: *Acta Mater.*, Vol.59, pp. 5125–5134, 2011.
19. X.W. Zhou, D.K. Ward, M. Foster, and J.A. Zimmerman, An analytical bond-order potential for the copper–hydrogen binary system, in: *J. Mater. Sci.*, Vol.50, pp. 2859–2875, 2015.
20. X.W. Zhou, D.K. Ward, and M. Foster, An analytical bond-order potential for the aluminum copper binary system, in: *Submitted*

21. X.W. Zhou, D.K. Ward, and M. Foster, A bond-order potential for the Al-Cu-H ternary system, in: *Prep.*
22. J.P. Hirth and J. Lothe, *Theory of dislocations*.Krieger Pub. Co., Malabar, FL, 1992.
23. P.R. Subramanian, D.J. Chakrabarti, and D.E. Laughlin, *Phase diagrams of binary copper alloys*.ASM International, Materials Park, OH, 1994.
24. J.L. Murray, The aluminium-copper system, in: *Int. Met. Rev.*, Vol.30, pp. 211–234, 1985.
25. C. Qiu, G.B. Olson, S.M. Opalka, and D.L. Anton, Thermodynamic evaluation of the Al-H system, in: *J. Phase Equilibria Diffus.*, Vol.25, pp. 520–527, 2004.
26. T.B. Massalski, H. Okamoto, and ASM International, eds., *Binary alloy phase diagrams*.2nd ed.ASM International, Materials Park, Ohio, 1990.
27. A.F. Voter and S.P. Chen, Accurate Interatomic Potentials for Ni, Al and Ni3Al, in: *MRS Proc.*, Vol.82, 1986.
28. X.W. Zhou, H.N.G. Wadley, R.A. Johnson, D.J. Larson, N. Tabat, A. Cerezo, et al., Atomic scale structure of sputtered metal multilayers, in: *Acta Mater.*, Vol.49, pp. 4005–4015, 2001.
29. X.W. Zhou, Misfit-energy-increasing dislocations in vapor-deposited CoFe/NiFe multilayers, in: *Phys. Rev. B*, Vol.69, p. 144113, 2004.
30. M.I. Baskes, J.E. Angelo, and N.R. Moody, Atomistic Calculations of Hydrogen Interactions with Ni $_3$ Al Grain Boundaries and Ni/Ni $_3$ Al Interfaces, in: A.W. Thompson, N.R. Moody (Eds.), *Hydrog. Eff. Mater.*, John Wiley & Sons, Inc., Hoboken, NJ, USA, 2013: pp. 77–90.
31. J. Cai, Simple analytical embedded-atom-potential model including a long-range force for fcc metals and their alloys, in: *Phys. Rev. B*, Vol.54, pp. 8398–8410, 1996.
32. M.I. Mendelev, D.J. Srolovitz, G.J. Ackland, and S. Han, Effect of Fe Segregation on the Migration of a Non-Symmetric Σ5 Tilt Grain Boundary in Al, in: *J. Mater. Res.*, Vol.20, pp. 208–218, 2005.
33. K.W. Jacobsen, Interatomic interactions in the effective-medium theory, in: *Phys. Rev. B*, Vol.35, pp. 7423–7442, 1987.
34. S.M. Foiles, Calculation of the surface segregation of Ni-Cu alloys with the use of the embedded-atom method, in: *Phys. Rev. B*, Vol.32, pp. 7685–7693, 1985.
35. S.M. Foiles, Embedded-atom-method functions for the fcc metals Cu, Ag, Au, Ni, Pd, Pt, and their alloys, in: *Phys. Rev. B*, Vol.33, pp. 7983–7991, 1986.
36. J.B. Adams, S.M. Foiles, and W.G. Wolfer, Self-diffusion and impurity diffusion of fee metals using the five-frequency model and the Embedded Atom Method, in: *J. Mater. Res.*, Vol.4, pp. 102–112, 1989.
37. M.I. Mendelev, M.J. Kramer, C.A. Becker, and M. Asta, Analysis of semi-empirical interatomic potentials appropriate for simulation of crystalline and liquid Al and Cu, in: *Philos. Mag.*, Vol.88, pp. 1723–1750, 2008.
38. M.I. Mendelev, M.J. Kramer, R.T. Ott, D.J. Sordelet, D. Yagodin, and P. Popel, Development of suitable interatomic potentials for simulation of liquid and amorphous Cu–Zr alloys, in: *Philos. Mag.*, Vol.89, pp. 967–987, 2009.
39. Y. Mishin, Interatomic potentials for monoatomic metals from experimental data and *ab initio* calculations, in: *Phys. Rev. B*, Vol.59, pp. 3393–3407, 1999.
40. F. Apostol, Interatomic potential for the Al-Cu system, in: *Phys. Rev. B*, Vol.83, 2011.

41. Y. Mishin, Structural stability and lattice defects in copper: *Ab initio*, tight-binding, and embedded-atom calculations, in: *Phys. Rev. B*, Vol.63, p. 224106, 2001.
42. B. Jelinek, Modified embedded atom method potential for Al, Si, Mg, Cu, and Fe alloys, in: *Phys. Rev. B*, Vol.85, p. 245102, 2012.
43. L. Liu, A. Jaramillo-Botero, W.A. Goddard, and H. Sun, Development of a ReaxFF Reactive Force Field for Ettringite and Study of its Mechanical Failure Modes from Reactive Dynamics Simulations, in: *J. Phys. Chem. A*, Vol.116, pp. 3918–3925, 2012.
44. J.G.O. Ojwang, R.A. van Santen, G.J. Kramer, A.C.T. van Duin, and W.A.G. Iii, Parametrization of a reactive force field for aluminum hydride, in: *J. Chem. Phys.*, Vol.131, p. 044501, 2009.
45. M.S. Daw, Embedded-atom method: Derivation and application to impurities, surfaces, and other defects in metals, in: *Phys. Rev. B*, Vol.29, pp. 6443–6453, 1984.
46. Y. Shimomura, M.W. Guinan, and T.D. de la Rubia, Atomistics of void formation in irradiated copper, in: *J. Nucl. Mater.*, Vol.205, pp. 374–384, 1993.
47. Q. Sun, J. Xie, and T. Zhang, Chemisorption of hydrogen on stepped (410) surfaces of Ni and Cu, in: *Surf. Sci.*, Vol.338, pp. 11–18, 1995.
48. J. Xie, P. Jiang, and K. Zhang, Dynamics of H2 dissociation on Cu(100): Effects of surface defects, in: *J. Chem. Phys.*, Vol.104, p. 9994, 1996.
49. T. Cheng, A. Jaramillo-Botero, W.A. Goddard, and H. Sun, Adaptive Accelerated ReaxFF Reactive Dynamics with Validation from Simulating Hydrogen Combustion, in: *J. Am. Chem. Soc.*, Vol.136, pp. 9434–9442, 2014.
50. D.G. Pettifor, M.W. Finnis, D. Nguyen-Manh, D.A. Murdick, X.W. Zhou, and H.N.G. Wadley, Analytic bond-order potentials for multicomponent systems, in: *Mater. Sci. Eng. A*, Vol.365, pp. 2–13, 2004.
51. R. Drautz, Analytic bond-order potential for predicting structural trends across the *sp*-valent elements, in: *Phys. Rev. B*, Vol.72, p. 144105, 2005.
52. LAMMPS Molecular Dynamics Simulator, in: http://lammps.sandia.gov
53. S. Plimpton, Fast Parallel Algorithms for Short-Range Molecular Dynamics, in: *J. Comput. Phys.*, Vol.117, pp. 1–19, 1995.
54. I. Barin, *Themochemical Data of Pure Substances*.VCH, Weinheim, 1993.
55. J.D.H. Donnay and H.M. Ondik, Determiniative Tables, erd ed., vol. 2 (inorganic compounds), in: 1973.
56. J.P. Bugeat, A.C. Chami, and E. Ligeon, A study of hydrogen implanted in aluminium, in: *Phys. Lett. A*, Vol.58, pp. 127–130, 1976.
57. H.M. Zbib, Introductino to Discrete Dislocation Dynamics, in: C. Sansour, S. Skatulla (Eds.), *Gen. Contin. Dislocation Theory*, Springer, New York, 2012: pp. 289–317.
58. M. Heggie, R. Jones, and A. Umerski, Interaction of impurities with dislocation cores in silicon, in: *Philos. Mag. A*, Vol.63, pp. 571–584, 1991.
59. R. Jones, A. Umerski, P. Sitch, M.I. Heggie, and S. Öberg, Density functional calculations of the structure and properties of impurities and dislocations in semiconductors, in: *Phys. Status Solidi A*, Vol.138, pp. 369–381, 1993.
60. N. Lehto and O. Sven, Effects of Dislocation Interactions: Application to the Period-Doubled Core of the 90° Partial in Silicon, in: *Phys. Rev. Lett.*, Vol.80, pp. 5568–5571, 1998.
61. A.S. Nandedkar and J. Narayan, Atomic structure of dislocations in silicon, germanium and diamond, in: *Philos. Mag. A*, Vol.61, pp. 873–891, 1990.

62. U. Trinczek and H. Teichler, Line Energies of 30°- and 90°-Partial Dislocations in Silicon and Germanium, in: *Phys. Status Solidi A*, Vol.137, pp. 577–589, 1993.
63. J.R.K. Bigger, D.A. McInnes, A.P. Sutton, M.C. Payne, I. Stich, R.D. King-Smith, et al., Atomic and electronic structures of the 90° partial dislocation in silicon, in: *Phys. Rev. Lett.*, Vol.69, pp. 2224–2227, 1992.
64. S. Ismail-Beigi and T.A. Arias, *Ab Initio* Study of Screw Dislocations in Mo and Ta: A New Picture of Plasticity in bcc Transition Metals, in: *Phys. Rev. Lett.*, Vol.84, pp. 1499–1502, 2000.
65. G. Wang, A. Strachan, T. Cagin, and W.A. Goddard, III, Role of core polarization curvature of screw dislocations in determining the Peierls stress in bcc Ta: A criterion for designing high-performance materials, in: *Phys. Rev. B*, Vol.67, p. 140101(R), 2003.
66. J. Bennetto, R.W. Nunes, and D. Vanderbilt, Period-Doubled Structure for the 90º Partial Dislocation in Silicon, in: *Phys. Rev. Lett.*, Vol.79, pp. 245–248, 1997.
67. R.W. Nunes, J. Bennetto, and D. Vanderbilt, Atomic structure of dislocation kinks in silicon, in: *Phys. Rev. B*, Vol.57, pp. 10388–10397, 1998.
68. X. Blase, K. Lin, A. Canning, S.G. Louie, and D.C. Chrzan, Structure and Energy of the 90º Partial Dislocation in Diamond: A Combined *Ab Initio* and Elasticity Theory Analysis, in: *Phys. Rev. Lett.*, Vol.84, pp. 5780–5783, 2000.
69. W. Cai, V.V. Bulatob, J. Chang, J. Li, and S. Yip, Periodic image effects in dislocation modelling, in: *Philos. Mag.*, Vol.83, pp. 539–567, 2003.
70. W. Cai, V.V. Bulatov, J. Chang, J. Li, and S. Yip, Anisotropic Elastic Interactions of a Periodic Dislocation Array, in: *Phys. Rev. Lett.*, Vol.86, pp. 5727–5730, 2001.
71. J. Li, C.-Z. Wang, J.-P. Chang, W. Cai, V.V. Bulatov, K.-M. Ho, et al., Core energy and Peierls stress of a screw dislocation in bcc molybdenum: A periodic-cell tight-binding study, in: *Phys. Rev. B*, Vol.70, p. 104113, 2004.
72. G. Lu, N. Kioussis, V.V. Bulatov, and E. Kaxiras, Dislocation core properties of aluminum: a first-principles study, in: *Mater. Sci. Eng. A*, Vol.309-310, pp. 142–147, 2001.
73. X.W. Zhou, D.K. Ward, J.A. Zimmerman, J.L. Cruz-Campa, D. Zubia, J.E. Martin, et al., An Atomistically Validated Continuum Model for Strain Relaxation and Misfit Dislocation Formation, in: *Submitted*
74. J. Paul, Hydrogen adsorption on Al(100), in: *Phys. Rev. B*, Vol.37, pp. 6164–6174, 1988.
75. E.P. Go, K. Thuermer, and J.E. Reutt-Robey, H adsorption and the formation of alane oligomers on Al(111), in: *Surf. Sci.*, Vol.437, pp. 377–385, 1999.
76. T. Gladman, Precipitation hardening in metals, in: *Mater. Sci. Technol.*, Vol.15, pp. 30–36, 1999.
77. E. Orowan, Session III (a). -Effects Associated with Internal Stresses.-Discussion, in: *Symp. Intern. Stress. Met. Alloys*, The Institute of Metals, London, 1948: p. 451.
78. X. Zhou, D.K. Ward, B.M. Wong, F.P. Doty, and J.A. Zimmerman, Molecular Dynamics Studies of Dislocations in CdTe Crystals from a New Bond Order Potential, in: *J. Phys. Chem. C*, Vol.116, pp. 17563–17571, 2012.
79. V. Mohles, Dislocation Dynamics Simulations of Particle Strengthening, in: D. Raabe, F. Roters, F. Barlat, L.-Q. Chen (Eds.), *Contin. Scale Simul. Eng. Mater.*, Wiley-VCH, Weinheim, Germany, 2004.
80. S. Queyreau, G. Monnet, and B. Devincre, Orowan strengthening and forest hardening superposition examined by dislocation dynamics simulations, in: *Acta Mater.*, Vol.58, pp. 5586–5595, 2010.

81. S.I.R. §, T.A. Parthasarathy, D.M. Dimiduk, and P.M. Hazzledine, Discrete dislocation simulations of precipitation hardening in superalloys, in: *Philos. Mag.*, Vol.84, pp. 3195–3215, 2004.
82. G. Monnet, Investigation of precipitation hardening by dislocation dynamics simulations, in: *Philos. Mag.*, Vol.86, pp. 5927–5941, 2006.
83. C. Ericson, *Real-Time Collision Detection*.Elsevier, San Francisco, 2004.
84. R.B. Sills, A. Aghaei, and W. Cai, Advanced Time Integration Algorithms for Dislocation Dynamics Simulations of Work Hardening, in: *Model. Simul Mater Sci Eng*, Vol.In-Preparation, 2015.
85. S.B. Pope, *Algorithms for Ellipsoids*.Cornell University, 2008.
86. A.S. Argon, *Strengthening Mechanisms in Crystal Plasticity*.Oxford University Press, New York, 2008.
87. A.J. Ardell, Precipitation hardening, in: *Metall. Trans. A*, Vol.16, pp. 2131–2165, 1985.
88. C.V. Singh and D.H. Warner, An Atomistic-Based Hierarchical Multiscale Examination of Age Hardening in an Al-Cu Alloy, in: *Metall. Mater. Trans. A*, Vol.44, pp. 2625–2644, 2013.
89. T. Mura, *Micromechanics of Defects in Solids*.Kluwer Academic Publishers, Boston, 1987.
90. C. Weinberger, W. Cai, and D. Barnett, ME340B Lecture Notes: Elasticity of Microscopic Structures, in: 2004.
91. V. Mohles and B. Fruhstorfer, Computer simulations of Orowan process controlled dislocation glide in particle arrangements of various randomness, in: *Acta Mater.*, Vol.50, pp. 2503–2516, 2002.
92. A. Winkler, Interaction of atomic hydrogen with metal surfaces, in: *Appl. Phys. Mater. Sci. Process.*, Vol.67, pp. 637–644, 1998.
93. B.P. Somerday, P. Sofronis, K.A. Nibur, C. San Marchi, and R. Kirchheim, Elucidating the variables affecting accelerated fatigue crack growth of steels in hydrogen gas with low oxygen concentrations, in: *Acta Mater.*, Vol.61, pp. 6153–6170, 2013.
94. P.M. Richards, S.M. Myers, W.R. Wampler, and D.M. Follstaedt, Mechanism of surface-limited release of hydrogen from oxidized metals, in: *J. Appl. Phys.*, Vol.65, p. 180, 1989.
95. B.J. Hinch, A. Lock, H.H. Madden, J.P. Toennies, and G. Witte, Helium-atom scattering investigation of facetting of the Al stepped (332) surface, in: *Phys. Rev. B*, Vol.42, pp. 1547–1559, 1990.
96. C. Eibl, Quantitative characterization of a highly effective atomic hydrogen doser, in: *J. Vac. Sci. Technol. Vac. Surf. Films*, Vol.16, p. 2979, 1998.
97. J.F. Ziegler and J.P. Biersack, The Stopping and Range of Ions in Matter, in: D.A. Bromley (Ed.), *Treatise Heavy-Ion Sci.*, Springer US, Boston, MA, 1985: pp. 93–129.
98. R. Beikler and E. Taglauer, Trajectory resolved analysis of LEIS energy spectra: Neutralization and surface structure, in: *Nucl. Instrum. Methods Phys. Res. Sect. B Beam Interact. Mater. At.*, Vol.182, pp. 180–186, 2001.
99. S. Markelj, O.V. Ogorodnikova, P. Pelicon, T. Schwarz-Selinger, and I. Čadež, Temperature dependence of D atom adsorption on polycrystalline tungsten, in: *Appl. Surf. Sci.*, Vol.282, pp. 478–486, 2013.
100. R.D. Kolasinski, J.A. Whaley, R.A. Karnesky, C. San Marchi, and R. Bastasz, Characterization of the Ne–Al scattering potential using low energy ion scattering maps, in:

Nucl. Instrum. Methods Phys. Res. Sect. B Beam Interact. Mater. At., Vol.269, pp. 1229–1233, 2011.

101. P. Tsong-Pyng and C.J. Altstetter, Effects of deformation on hydrogen permeation in austenitic stainless steels, in: *Acta Metall.*, Vol.34, pp. 1771–1781, 1986.
102. R.A. Causey, R.A. Karnesky, and C. San Marchi, *Tritium Barriers and Tritium Diffusion in Fusion Reactors*.Elsevier, Amsterdam, 2012.
103. C.E. Ransley and H. Neufeld, The solubility of hydrogen in liquid and solid aluminium, in: *J. Inst. Met.*, Vol.74, pp. 599–620, 1948.
104. J.R. Scully, G.A. Young Jr., and S.W. Smith, 19 - Hydrogen embrittlement of aluminum and aluminum-based alloys, in: R.P. Gangloff, B.P. Somerday (Eds.), *Gaseous Hydrog. Embrittlement Mater. Energy Technol.*, Woodhead Publishing, 2012: pp. 707–768.
105. C. San Marchi and B.P. Somerday, *Technical Reference for Hydrogen Compatibility of Materials*.Sandia National Laboratories, 2012.
106. M.O. Speidel, Hydrogen embrittlement and stress corrosion cracking of aluminum alloys, in: R. Gibala, R.F. Hehemann (Eds.), *Hydrog. Embrittlement Stress Corros. Crack.*, American Society for Metals, Metals Park, 1984: pp. 271–296.
107. P.M. Ordin, *Safety Standard for Hydrogen and Hydrogen Systems: Guidelines for Hydrogen System Design, Materials Selection, Operations, Storage and Transportation*.NASA, 1997.
108. H.K. Birnbaum, C. Buckley, F. Zeides, E. Sirois, P. Rozenak, S. Spooner, et al., Hydrogen in aluminum, in: *J. Alloys Compd.*, Vol.253-254, pp. 260–264, 1997.
109. E. Charitidou, G. Papapolymerou, G.N. Haidemenopoulos, N. Hasiotis, and V. Bontozoglou, Characterization of trapped hydrogen in exfoliation corroded aluminium alloy 2024, in: *Scr. Mater.*, Vol.41, pp. 1327–1332, 1999.
110. A.K. Zurek, R. Walser, and H.L. Marcus, Deuterium transport and trapping in aluminum alloys, in: *Metall. Trans. A*, Vol.14, pp. 1307–1312, 1983.
111. N. Imanishi, M. Ogura, M. Ikeda, R. Mitsusue, and A. Itoh, Effect of implanted silicon on hydrogen behavior in aluminum and nickel, in: *Nucl. Instrum. Methods Phys. Res. Sect. B Beam Interact. Mater. At.*, Vol.161–163, pp. 401–405, 2000.
112. H. Kamoutsi, G.N. Haidemenopoulos, V. Bontozoglou, P.V. Petroyiannis, and S.G. Pantelakis, Effect of prior deformation and heat treatment on the corrosion-induced hydrogen trapping in aluminium alloy 2024, in: *Corros. Sci.*, Vol.80, pp. 139–142, 2014.
113. E. Hashimoto and T. Kino, Hydrogen diffusion in aluminium at high temperatures, in: *J. Phys. F Met. Phys.*, Vol.13, pp. 1157–1165, 1983.
114. C. Wolverton, V. Ozolins, and M. Asta, Hydrogen in aluminum: First-principles calculations of structure and thermodynamics, in: *Phys. Rev. B*, Vol.69, pp. 144109:1–16, 2004.
115. S. Linderoth, Hydrogen diffusivity in aluminium, in: *Philos. Mag. Lett.*, Vol.57, pp. 229–234, 1988.
116. H. Saitoh, Y. Iijima, and K. Hirano, Behaviour of hydrogen in pure aluminium, Al-4 mass% Cu and Al-1 mass% Mg2Si alloys studied by tritium electron microautoradiography, in: *J. Mater. Sci.*, Vol.29, pp. 5739–5744, 1994.
117. Y. Iijima, S. Yoshida, and H. Saitoh, Hydrogen trapping in an Al-2.1 wt % Li alloy, in: *J. Mater. Sci.*, Vol.30, pp. 1290–1294, 1995.

118. Y. Iijima, S.-I. Yoshida, H. Saitoh, H. Tanaka, and K.-I. Hirano, Hydrogen trapping and repelling in an Al-6 wt % Zn-2 wt % Mg alloy, in: *J. Mater. Sci.*, Vol.27, pp. 5735–5738, 1992.
119. T. Hayashi, K. Okuno, H. Kudo, and H. Amano, Tritium diffusion and trapping associated with lithium in Al-Li systems, in: *J. Common Met.*, Vol.141, pp. 169–176, 1988.
120. M. Ji, C.-Z. Wang, K.-M. Ho, S. Adhikari, and K. Hebert, Statistical model of defects in Al-H system, in: *Phys. Rev. B*, p. 024105, 2010.
121. P.N. Anyalebechi, Analysis and Thermodynamic Prediction of Hydrogen Solution in Solid and Liquid Multicomponent Aluminum Alloys, in: J.F. Grandfield, D.G. Eskin (Eds.), *Essent. Read. Light Met.*, John Wiley & Sons, Inc., 2013: pp. 183–200.
122. M. Leger and G.R. Piercy, Internal friction in hydrogen-charged aluminium alloys, in: *Philos. Mag. A*, Vol.43, pp. 377–385, 1981.
123. D. Pérez Escobar, T. Depover, L. Duprez, K. Verbeken, and M. Verhaege, Combined thermal desorption spectroscopy, differential scanning calorimetry, scanning electron microscopy and X-ray diffraction study of hydrogen trapping in cold deformed TRIP steel, in: *Acta Mater.*, Vol.60, pp. 2593–2605, 2012.
124. J. R. Davis, ed., *Aluminum and aluminum alloys*.ASM International, Materials Park, OH, 1993.
125. J.W. Eaton, D. Bateman, and S. Hauberg, *GNU Octave version 3.0.1 manual: a high-level interactive language for numerical computations*.CreateSpace Independent Publishing Platform, 2009.
126. H.E. Kissinger, Reaction Kinetics in Differential Thermal Analysis, in: *Anal. Chem.*, Vol.29, pp. 1702–1706, 1957.
127. J. Røyset and N. Ryum, Kinetics and mechanisms of precipitation in an Al–0.2wt.% Sc alloy, in: *Mater. Sci. Eng. A*, Vol.396, pp. 409–422, 2005.
128. H. Kaya, Dependence of electrical resistivity on temperature and composition of Al–Cu alloys, in: *Mater. Res. Innov.*, Vol.16, pp. 224–229, 2012.
129. J. Klimeš, Van der Waals density functionals applied to solids, in: *Phys. Rev. B*, Vol.83, p. 195131, 2011.
130. P.E. Blöchl, Projector augmented-wave method, in: *Phys. Rev. B*, Vol.50, pp. 17953–17979, 1994.
131. G. Kresse, From ultrasoft pseudopotentials to the projector augmented-wave method, in: *Phys. Rev. B*, Vol.59, pp. 1758–1775, 1999.
132. G. Kresse, *Ab initio* molecular dynamics for liquid metals, in: *Phys. Rev. B*, Vol.47, pp. 558–561, 1993.
133. G. Kresse, *Ab initio* molecular-dynamics simulation of the liquid-metal–amorphous-semiconductor transition in germanium, in: *Phys. Rev. B*, Vol.49, pp. 14251–14269, 1994.
134. G. Kresse and J. Furthmüller, Efficiency of ab-initio total energy calculations for metals and semiconductors using a plane-wave basis set, in: *Comput. Mater. Sci.*, Vol.6, pp. 15–50, 1996.
135. G. Kresse, Efficient iterative schemes for *ab initio* total-energy calculations using a plane-wave basis set, in: *Phys. Rev. B*, Vol.54, pp. 11169–11186, 1996.
136. H.J. Monkhorst and J.D. Pack, Special points for Brillouin-zone integrations, in: *Phys. Rev. B*, Vol.13, pp. 5188–5192, 1976.
137. G. Simmons and H. Wang, *Single Crystal Elastic Constants and Calculated Aggregate Properties: A Handbook*.MIT Press, Cambridge, 1971.

138. C.I. Smithels, *Metals Reference Book*.Butterworths, London, 1976.

139. F.R. Eshelman and J.F. Smith, Single-crystal elastic constants of Al2Cu, in: *J. Appl. Phys.*, Vol.49, p. 3284, 1978.

140. ALLOY DATABASE, in: http://alloy.phys.cmu.edu

141. L.E. Murr, *Interfacial Phenomena in Metals and Alloys*.Addison-Wesley, Reading, MA, 1975.

142. W.R. Tyson and W.A. Miller, Surface free energies of solid metals: Estimation from liquid surface tension measurements, in: *Surf. Sci.*, Vol.62, pp. 267–276, 1977.

143. R.H. Rautioaho, An Interatomic Pair Potential for Aluminium Calculation of Stacking Fault Energy, in: *Phys. Status Solidi B*, Vol.112, pp. 83–89, 1982.

144. K.H. Westmacott and R.L. Peck, A rationalization of secondary defect structures in aluminium-based alloys, in: *Philos. Mag.*, Vol.23, pp. 611–622, 1971.

145. C.B. Carter and I.L.F. Ray, On the stacking-fault energies of copper alloys, in: *Philos. Mag.*, Vol.35, pp. 189–200, 1977.

146. H.-E. Schaefer, R. Gugelmeier, M. Schmolz, and A. Seeger, Positron Lifetime Spectroscopy and Trapping at Vacancies in Aluminium, in: *Mater. Sci. Forum*, Vol.15-18, pp. 111–116, 1987.

147. R.W. Siegel, Vacancy concentrations in metals, in: *J. Nucl. Mater.*, Vol.69-70, pp. 117–146, 1978.

148. H. Ullmaier, ed., *Properties and Interaction of Atomic Defects in Metals and Alloys*.Springer, Berlin, 1991.

149. R.C. Weast, *CRC handbook fo chemistry and physics*.CRC, Boca Raton, FL, 1983.

150. W. Eckstein and R. Bastasz, A simple representation for the angular dependence of scattered and recoil particle energies, in: *Nucl. Instrum. Methods Phys. Res. Sect. B Beam Interact. Mater. At.*, Vol.29, pp. 603–608, 1988.

151. C.J. Barnes, H. Asonen, A. Salokatve, and M. Pessa, Growth mode and electronic structure of copper films on aluminium substrates, in: *Surf. Sci.*, Vol.184, pp. 163–176, 1987.

152. J.D.R. Buchanan, T.P.A. Hase, B.K. Tanner, P.J. Chen, L. Gan, C.J. Powell, et al., Anomalously large intermixing in aluminum–transition-metal bilayers, in: *Phys. Rev. B*, Vol.66, p. 104427, 2002.

153. L. Vitos, A.V. Ruban, H.L. Skriver, and J. Kollár, The surface energy of metals, in: *Surf. Sci.*, Vol.411, pp. 186–202, 1998.

APPENDIX A: QUANTUM MECHANICAL STUDIES OF AL-CU SYSTEMS

Density functional theory (DFT) calculations are performed using the optB86b-vdW functional [129] with spin-polarization and projector-augmented-wave (PAW) [130,131] pseudopotentials within VASP [132–135]. Due in part to the inclusion of non-local correlation (i.e. van der Waals interactions), the optB86b-vdW exchange-correlation functional improves over transitional generalized-gradient approximation (GGA) functionals (e.g. PBE) for a range of solids on the prediction of lattice constants, cohesive energies, and bulk moduli [129]. For all calculations a cutoff energy of 500 eV for the plane-wave basis set was used and full geometry optimizations (ions and unit cell) were performed until all forces were smaller than 0.01 eV/Å. For bulk lattices, the Brillouin zone was sampled using a 10 × 10 × 10 gamma-centered Monkhorst-Pack grid [136]. For small clusters, the calculations are carried out in a 25 Å^3 box using a gamma-point Brillouin zone. The reference potential energy curves for the $H + H_2 \rightarrow H_2 + H$ reaction were generated at the CCSD(T) level of theory using the Aldrich triple-zeta basis set with polarization (TZVP). The CCSD(T) method is the current gold-standard in quantum chemistry and is capable of accurately modeling reaction barriers.

The energies and atomic spacings of various clusters, consisting of four or less atoms for the elemental Al, Cu, and H, are given in Table 9 and for the binary AlCu, AlH, and CuH in Table 10. A stable configuration for the H trimer could not be determined. Figure 45 shows the energy profile for attempting to form a trimer. These simulations begin with an optimized H_2 molecule and the total energy is calculated as a function of an approaching third H atom. The results clearly show that as the third atom approaches the dimer, the energy increases. Eventually, the third atom is closer than the spacing of the initial dimer and a new dimer is formed causing one of the H atoms of the initial dimer to be pushed away. This series of simulations clearly demonstrates that there is no stable cluster structure to accommodate three H atoms. The cohesive energies and atomic volumes of various elemental Al, Cu, and H and the binary AlCu, AlH, and CuH elemental lattice structures are given in Table 11-Table 13. It should be noted that the experimental values for the Al and Cu fcc structures [24,54,55] are in good agreement. In addition, the dilute heat of solution for Cu in fcc Al was also obtained from DFT as 0.40 eV.

Table 10. Cohesive energies Ec (eV/atom) and atom spacing r (Å) of various Al, Cu, and H clusters. CCSD(T) values are given in parenthesis. For chain r values, the first value is the exterior bond length and the second number is the internal bond length.

Structure	**Al**		**Cu**		**H**	
	E_c	r	E_c	r	E_c	r
tetra	-1.48158 (-1.17070)	2.70 (2.82)	-1.32946 (-2.14910)	2.37 (2.58)	-0.11078	1.39
square	-1.59793 (-1.16843)	2.65 (2.73)	-1.37597 (-2.22392)	2.30 (2.40)	-0.75886	1.18
trimer	-1.39647 (-1.11382)	2.52 (2.54)	-1.24050 (-2.14445)	2.32 (2.42)	unstable	unstable
dimer	-0.83325 (-0.32865)	2.76 (2.58)	-1.14822 (-2.11369)	2.21 (2.30)	-2.48282 (-2.25)	0.75

chain	-1.27933 (-0.77727)	2.73, 2.52 (2.51,2.45)	-1.22991 (-2.20998)	2.34, 2.77 (2.33, 2.49)	-2.48317	0.75, 3.80

Table 11. Cohesive energies E_c (eV/atom), atomic spacing r (Å), and angles θ (deg.) of various Al-Cu clusters. For ABA trimers the first r value is distance between A-B, the second r value is distance between A-A, the first θ is centered B, the second θ is centered at either A. For $(AB)_2$-rhom the first θ is centered on A and the second θ is centered on B. For A_3B-tet first r is between A-A and second r is between A-B

Structure	**DFT**		
	E_c	r	θ
AlCu-di	-1.37145	2.34	-----
AlCuAl-tri	-1.62658	2.36, 2.54	65.3, 57.4
CuAlCu-tri	-1.57430	2.43, 2.28	56.0, 62.0
AlH-di	-1.66351	1.68	-----
AlHAl-tri	-1.63398	1.83, 2.49	85.9, 47.1
HAlH-tri	-1.68544	2.84, 0.75	15.4, 82.3
Al_3H-tet	-1.82973	2.56, 1.89	-----
$(AlH)_2$-rhom	-2.03100	1.84	71.5, 108.5
CuH-di	-1.56420	1.46	-----
CuHCu-tri	-1.44944	1.55, 2.46	104.9, 37.6
HCuH-tri	-1.64296	1.89, 0.78	23.8, 78.1
Cu_3H-tet	-1.40526	2.44, 1.63	-----
$(CuH)_2$-rhom	-1.72299	1.74	104.6, 75.4

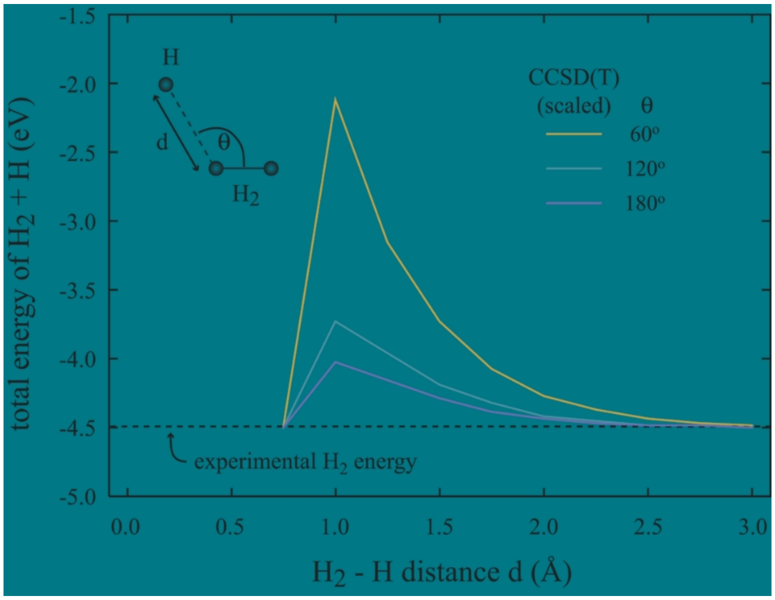

Figure 47. Scaled CCSD(T) energy profiles of H + H_2 → H_2 + H reaction at different incoming atom incident angle θ. The horizontal dash line shows the experimental total cohesive energy of an H_2 molecule.

Table 12. Cohesive energies Ec (eV/atom) and atomic volumes Ω (Å3/atom) of various Al, Cu, and H lattices obtained from DFT. Experimental values are given in parenthesis. [54,55]

Structure	Al		Cu		H	
	E_c	Ω	E_c	Ω	E_c	Ω
fcc	-3.61073 (-3.39)	16.4 (16.6)	-3.8093 (-3.47)	11.6 (11.8)	-1.23543	3.0
hcp	-3.58501	16.6	-3.7876	11.7	-1.54075	3.4
bcc	-3.51407	17.0	-3.7685	11.6	-1.21651	3.0
sc	-3.26314	20.3	-3.3224	13.5	-1.35517	23.6
dc	-2.98993	27.3	-2.7082	18.2	-1.72392	3.4

Table 13. Cohesive energies E_c (eV/atom) and atomic volumes Ω (Å^3/atom) of various Al_nCu_m compound lattices obtained from DFT. Experimental values given in parenthesis [24,55].

Structure	DFT	
	E_c	Ω
Al_3Cu-L2$_1$	-3.69027	14.9
Al_2Cu-θ' (CaF_2)	-3.86901	15.9
Al_2Cu-θ	-3.83957 (-3.44)	14.8 (14.9)
AlCu-zb	-3.11251	20.5
AlCu-B1	-3.50440	15.7
AlCu-B2	-3.73158	15.7
AlCu-L1$_0$	-3.85737	13.4
$AlCu_2$-c16	-3.64204	13.6
$AlCu_3$-L2$_1$	-3.92456	12.3
$AlCu_3$-D022	-3.92526	12.2

Table 14. Cohesive energies E_c (eV/atom) and atomic volumes Ω (Å^3/atom) of various X-H compound lattices obtained from DFT, where X is either Al or Cu.

Structure	Al		Cu	
	E_c	Ω	E_c	Ω
XH-CsCl	-2.24018	10.0	-2.59551	7.5
XH-gra	-2.64402	10.6	-2.93475	8.0
XH-grap	-2.12851	-----	-2.68304	-----
XH-NaCl	-2.65263	9.4	-2.90665	7.1
XH-fcs	-2.17880	-----	-2.70873	-----
XH-wz	-2.67156	10.5	-2.95572	7.7
XH-zb	-2.67684	10.5	-3.01791	7.8
XH-R-3C	-2.81046	9.4	-----	-----
XH-fluorite	-2.57381	8.2	-----	-----
XH-rutile	-2.60165	9.6	-----	-----

APPENDIX B: DETAILED COMPARISON BETWEEN DIFFERENT ATOMISTIC MODELING METHODS

Table 15. Cohesive energies E_c (eV/atom) and atomic volumes Ω (Å^3/atom) of various Al lattices obtained from different methods.

Model/Exp.	fcc		hcp		bcc		sc		dc	
	E_c	Ω	E_c	Ω	E_c	Ω	E_c	Ω	E_c	Ω
EAM-CY	-3.31832	16.6	-3.31806	16.6	-3.30162	16.7	-3.06265	19.4	-2.68963	35.2
EAM-Mishin1	-3.36000	16.6	-3.33221	17.0	-3.25453	16.9	-2.96141	20.6	-2.46907	27.6
EAM-BAM	-3.36000	16.6	-3.34804	17.3	-3.27338	19.1	-3.31109	19.8	-2.92429	22.4
EAM-VC	-3.36846	16.6	-3.35424	16.9	-3.29450	17.2	-3.22880	19.7	-2.71189	24.0
EAM-MSAH	-3.36971	16.4	-3.34233	16.5	-3.29621	16.7	-3.03994	19.9	-2.47949	26.3
EAM-Zhou	-3.58000	17.0	-3.57104	17.3	-3.52296	17.8	-3.38123	19.9	-3.00468	23.3
EAM-MKBA	-3.41066	16.5	-3.38314	16.6	-3.30883	17.0	-3.09830	20.0	-2.59845	24.2
EAM-JNP	-3.38764	15.9	-3.38892	15.8	-3.37325	15.9	-3.02978	18.2	-2.53042	26.1
MEAM	-3.58000	16.6	-3.54878	16.7	-3.47192	16.0	-3.22432	19.1	-2.45695	33.2
REAX-LJGS	-3.23777	16.0	-3.23778	16.0	-3.17827	15.9	-2.94002	22.2	-2.49575	25.0
REAX-Ojwang	-3.42575	16.3	-3.42554	16.3	-3.36293	16.0	-2.86859	22.5	-2.23815	26.4
BOP	-3.36098	16.6	-3.33399	16.6	-3.30463	16.4	-3.09708	19.5	-2.22597	24.4
DFT	-3.61073	16.4	-3.58501	16.6	-3.51407	17.0	-3.26314	20.3	-2.98993	27.3
Exp. [54,55]	-3.39	16.6	------	------	------	------	------	------	------	------

Table 16. Cohesive energies E_c (eV/atom) and atomic volumes Ω (Å^3/atom) of various Cu lattices obtained from different methods.

Model/Exp.	fcc		hcp		bcc		sc		dc	
	E_c	Ω	E_c	Ω	E_c	Ω	E_c	Ω	E_c	Ω
EAM-Mendelev	-3.28312	12.0	-3.27636	12.0	-3.24271	12.1	-2.66223	13.9	-2.13886	21.0
EAM-Zhou	-3.53980	11.8	-3.52485	11.7	-3.48764	11.3	-3.15797	13.8	-2.59921	17.8
EAM-Mishin2	-3.54000	11.8	-3.53218	11.8	-3.49449	11.8	-3.10686	13.7	-2.41920	19.2
EAM-Foiles	-3.54000	11.8	-3.53762	11.8	-3.51015	11.8	-3.11167	13.7	-2.50254	19.3
EAM-FBD	-3.54000	11.8	-3.53693	11.8	-3.51164	11.8	-3.10575	13.6	-2.46351	19.1
EAM-AFW	-3.54000	11.8	-3.53678	11.8	-3.51087	11.8	-3.09318	13.6	-2.43813	19.2
EAM-CY	-3.52457	11.8	-3.52518	11.8	-3.50214	11.8	-3.10750	13.9	-2.58687	20.3
MEAM	-3.54000	11.9	-3.52739	11.9	-3.49798	10.9	-3.33533	12.6	-2.81232	18.2
BOP	-3.47330	11.8	-3.46685	11.8	-3.42609	11.8	-3.03076	13.8	-2.37348	18.4
DFT	-3.8093	11.6	-3.7876	11.7	-3.7685	11.6	-3.3224	13.5	-2.7082	18.2
Exp. [54,55]	-3.47	11.8	------	------	------	------	------	------	------	------

Table 17. Cohesive energies E_c (eV/atom) and atomic volumes Ω (Å^3/atom) of various Al_nCu_m compound lattices obtained from different methods. Note that the relaxed structure may be different from the initial structure. Such unstable structures are included in the table to provide additional verification of the lowest energy phases. (* Indicates those structures that do not maintain the original configuration but remain crystalline.)

Model/Exp.	EAM-CY		ADP		BOP		DFT		Exp. [24,55]	
	E_c	Ω	E_c	Ω	E_c	Ω	E_c	Ω	E_c	Ω
Al_3Cu-L2_1	-3.50417	15.2	-3.31466	11.7	-3.40932	14.1	-3.69027	14.9	-----	-----

Al$_3$Cu-D022	-3.52297	15.1	-3.45103	13.8	-3.52121	14.7	-----	-----	-----	-----
Al$_3$Cu-L1$_2$	-3.52109	15.1	-3.30530	13.7	-3.55840	14.8	-----	-----	-----	-----
Al$_2$Cu-θ' (CaF$_2$)	-3.26127	17.5	-3.62259	15.0	-3.67715	15.6	-3.86901	15.9	-----	-----
Al$_2$Cu-θ	-3.48060	15.2	-3.60977	14.4	-3.58819	14.6	-3.83957	14.8	-3.44	14.9
Al$_2$Cu-cP4	-2.64727	30.4	-2.76233	16.6	-2.23599	15.3	-----	-----	-----	-----
AlCu-zb	-2.78406	22.7	-2.98128	16.2	-2.73423	18.4	-3.11251	20.5	-----	-----
AlCu-wz	-2.97643	20.7	-3.31938	16.5	-2.73435	18.5	-----	-----	-----	-----
AlCu-B1	-3.26408	16.2	-3.52851	14.9	-3.01827	15.0	-3.50440	15.7	-----	-----
AlCu-B2	-3.61074	13.9	-4.08530	11.5	-3.36516	13.6	-3.73158	15.7	-----	-----
AlCu-B8$_1$	-3.63198	13.7	-3.69681	13.1	-3.38405	13.5	-----	-----	-----	-----
AlCu-B33	-3.61810	13.9	-3.78424	12.2	-3.38351	14.0	-----	-----	-----	-----
AlCu-L1$_0$	-3.63583	13.8	-4.08530*	11.5	-3.41128	13.8	-3.85737	13.4	-----	-----
AlCu-L1$_1$	-3.63221	13.8	-3.57746*	13.5	-3.38495	13.5	-----	-----	-----	-----
AlCu-gra	-3.09286	17.9	-2.70701	21.9	-3.18001	14.0	-----	-----	-----	-----
AlCu-grap	-2.51260	-----	-2.22658	-----	-2.17544	-----	-----	-----	-----	-----
AlCu-fcs	-2.70600	-----	-2.60970	-----	-2.33810	-----	-----	-----	-----	-----
AlCu$_2$-CaF$_2$	-3.20420	16.4	-3.58880	14.0	-2.67958	15.2	-----	-----	-----	-----
AlCu$_2$-c16	-3.38292	14.5	-3.55848	13.3	-2.96290	12.9	-3.64204	13.6	-----	-----
AlCu$_2$-cP4	-2.45412	35.0	-2.64423	16.0	-1.88495	22.5	-----	-----	-----	-----
AlCu$_3$-L2$_1$	-3.62632	12.8	-3.76657	10.7	-3.18910	12.8	-3.92456	12.3	-----	-----
AlCu$_3$-D022	-3.64533	12.7	-3.73961	11.2	-3.18910	12.8	-3.92526	12.2	-----	-----
AlCu$_3$-L1$_2$	-3.64318	12.7	-3.65695	10.8	-3.12571	13.2	-----	-----	-----	-----

Table 18. Elastic constants C_{11}, C_{12}, and C_{44} (GPa) and melting temperature T_m (K) for Al-fcc as obtained from different methods.

Model/Exp.	C_{11}	C_{12}	C_{44}	T_M
EAM-CY	90.0	70.7	33.1	756±19
EAM-Mishin1	113.5	61.3	31.6	1044±34
EAM-BAM	114.0	62.0	31.6	316±4
EAM-VC*	95.5	78.5	19.0	612±12
EAM-MSAH	115.9	61.4	33.4	954±28
EAM-Zhou	127.1	81.4	36.4	644±13
EAM-MKBA	105.1	59.5	30.7	935±37
EAM-JNP	111.4	85.1	45.9	1054±37
MEAM	112.3	66.2	28.0	981±31
REAX-LJGS	118.0	60.8	60.8	820±24
REAX- Ojwang	161.9	85.9	85.9	1376±74
BOP	114.9	62.6	31.6	947±36
Exp. [137,138]	114	62	32	933

*The literature for the EAM-VC potential [27] reports elastic constants of C11=107GPa, C12=65.2 GPa, and C44=32.2 GPa. Using the potential tables provided by LAMMPS [52,53] we were unable to reproduce these numbers.

Table 19. Elastic constants C_{11}, C_{12}, and C_{44} (GPa) and melting temperature T_m (K) for Cu-fcc as obtained from different methods.

Model/Exp.	C_{11}	C_{12}	C_{44}	T_M
EAM-Mendelev	178.3	128.6	85.2	1374±65
EAM-Zhou	180.4	117.1	70.7	1141±42

EAM- Mishin2	169.9	122.7	76.2	1333±50
EAM-Foiles	168.6	123.5	76.6	1257±57
EAM-FBD	167.3	124.2	76.4	1278±57
EAM-AFW	168.1	123.5	76.6	1314±70
EAM-CY	168.3	127.0	75.1	1219±46
MEAM	170.2	122.7	75.9	1340±75
BOP	176.1	124.9	82.0	1388±68
Exp. [137]	176	125	82	1356

Table 20. Elastic constants C_{11}, C_{12}, and C_{44} (GPa) for θ and θ' phases of the Al_2Cu compound as obtained from different methods (subperscript "^{o}" refers to unrelaxed values).

Phase	Property	ADP	EAM-CY	BOP	DFT	Exp. [139,140]
θ'	C_{11}	193	130	134	179	-----
	C_{44}^{o}	47	0	55	80	-----
	C_{44}	20	0	24	-----	-----
	C_{12}	111	116	54	64	-----
θ	C_{11}	199	103	113	144	186
	C_{33}	278	126	128	175	179
	C_{44}^{o}	79	7	42	45	29
	C_{44}	48	5	27	-----	-----
	C_{66}^{o}	21	15	41	23	47
	C_{66}	9	11	16	-----	-----
	C_{12}	98	130	49	38	72
	C_{13}	116	84	73	71	79

Table 21. Al-fcc surface energies γ_{100}, γ_{110}, γ_{111} and stacking fault energy γ_{sf}(mJ/m^2) as obtained from different methods.

Model/Exp.	γ_{100}	γ_{110}	γ_{111}	γ_{sf}
EAM-CY	583	631	526	1
EAM-Mishin1	947	1013	873	141
EAM-BAM	1017	1154	1003	85
EAM-VC	862	969	829	71
EAM-MSAH	194	328	138	126
EAM-Zhou	868	958	832	44
EAM-MKBA	495	582	427	125
EAM-JNP	977	1055	910	0
MEAM	903	944	599	141
REAX-LJGS	481	483	427	0
REAX- Ojwang	810	848	711	1
BOP	979	1069	850	133
DFT	1063	1098	987	------
Exp. [141–144]	980-1140	980-1140	980-1140	120-144

Table 22. Cu-fcc surface energies γ_{100}, γ_{110}, γ_{111} and stacking fault energy γ_{sf}(mJ/m^2) as obtained from different methods.

Model/Exp.	γ_{100}	γ_{110}	γ_{111}	γ_{sf}
EAM-Mendelev	1089	1160	903	37
EAM-Zhou	1517	1649	1449	86
EAM-Mishin2	1354	1488	1243	45
EAM-Foiles	1213	1332	1097	14
EAM-FBD	1297	1424	1183	18
EAM-AFW	1330	1460	1217	19
EAM-CY	1260	1371	1170	0
MEAM	1660	1604	1413	72
BOP	1814	1948	1570	37
DFT	1876	1936	1665	-----
Exp. [142,145]	1790	1790	1790	45

Table 23. Intrinsic defect energies (eV) of various point defects in Al-fcc as obtained from different methods.

Model/Exp.	V	I_O	I_{111}	I_{110}	I_{100}
EAM-CY	0.72	1.96	2.11	2.06	1.90
EAM- Mishin1	0.67	2.77	3.00	2.92	2.57
EAM-BAM	0.52	1.81	2.09	1.95	1.76
EAM-VC	0.63	2.07	2.49	2.26	2.04
EAM-MSAH	0.67	2.50	2.88	2.69	2.39
EAM-Zhou	0.71	1.85	1.96	1.89	1.75
EAM-MKBA	0.66	2.40	2.61	2.57	2.30
EAM-JNP	1.16	2.50	2.62	2.53	2.37
MEAM	0.56	3.06	1.89	2.04	2.64
REAX-LJGS	0.71	3.49	3.77	3.54	3.14
REAX-Ojwang	1.14	4.85	4.88	4.72	4.24
BOP	0.97	1.37	1.71	2.12	1.54
DFT	0.47	1.36	1.41	1.74	2.19
Exp. [146]	0.68	-----	-----	-----	-----

Table 24. Intrinsic defect energies (eV) of various point defects in Cu-fcc as obtained from different methods.

Defect	V	I_O	I_{111}	I_{110}	I_{100}
EAM-Mendelev	1.05	2.96	2.94	3.01	2.78
EAM-Zhou	1.32	2.62	2.76	2.65	2.44
EAM-Mishin2	1.27	3.22	3.51	3.34	3.05
EAM-Foiles	1.20	3.06	3.29	3.15	2.94
EAM-FBD	1.28	3.01	3.20	3.08	2.84
EAM-AFW	1.33	3.10	3.29	3.16	2.92
EAM-CY	1.27	3.15	3.29	3.23	2.91
MEAM	1.10	2.54	3.20	3.62	2.51
BOP	1.26	2.42	2.59	2.88	2.29

DFT	1.21	3.31	3.59	3.35	2.75
Exp. [147,148]	1.27	2.8-4.2	-----	-----	-----

Table 25. Cohesive energies E_c (eV/atom) and atomic volumes Ω (Å^3/atom) of various Al-H structures obtained from BOP and DFT calculations. Available experimental data are also shown.

Model/Exp.	BOP		DFT (scaled)		DFT (original)		Exp. [39,54,55,149]	
	E_c	Ω	E_c	Ω	E_c	Ω	E_c	Ω
Al-fcc	-3.3611	16.6012	-3.3600	16.6077	-3.6107	16.4165	-3.360	16.60
$AlH_{0.25,T}$-fcc	-2.9644	14.7945	-3.0736	14.0834	-3.2543	13.9534	-----	-----
$AlH_{0.25,O}$-fcc	-2.9117	14.2328	-3.0417	13.8198	-3.2206	13.6922	-----	-----
AlH-zb	-2.4987	12.3872	-2.5839	10.5406	-2.6768	10.4795	-----	-----
AlH-wz	-2.4992	12.3507	-2.5788	10.5481	-2.6716	10.4870	-----	-----
AlH-B1	-2.4342	9.5403	-2.5605	9.4615	-2.6526	9.4067	-----	-----
AlH-gra	-2.4141	11.3986	-2.5522	10.6369	-2.6440	10.5753	-----	-----
AlH_2-rut	-2.3665	11.0654	-2.5414	9.6267	-2.6017	9.5895	-----	-----
AlH_2-θ’	-2.3601	9.6026	-2.5186	8.1865	-2.5783	8.1549	-----	-----
H_2-di	-2.2468	-----	-2.4828	-----	-2.4828	-----	-2.247	-----
AlH-B2	-2.2695	8.5718	-2.1624	10.0266	-2.2402	9.9686	-----	-----
AlH-fcs	-2.0584	-----	-2.1032	-----	-2.1788	-----	-----	-----
AlH-grap	-2.0652	-----	-2.5046	-----	-2.1285	-----	-----	-----
$(AlH)_2$-para	-1.4922	-----	-1.9605	-----	-2.0310	-----	-----	-----
Al_3H-tetra	-1.1323	-----	-1.7344	-----	-1.8297	-----	-----	-----
AlH_2-tri	-1.4979	-----	-1.6464	-----	-1.6854	-----	-----	-----
AlH-di	-1.0814	-----	-1.6058	-----	-1.6635	-----	-----	-----
Al_2H-tri	-1.1806	-----	-1.5583	-----	-1.6340	-----	-----	-----

Table 26. Cohesive energies E_c (eV/atom) and atomic volumes Ω (Å^3/atom) of various Cu-H structures.

Structure	BOP		DFT		Scaled DFT		Exp. [54,55]	
	E_c	Ω	E_c	Ω	E_c	Ω	E_c	Ω
CuH_3-tetra	-1.16	-----	-1.41	-----	-1.28	-----	-----	-----
Cu_2H-tri	-1.17	-----	-1.45	-----	-1.32	-----	-----	-----
CuH_2-tri	-1.50	-----	-1.64	-----	-1.50	-----	-----	-----
$(CuH)_2$-rhom	-1.54	-----	-1.72	-----	-1.57	-----	-----	-----
H_2-di	-2.25	-----	-2.48	-----	-2.25	-----	-2.25	-----
CuH-CsCl	-2.24	5.80	-2.60	7.55	-2.37	7.69	-----	-----
CuH-grap	-2.19	-----	-2.68	-----	-2.45	-----	-----	-----
CuH-NaCl	-2.48	6.31	-2.91	7.14	-2.66	7.27	-----	-----
CuH-gra	-2.56	7.58	-2.93	7.99	-2.68	8.14	-----	-----
CuH-wz	-2.61	7.61	-2.96	7.68	-2.70	7.82	-----	-----
CuH-zb	-2.61	7.61	-3.02	7.85	-2.76	7.99	-----	-----
Cu_4H-O	-2.99	9.86	-3.43	9.84	-3.13	10.04	-----	-----
Cu_4H-T	-3.04	10.19	-3.45	9.99	-3.15	10.20	-----	-----

Cu-fcc	-3.47	11.81	-3.81	11.56	-3.47	11.81	-3.47	11.81

APPENDIX C: DISLOCATION ENERGY UNDER PERIODIC BOUNDARY CONDITIONS

Following the previous approach for edge dislocations [17], the dislocation line energy Γ for periodic mixed dislocations with a mixed angle β can be derived as:

$$\Gamma = E_c + \sin^2\beta \cdot E_{0,edge} + \cos^2\beta \cdot E_{0,screw} + 2\sin^2\beta \cdot \sum_{i=1}^{\infty} E_{i,edge} + 2\cos^2\beta \cdot \sum_{i=1}^{\infty} E_{i,screw} \qquad \text{(C1)}$$

where

$$E_{0,edge} = \frac{Gb^2}{4\pi(1-\nu)} \left\{ \ln\left(\frac{d}{2r_0}\right) + \ln\left(\frac{L_y - d}{L_y - 2r_0}\right) - \ln\left[Ga\left(\frac{L_y + d}{L_y}\right)\right] - \ln\left[Ga\left(2 - \frac{d}{L_y}\right)\right] \right\} \qquad \text{(C2)}$$

$$E_{0,screw} = \frac{Gb^2}{4\pi} \left\{ \ln\left(\frac{d}{2r_0}\right) + \ln\left(\frac{L_y - d}{L_y - 2r_0}\right) - \ln\left[Ga\left(\frac{L_y + d}{L_y}\right)\right] - \ln\left[Ga\left(2 - \frac{d}{L_y}\right)\right] \right\} \qquad \text{(C3)}$$

$$E_{i,edge} = \frac{Gb^2}{8\pi(1-\nu)} \left\{ \begin{array}{c} \dfrac{4\pi \cdot i \cdot L_x \cdot \coth\left(\dfrac{\pi \cdot i \cdot L_x}{L_y}\right) \cdot \sin^2\left(\dfrac{\pi \cdot d}{L_y}\right)}{L_y \cdot \cosh\left(\dfrac{2\pi \cdot i \cdot L_x}{L_y}\right) - L_y \cdot \cos\left(\dfrac{2\pi \cdot d}{L_y}\right)} \qquad + \\ \ln\left[\cos^2\left(\dfrac{\pi \cdot d}{L_y}\right) + \coth^2\left(\dfrac{\pi \cdot i \cdot L_x}{L_y}\right) \cdot \sin^2\left(\dfrac{\pi \cdot d}{L_y}\right)\right] \end{array} \right\} \qquad \text{(C4)}$$

$$E_{i,screw} = \frac{Gb^2}{8\pi} \left\{ \ln\left[\cos^2\left(\frac{\pi \cdot d}{L_y}\right) + \coth^2\left(\frac{\pi \cdot i \cdot L_x}{L_y}\right) \cdot \sin^2\left(\frac{\pi \cdot d}{L_y}\right)\right] + \right\} \qquad \text{(C5)}$$

In Eqs. (C1) – (C5), E_c and r_0 are the core energy and core radius of an isolated dislocation, *Ga* is an Euler gamma function, coth and cosh are hyperbolic functions, G is shear modulus, ν is Poisson's ratio, and *b* is Burgers magnitude. Note that the summation in Eq. (B1) converges very fast so that the error is negligible if a few terms are included (in the present work, we included 100 terms so that our results are virtually indistinguishable from the full series).

APPENDIX D: DETAILS ON LEIS AND DRS MEASUREMENTS

Using classical kinematics, one can determine the composition of surfaces with LEIS and DRS by analyzing the energies of scattered and recoiled atoms. Let us assume the binary collision approximation is valid, and that only particles that scatter within a plane containing the incident beam and the surface normal are of interest. For convenience we define a mass ratio $A = m_2 / m_1$, where m_2 and m_1 refer to the atomic masses of the surface atom and the incident ion, respectively. The following straightforward expression relates this mass ratio to the observation angle and the scattered particle energy (E^E):

$$\cos\theta = (1 + A)\sqrt{E / E_0} + (1 - A(1 - Q_n))/\sqrt{E / E_0} \tag{D1}$$

Note that we define E_0 as the initial beam energy, and Q_n is accounts for inelastic energy loss during the collision. With all other quantities in the above expression known, one may solve for the mass ratio A analytically to identify surface species. The above equation applies to scattered particles, and a similar expression may easily be derived for recoiled particles, as described in Ref. [150].

APPENDIX E: ATOMIC SCALE MEASUREMENTS OF THE INTERMIXING IN CU/AL HETEROSTRUCTURES

In the last month of this project we started experimental work to measure the Cu-Al intermixing with atomic precision. We aim to achieve unprecedented accuracy by depositing Cu onto single-crystal Al surfaces under precisely controlled conditions in ultrahigh vacuum (UHV), and subsequently analyzing the Cu/Al interface directly with atom probe tomography (APT). So far, the Cu/Al interface has been characterized only with the somewhat crude and indirect techniques of auger spectroscopy (AES), work function measurements, LEED, and x-ray reflectometry, leading to a rather contradictory and incomplete picture. For example, reports of the width of the intermixing layer range from less than1 nm[151] to more than 16 nm [152]. Since intermixing is very sensitive to the details of the Cu-Al interaction, obtaining experimental intermixing data with atomic-scale precision will allow atomic models of the Cu-Al interaction to be tested rigorously. We also want to test whether intermixing can be explained by the following scenario: After depositing a fraction of a Cu monolayer (ML) the sample surface should be partially covered by Cu islands surrounded by exposed Al surface. The lower surface energy of Al compared to Cu (1.15 vs. 1.8 J/m2 [153]) is then expected to drive Al atoms' migration to the top of Cu islands, thus burying Cu beneath Al. Such a process would explain why the intermixing layer is much wider when Cu is deposited onto Al compared to Al grown onto Cu, as reported in Ref.[152].

For our experiments we prepared an atomically flat single crystal Al(001) surface using more than 100 cycles of ion bombardment and annealing in UHV. The Auger electron spectrum (AES) in Figure 44(a) demonstrates the extreme cleanliness of the prepared Al(001) surface. Onto this surface, we then grew a 40 nm thick Cu film using an electron-beam evaporator, which was newly installed in the same UHV chamber. The deposition occurred at ambienttemperature with a rate of 1 atomic layer per minute. Figure 44(b) shows AES intensity exclusively originating from Cu; the Cu/Al interface has thus been prepared with extreme cleanliness. To examine the buried Cu/Al interface with atom probe tomography the sample has to be removed from this chamber and exposed to air. To exclude the possibility of contaminating the interface we deposited a 20 nm thick protective Ag layer using a newly installed e-beam evaporator (corresponding AES shown in Figure 44(c)).

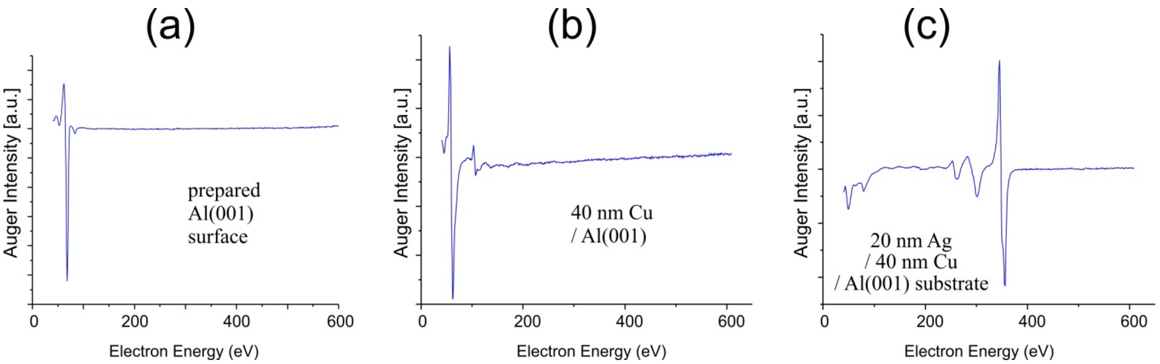

Figure 46. Auger Electron Spectra of (a) the clean Al(001) surface, (b) the 40 nm thick Cu film deposited onto the Al(001) surface, and (c) the Cu/Al(001) film covered by a 20 nm thick Ag protection layer.

At this stage the sample is under ultra-high vacuum and ready to be cut it into tip-shaped samples suitable for atom probe tomography (APT). APT, which can distinguish between individual Cu and Al atoms, will yield a detailed map of the buried Cu/Al interface with sub-nanometer resolution. This direct spatial information will allow us to quantify the extent of Cu-Al intermixing.

At the time of writing this report, the Cu/Al interface sample is put on the schedule of Sandia Livermore's newly installed field ion beam (FIB) apparatus to be cut up into APT samples in October (2015). Currently there is also a second Cu/Al in preparation. For this second sample the Cu will be deposited on a Al(111) surface, which will allow us to examine the influence of the interface orientation, i.e., by comparing Cu/Al(001) versus Cu/Al(111). The preparation of this second sample is expected to be completed within this project.

The detailed data on intermixing we expect to obtain with atom probe will be useful for testing and training atomic models of the Cu-Al interaction. In addition, this detailed structural information can be used to guide the growth of tailored Cu-Al surface alloys in a separate UHV chamber where they will be exposed to hydrogen and analyzed with low energy ion scattering (LEIS). Taking advantage of its sensitivity to hydrogen as well of its high surface specificity, LEIS will be employed to characterize the evolution of the Cu films in real time, along with their interaction with hydrogen.

APPENDIX F: PUBLICATIONS

This is a list of papers associated with this project including published, submitted, and in preparation.

1. X.W. Zhou, D.K. Ward, M. Foster, and J.A. Zimmerman, An analytical bond-order potential for the copper–hydrogen binary system, in: *J. Mater. Sci.*, Vol.50, pp. 2859–2875, 2015.
2. X.W. Zhou, D.K. Ward, and M. Foster, An analytical bond-order potential for the aluminum copper binary system, submitted to *Phys. Chem. Chem. Phys.*

3. X.W. Zhou, D.K. Ward, J.A. Zimmerman, J.L. Crus-Campa, D. Zubia, J.E. Martin, and F. van Swol, An atomistically validated continuum model for strain relaxation and misfit dislocation formation, submitted to *J. Mech. Phys. Sol.*
4. P. Chao and R.A. Karnesky, Hydrogen isotope trapping in Al-Cu binary alloys, to be submitted to *Acta Mat.*
5. X.W. Zhou, D.K. Ward, and M. Foster, A bond-order potential for the Al-Cu-H ternary system, In Preparation.
6. X.W. Zhou, R.B. Sills, D.K. Ward, and R.A. Karnesky, Atomistic calculations of dislocation core energy in aluminum, In Preparation.
7. R.D. Kolasinski, et al. Analysis of hydrogen interactions with aluminum surfaces using direct recoil spectrometry, In Preparation.
8. R.B. Sills, Dislocation dynamics of face-centered cubic metals and alloys, Ph.D. thesis, In Preparation.

DISTRIBUTION

1	MS0343	Carl W. Vanecek	2610
1	MS0359	Donna L. Chavez	1911
1	MS0899	Technical Library	9536 (electronic copy)
1	MS9035	Dorian K. Balch	8254
1	MS9154	Bill P. Ballard	8200
1	MS9161	Chris W. San Marchi	8367

Sandia National Laboratories